ENABLING TECHNOLOGIES FOR MULTIPLEXED BIOMOLECULE ANALYSIS AND CELL SORTING

by

DANIEL COLIN PREGIBON

B.S. Chemical Engineering, Case Western Reserve University (2003).

Submitted to the Department of Chemical Engineering
in partial fulfillment of the requirements for the degree of

Doctor of Philosophy in Chemical Engineering

at the

MASSACHUSETTS INSTITUTE OF TECHNOLOGY

May 2008

© Massachusetts Institute of Technology 2008. All rights reserved.

Author______________________________
Department of Chemical Engineering
May 23$^{\text{rd}}$, 2008

Certified by______________________________
Patrick S. Doyle
Doherty Associate Professor of Chemical Engineering, MIT
Thesis Supervisor

Certified by______________________________
Mehmet Toner
Professor of Surgery and Health Sciences & Technology, Harvard and MGH
Thesis Supervisor

Accepted by______________________________
William M. Deen
Chairman, Department Committee on Graduate Students

Enabling Technologies for Multiplexed Biomolecule Analysis and Cell Sorting

by

Daniel Colin Pregibon

Submitted to the Department of Chemical Engineering
on May 23rd, 2008, in partial fulfillment of the
requirements for the degree of
Doctor of Philosophy in Chemical Engineering

Abstract

The quantification and manipulation of biological entities from a physiological sample is extremely important for a broad range of applications in medical diagnostics, therapeutics, and basic science research. From a diagnostics standpoint, the cells, proteins, and nucleic acids that compose our bodies contain an enormous amount of information that can indicate the presence of, progression of, or even susceptibility to a given disease. However, extracting this information is often quite challenging. New tools are constantly being developed to make diagnostic testing more accurate, less invasive, faster, and less expensive. To this end, this thesis describes that advent of technologies to (1) precisely pattern biologically- and magnetically-active beads in hydrogel substrates for cell sorting and pattering, (2) synthesize morphologically and chemically-complex microparticles in a high-throughput fashion, and (3) perform rapid and accurate multiplexed biomolecule quantification using such particles.

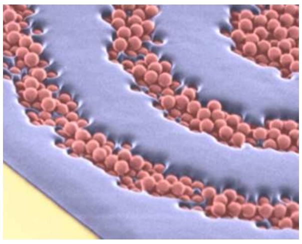

Bead-Patterned Hydrogels are a class of materials developed in this thesis that consist of microbeads precisely patterned in poly(ethylene glycol) (PEG) matrices. Using microfluidics and projection lithography on a standard microscope, magnetically-active or protein-decorated beads were patterned in close-packed or disperse-bead patterns on glass substrates with high resolution over large areas. Using slight alterations to the synthesis protocol, bead patterns could be completely encapsulated in a bio-inert PEG matrix, or exposed from the PEG surface. It was shown that bead-patterned hydrogels could be used for the phenotype-specific sorting or patterning of lymphocytes.

As was observed in the synthesis of bead-patterned hydrogels, free-radical polymerization is inhibited near microfluidic channel walls due to oxygen diffusion through the porous polydimethoxysilane (PDMS) elastomer composing devices. By exploiting this phenomenon using projection lithography in an all-PDMS device, **Continuous-Flow Lithography** was developed. In stark contrast to traditional methods for anisotropic particle synthesis, this one-phase process provides a simple method to synthesize microparticles with complex morphologies and/or multiple adjacent chemistries in a high-throughput fashion. The processes is broadly applicable to any free-radical reacting monomer. For improved resolution and sharpened interfaces between adjacent chemistries,

Stop-Flow Lithography was implemented using a valve system to rapidly start and stop flow in a fluidic system.

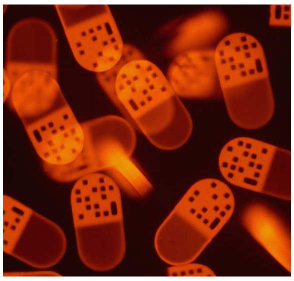

Flow lithography provided unprecedented control over particle shape, composition, and inclusion of multiple functionalities. Utilizing these attributes, **Encoded Hydrogel Particles** were synthesized bearing multiple functional regions including a graphical barcode and one or more DNA probe-loaded regions. These particles were used for multiplexed detection of deoxyribonucleic acid (DNA) and ribonucleic acids (RNA), affording virtually unlimited multiplexing capabilities, single-color detection, flow-through scanning in a microfluidic device, and low cost. Mathematical models were developed to understand the kinetics of hybridization depending on particle design and assay conditions. Using these models to direct optimization, the method was shown to give attomole-sensitivity, single-nucleotide specificity, and rapid hybridization kinetics. Overall, this thesis demonstrates the combination of hydrogels, lithography, and microfluidics to generate intricate substrates and particles that provide means for high-performance, low-cost bioseparations and molecular screening.

Thesis Supervisor: Patrick S. Doyle
Title: Doherty Associate Professor of Chemical Engineering, MIT

Thesis Supervisor: Mehmet Toner
Title: Professor of Surgery and Health Sciences & Technology, Harvard and MGH

Acknowledgments

The work presented in this thesis is not the product of one person alone; it would not have been possible without the patient mentoring, creative brainstorming, constructive criticism, and constant support given by many people I have interacted with over these last five years. I deeply appreciate all of the individuals who have contributed directly or indirectly to this work or my graduate experience as a whole. This has truly been a rewarding and memorable endeavor.

First, I would like to extend a sincere thank you to my advisors who provided consistent direction and motivation throughout my Ph.D. studies. Pat – thank you for teaching me how to think critically about problems, construct thorough studies, and put ideas into scientifically-relevant contexts. Thank you for keeping me focused, and for your patience over these years. Mehmet – thank you for your constant enthusiasm and creativity. Thank you for helping me to identify important biological problems to which our technologies could be applied. To my committee members Dr. T. Alan Hatton and Dr. Paul Matsudaira – thank you for showing your support, expressing your concerns, and consistently providing useful insights.

There are several Doyle Group members who been very valuable to my thesis studies. Dhananjay Dendukuri – it was an absolute pleasure working with you. I truly admire your analytical proficiency, experimental ingenuity, and always-cheerful nature. Ramin Haghgooie – thanks for showing me the ropes early in my Ph.D. career, working with me on the magnetic cell sorting project, and giving continued assistance even after graduation. Anthony Balducci – thank you for the countless discussions over these past years. Sorry you got stuck sitting next to me... I would also like to thank past members of the Doyle Group for making my transition into the group smooth and enjoyable, as well as current students and post-docs for keeping it interesting.

I have had the privilege of working with several talented undergraduate "UROP" students including Shelley Gu, Stephen Maltas, Jesse Collins, and Jesse Lee. Thank you all for your hard work. I would also like to thank everyone I met at the Center for Engineering in Medicine who among other things, helped me make devices, culture cells, and explore new ideas. Thanks also to the assistants who provided administrative help over the years.

Beyond the purely academic scope, I would like to extend thanks to the Deshpande Center and others for entrepreneurial mentoring, as well as the groups in the i-Teams and New Enterprises courses who have given valuable input for business development of ideas introduced in this thesis. Last but certainly not least, I would like to thank my family and friends for their persistent support and encouragement. Thank you for everything.

Table of Contents

Abstract **3**

Chapter 1 Introduction **21**

1.1 Microfluidics for Biological Applications . . . 21
1.2 Medical Diagnostics Using Cells and Biomolecules . . . 22
1.3 Patterning Probes . . . 23
  1.3.1 Patterning Proteins . . . 24
  1.3.2 Patterning Microbeads . . . 24
  1.3.3 Patterning Magnetic Materials . . . 24
  1.3.4 Patterning Nucleic Acids . . . 24
1.4 Multiplexed Analysis . . . 26
  1.4.1 Encoding Methods Used for Solution Arrays . . . 26
  1.4.2 Synthesis of Complex Particles for Solution Arrays . . . 28
  1.4.3 Thermodynamics of Hybridization on Solid Substrates . . . 28
  1.4.4 Hydrogel Substrates for Nucleic Acid Detection . . . 29
1.5 Other Uses of Hydrogels . . . 29
1.6 Outline of Thesis . . . 30

Chapter 2 General Materials and Experimental Methods **33**
2.1 Materials . . . 33
2.1.1 Chemicals and Buffers . . . 33
2.1.2 Oligonucleotides . . . 34
2.2 Equipment Setup . . . 36
2.2.1 Configuration of Microscope for Polymerization . . . 36
2.2.2 Syringe-Pump Sample Delivery . . . 36
2.2.3 Pressure System for Sample Delivery . . . 36
2.3 General Experimental Protocols . . . 36
2.3.1 Soft Lithography . . . 36
2.3.2 Making PDMS-Coated Slides . . . 37
2.3.3 Assembling Microfluidic Devices . . . 37
2.3.4 Activating Glass Slides with Methacrylates . . . 37
2.3.5 Cell Culture . . . 38
2.3.6 Suspending Fluorescent Monomers . . . 38
2.3.7 Preparation of Prepolymers . . . 38
2.3.8 Preparation of Prepolymers Containing Beads . . . 38
2.3.9 Preparation of Prepolymers Containing DNA . . . 38
2.3.10 Particle Recovery and Rinsing . . . 39
2.3.11 Hybridization with Nucleic Acids . . . 39
2.3.12 Labelling Biotinylated Targets . . . 39
2.3.13 Direct-Labelling of Hybridized Targets . . . 39
2.3.14 Imaging Particles . . . 40

Chapter 3 Bead-Patterned Hydrogels **41**
3.1 Description of Bead-Patterened Hydrogels . . . 42
3.2 Principles of Patterning . . . 42
3.3 Dispersed-Bead Magnetic Patterns . . . 44
3.4 Packed-Bead Magnetic Patterns . . . 45
3.5 Exposed Versus Encapsulated Bead Patterns . . . 47
3.6 Protein-Bound-Bead Patterns . . . 47
3.7 Cell Capture Experiments . . . 48
3.7.1 Capture of Magnetic-Bound B Cells . . . 48
3.7.2 Direct Capture of B Cells on Patterned Beads . . . 48
3.8 Conclusions . . . 50

Chapter 4 Flow Lithography **51**
4.1 Continuous-Flow Lithography . . . 52
4.1.1 Synthesis of Janus and Multifunctional Particles . . . 55
4.1.2 Armored Droplets . . . 56
4.1.3 Limitations of CFL . . . 58
4.2 Stop-Flow Lithography . . . 58
4.2.1 Improvement of Resolution and Throughput over CFL . . . 59
4.2.2 Synthesis of Multi-functional Particles with Sharp Interfaces . . . 60
4.2.3 Valve System for Independent Stream Control . . . 61

4.3 Conclusions . . . 62

Chapter 5 Encoded Hydrogel Particles **63**
5.1 Synthesis of Multifunctional Encoded Particles . . . 64
5.2 Multiplexed DNA Detection . . . 66
5.3 Flow-through Particles Scanning . . . 67
5.4 Preliminary Investigation of Particle Composition . . . 69
  5.4.1 Probe Concentration . . . 69
  5.4.2 Choice of Monomers . . . 70
5.5 Characterization of Particles . . . 70
  5.5.1 Polydispersity . . . 70
  5.5.2 Active Probe Concentration . . . 70
  5.5.3 Estimation of Throughput . . . 72
  5.5.4 Initial Study of Detection Limits and Dynamic Range . . . 73
  5.5.5 Cost of Materials . . . 74
5.6 Conclusions . . . 75

Chapter 6 Assay Optimization and Validation for mRNA Profiling **77**
6.1 1–D Encoding for Medium-Density Applications . . . 77
6.2 Investigation of Particle Composition . . . 79
6.3 Schemes for Labeling Targets . . . 81
6.4 Method Validation via mRNA Profiling . . . 84
6.5 Conclusions . . . 86

Chapter 7 Kinetic Modelling and Assessment of Performance **87**
7.1 Modelling Hybridization . . . 87
  7.1.1 Reaction Diffusion Model . . . 89
  7.1.2 Reaction-Limited Model . . . 92
  7.1.3 Perfect Mixing Assumption . . . 94
7.2 Experimental Validation of Reaction-Diffusion Model . . . 95
7.3 Experimental Validation of Reaction-Limited Model . . . 97
7.4 Investigation of Sensitivity . . . 98
7.5 Investigation of Specificity . . . 99
7.6 Conclusions . . . 100

Chapter 8 Conclusions and Outlook **101**
8.1 Microwell-Directed Hydrogel Patterning . . . 102
8.2 Pattern-Assisted Magnetic Cell Sorting . . . 102
8.3 Armored Droplets and Cell Encapsulation . . . 104
8.4 Particle Scanning Technologies . . . 104
8.5 Development of a Generic Scheme for Probe Attachment . . . 106

Bibliography **109**

List of Figures

1.1 Use of microfluidics used for biological processes. Shown are examples of polymerase chain reaction (PCR) [1], cell culture [13], fluorescence-activated cell sorting [10], and immunomagnetic cell sorting [11]. 22

1.2 Examples of methods used to pattern beads and magnetic materials onto substrates. Bead-patterning methods shown include wet stamping [53], patterning of hydrophilic regions using capillary forces [59], optical positioning [55], and patterning using physical templates [61]. Magnetic patterns shown are made via electrodeposition of metal through a stencil [70], doping of PDMS [71], and stamp-patterning of magnetic beads [72]. 25

1.3 Comparison of multiplexing throughput and density for bead and planar arrays. . . 26

1.4 Methods for particle encoding. Shown are examples of spectrometric(wavelength) [81], graphical [86, 90, 89, 88], chemical [85], radio frequency [94], and shape [96] encoding schemes. 27

1.5 Comparison of hybridization kinetics on solid substrates and in solution (adapted from [112]). (a) Representation of free energies associated with target-probe hybridization on solid surfaces and that in solution. (b) Graph showing experimentally-observed association constants, K_{ES}, versus calculated constants for hybridization in solution, K_{EB}. 29

1.6 Hydrogels arrays. (a) Bright-field image of hydrogel-based microarray [114]. (b) Comparison of hybridization thermodynamics (Gibbs free energy) of gel systems versus solution hybridization [115]. (c) Direct comparison of hybridization on solid-substrate arrays versus gel arrays [116]. 30

3.1 Schematic of structure polymerization for dispersed magnetic bead patterns. 43

3.2 Variation of structure height with exposure dose when UV-irradiated through the glass substrate (a, b) or PDMS channel (c, d). (a, c) Schematic of hydrogel polymerization through glass substrate or PDMS channel. (b, d) Scanning electron micrograph of PEG structures polymerized for 0.05, 0.1, 0.2, 0.4, 0.8, 1.5, and 3 seconds in a 9.6 μm-tall channel. (e) Graph showing structure height with varying UV exposure times, estimated from SEM images shown in (b) and (d). The height measurement uncertainty (shown as error bars in (e)) is due to the SEM image resolution (pixel size). Scale bars are 200 μm. 43

3.3 Dispersed magnetic bead patterns in rectangular PEG structures. (a) – (c) Bright field images of PEG structures with varying concentrations of beads. (d) Scanning electron micrograph of structure shown in (c). Scale bars: 100 μm (a – c); 20 μm (d). 44

3.4 (a) Bright field image of magnetic bead islands polymerized to a glass substrate. (b) Composite structure with PEG rectangle polymerized around the magnetic bead islands. (c) Scanning electron micrograph of exposed beads in PEG structure. Scale Bars: 100 μm (a, b); 5 μm (c). 45

3.5 (a) Scanning electron micrograph of magnetic beads patterned in a target shape on a glass substrate. (b) Bright field image and (c) scanning electron micrograph of a target bead pattern with a rectangular PEG structure polymerized around it from below the substrate. (d) Bright field image of another packed-bead pattern with a rectangular PEG film polymerized around it. (e) Lines and (f) dots patterned to glass over lengths greater than 1 μm. (g) Bright field image with close-up inlay of a single rail of magnetic beads encapsulated in PEG. (h) Scanning electron micrograph of the rail in (g), showing that the beads are completely encapsulated in PEG. Scale bars: 20 μm (a,c); 100 μm (b, d, f, g); 200 μm (e); 10 μm (g inlay, h). 46

3.6 Scanning electron micrographs of (a) free-standing packed bead cluster polymerized to glass, (b) cluster with outer PEG structure polymerized from below the glass substrate, and (c) cluster with outer PEG structure polymerized through PDMS channel, each with bright field image inlays. Scale bars: 20 μm (a – c); 50 μm (a – c inlays). 47

3.7 (a) Bright field image of B and T cells incubated with α-CD19 decorated microbeads (with bead-bound cells circled). (b) Fluorescence image of cells in (a), showing the specificity of the beads for the fluorescently dyed B cells. (c) Schematic of magnetic-bound cell capture experiment. (d) Bright field image of PEG-encapsulated magnetic bead cluster platform in a microchannel. (e) Bead-bound B cells captured over the magnetic pads in a flow. Scale bars: 30 μm (a,b); 200 μm (d); 50 μm (e). 49

3.8 (a) Schematic of direct cell capture experiment. (b) Bright field image of patterned anti-CD19 microbeads on a glass substrate. (c) Cells captured directly on the patterned beads in a fluid flow. Scale bars: 100 μm (b); 25 μm (c). 50

4.1 Experimental Setup. (a) Schematic of setup, where bursts of UV light are shown through a transparency mask and microscope objective onto a flowing monomer stream in an all-PDMS microdevice. (b) A brightfield image (xy plane) of an array of cuboids moving through the unpolymerized monomer. (c) A cross-sectional view of the cuboids seen in (b) upon collection in a droplet that has turned most particles on their sides. 52

4.2 Differential Interference Contrast images of collections of particles. Particles were generated in a high-throughput fashion and collected in a reservoir. (a) Rings formed using a 9.6 μm high channel and the 20× objective . (b) Triangles formed in a 38 μm high channel using a triangular mask and the 20× objective. (c) Cylinders were synthesized using circular masks in channels 38 μm tall using the 20× objective. (d) Colloidal cuboids synthesized using a square mask and the 20× objective in a 9.6 μm high channel. 53

4.3 SEM images of particles. Microparticles formed using a 20× objective (except d was formed using a 40× objective) were washed before being observed using SEM. The scale bar in all the figures is 10 μm. (a – c) Flat polygonal structures that were formed in a channel of height 20 μm. (d) A colloidal cuboid that was formed in a channel of height 9.6 μm. (e – f) High aspect ratio structures with different cross-sections that were formed in a channel of height 38 μm. (g – i) Curved particles that were all formed in a channel of height 20 μm. The inset in the figure shows the transparency mask feature that was used to make the corresponding particle. 54

4.4 Synthesis of Janus particles. (a) A cartoon showing the synthesis of Janus (two-faced) particles. The widths of the streams, L1 and L2 can be altered by changing the flow rates of the streams. (b) Two streams containing PEG-DA (grey) and PEG-DA with rhodamine labelled cross-linker (white) are co-flowed through a channel. A cartoon representing the formation of a bar-shaped particle 130 μm in length and 20 μm width is overlaid on the picture. Diffusion limited mixing seen in laminar flow is exploited to ensure the streams flow distinctly. (c) DIC image of a Janus particle. (d) Fluorescence microscopy image of the particle in (c). The rhodamine labelled portion is seen in red. (e) An overlaid image of the entire particle showing both the fluorescently labelled (orange) and the non-labelled (green) sections. The scalebar in figures (c – e) is 50 μm. (f) Multiple Janus particles with the fluorescent portion shown in orange. The scalebar is 100 μm. 55

4.5 Synthesis of armored droplets. (a) Aqueous droplets were broken off in a 40 μm-tall, 40 μm-wide T-junction channel with an organic monomer used as the continuous phase. A computer script was used to monitor droplets as they entered the polymerization region, triggering the UV shutter to polymerize an armor ring around each. Shown with the schematic is an image of arrayed droplets collected at the end of the channel (bottom), artificially colored to designate monomer (tan) and droplets (blue). (b) Time sequence images showing polymerization around a droplet. Scalebars are 50 μm. 57

4.6 Schematic of stop-flow lithography setup. Pressurized air is controlled using a 3-way solenoid valve to selectively drive monomer through a channel. A computer is used to control the valve and UV shutter synchronously to facilitate flow stoppage, polymerization of particles, and particle flushing with flow. Shown also is a brightfield image of the three-step process. Scalebars are 50 μm. 59

4.7 Interface comparison of multifunctional particles made using CFL and SFL. (a) Striped, rod-shaped particles were polymerized across adjacent streams, the center of which was loaded with a fluorescent monomer. (b) Scans of fluorescent intensity were taken along particles at a fluorescent/non-fluorescent interface. Insets show DIC and fluorescence images of particles made using CFL (with flow velocity of ~50 μm/s) and SFL (with a velocity of ~1,000 μm/s). Scalebars are 100 μm. 61

4.8 Valve system for independent flow control. (a) Schematic of flow-control system, consisting of a pressure source, 3-way solenoid valve, and independent sample chambers with pressure-control relief valves. (b) Bright-field images of stream adjustment (flow from top to bottom), showing reduction of central stream width upon opening of its respective relief valve. Scalebar is 50 μm. 62

5.1 (a) Schematic diagram of dot-coded particle synthesis showing polymerization across two adjacent laminar streams to make single-probe, half-fluorescent particles (shown in (b)). (c) Diagrammatic representation of particle features for encoding and analyte detection. Encoding scheme shown allows the generation of 2^{20} (1,048,576) unique codes. (d) Differential interference contrast (DIC) image of particles generated using the scheme shown in (a). (e – g) Overlap of fluorescence and DIC images of single-probe (e), multi-probe (f, bottom), and probe gradient (g, left) encoded particles. Shown also is a schematic representation of multi-probe particles (f, top) and a plot of fluorescent intensity along the centerline of a gradient particle (g, right). Scale bars are 100 μm (d, f, g) and 50 μm (e). 65

5.2 Multiplexed analysis using single-probe encoded particles. The particles were loaded with DNA oligomer probes (Probe #1, Probe #2, or no probe (negative control, C) as shown schematically in (a). (b) Shown are representative fluorescence images of particles after a 10min incubation with both fluorescent-labelled targets. Fluorescence in the probe-regions indicates target detection. Also shown are individual particles after incubation in solutions containing no targets, Target #1 only, Target #2 only, and both targets (c). Scalebar is 100 μm. 66

5.3 Multiplexed analysis using multi-probe particles. (a, c) Fluorescence images of particles with regions containing Probe #1, #2, and no probe (as shown in b) after a 10min incubation with targets #1, #2, or no target. Scalebar is 100 μm. 67

5.4 Flow-through particle reading. (a) Schematic representation of a flow-focusing microfluidic device used to align and read particles after hybridization experiments. Particles are directed down a narrow channel and are imaged using fluorescence microscopy. (b) A typical image of a particle taken in a flow-through device as shown in (a). The image was captured using a microscope-mounted camera with an exposure of 1/125 sec as the particle flowed at a velocity of ∼1200 μm/s through the channel. Scans of fluorescent intensity were taken across the 5 “lanes” of the particle to reveal the code and detect oligomer targets (O1 and O2). With the particle in this orientation, the code is read from right to left, top to bottom where *1*, *0*, and x represent a hole, no hole, and an alignment marker, respectively. Particle shown is 90 μm × 270 μm. 68

5.5 Fluorescent intensity of particles with varying precursor probe concentrations. 69

5.6 Plot of fluorescent intensity across a particle section after target hybridization. The white line on the particle image indicates the region that was scanned. 71

5.7 Hybridization signal (fluorescent intensity) of particles incubated at varying target concentrations. 73

6.1 1–D encoding scheme. (a) Schematic of particle design with symmetric, analog dot-coding scheme (providing 2,500 codes) and probe region flanked by two control regions. (b) Sample fluorescence image and scanning. Particles are designed to be flowed along a channel and analyzed using slit illumination/detection that is perpendicular to the channel. Scans can then be analyzed to reveal the code (using trough depths) and target amount. 78

6.2 Particle composition study. (a) Penta-functional particles made from monomer solutions containing 15 - 35% PEG-DA were investigated for probe incorporation (b) and hybridization signal using two methods of fluorescent detection (c, d). Fluorescent scans along the particles (c, d, small plots) were scaled (large plots) to show penetration of streptavidin-PE (SAPE) reporter (c) and DNA targets (d) that varied from 20 – 200bp in size. Particles have dimensions of 400 × 100 × 30 μm. 80

6.3 Schematic illustrations of the two assay protocols used for detection. (a) With the “Exonuclease/PicoGreen” scheme, targets are hybridized with particles, unbound probes are digested using exonuclease I, and target-probe complexes are directly labelled using a dsDNA dye (PicoGreen). (b) With the “Biotin/SAPE” scheme, targets are biotinylated, hybridized with particles, and then fluorescently labelled using a streptavidin-PE reporter. 82

6.4 Determination of fluorescence background and target signal depletion during exonuclease incubation. (a) Particles with 50 μM probe were incubated with varying amounts of Exonuclease I for up to 60 minutes. Shown is probe-region flourescence after rinsing and dying with PicoGreen. (b) Particles were incubated with target DNA and subsequently subjected to exonuclease digestion. Shown is the resulting flourescent signal, background signal, and difference between the two (the “target” signal). 83

6.5 Assessment of noise with varying precursor probe concentrations. Particles made with monomer solutions containing 5, 10, 25, or 50 μM probe were digested with Exonuclease I and subsequently measured for fluorescent signal and signal standard deviation (SD). 84

6.6 Expression profiling of mRNA prepared by ligation mediated amplification (LMA). (a) Multifunctional particles were designed to test for five mRNA targets with a built-in negative control and arbitrary code. (b) After hybridization with LMA samples (ATRA or DMSO), the probe-regions of several particles were analyzed to quantify the amount of target captured (using fluorescent signal). (c) Target quantities were normalized using the internal control (LUA95) and their differential expression was plotted alongside expression data measured using a Luminex system. 85

6.7 Expression profiling of mRNA prepared by in vitro transcription (IVT). Five targets of interest were quantified using RNA obtained from ATRA and DMSO-treated cells. Shown is the differential expression of those targets alongside data obtained using a Luminex system. 86

7.1 Schematic of hybridization. Target oligonucleotes (S is solution, T within particles) in solution diffuse into the particle surface and bind with incorporated probes P to form complexes TP. 88

7.2 Validation of model predictions. Particles with varying probe concentrations ($[P]$), stripe width (d), and numbers (N_p) were incubated with 500 attomoles of complementary target and their fluorescence was measured over time. (a) Raw data showing the average particle signal multiplied by the number of particles. (b) The same data shown in (a) that has been plotted using the predicted timescale (left) along with comparison of predicted and measured particle signals (right). 96

7.3 Experimental validation of Reaction-Limited Model. Particles with varying probe concentrations ($[P]_o$) were incubated with complementary DNA targets at two different concentrations ($[S]_o$) and the resulting fluorescence was measured over time. (a) Raw data showing the measured probe-region fluorescent signals. (b) The same data shown in (a) that has been plotted using the predicted timescale (left) along with comparison of predicted and measured particle signals (right). 97

7.4 Assessment of assay sensitivity versus model predictions. Particles were incubated with varying amounts of target, and signal-to-noise ratios were calculated. The sensitivity was taken at the target concentration where SNR = 3. Total assay time includes both hybridization and labeling time (90 min for biotin/SAPE and 45 min for Exo/PG). 99

7.5 Assessment of assay specificity. (a) Specificity of DNA/RNA hybridization using the Exonuclease/PicoGreen labeling scheme, and (b) specificity of DNA/DNA hybridization using the biotin/SAPE labeling scheme. 100

8.1 Precise patterning of beads in photopolymerized PEG microwells. PEG structures (100 × 200 μm) with lines of $\sim$ 5 μm microwells were polymerized on a glass surface. Magnetic beads (4.5 μm) were deposited on the structures, filling most of the microwells. 103

8.2 Pattern-assisted magnetic cell sorting. (a) Schematic of sorting method where columns of magnetic beads enter a channel, are directed laterally across a stream of mixed cells, where they capture cells of interest, and into a clean buffer stream where are harvested. (b) Phase diagram for predicting "guiding" and "non-guiding" regimes for column steering using the Mason Number (Ma), number of beads per column (N) and pattern angle (θ). For more details see Reference [172]. 104

8.3 High speed particle alignment in a flow-focusing device. Time-lapse brightfield images, taken with a high-speed camera, show particles ($225 \times 90 \times 25\ \mu m$) entering the focusing region of a microfluidic channel (35um-tall), where they are aligned by side-channel sheath flows in preparation for scanning. The particles were traveling at a velocity of 0.3 m/s with no incidents of clogging in any of the preliminary experiments. Scalebar is 250 μm. 105

8.4 Generic coupling scheme using amino acid-loaded particles with amino-modified DNA probes. (a) Particles were synthesized using monomer blends of PEG-DA$_{700}$ and acrylic acid, and reacted with amino-modified DNA probe. After probe conjugation, the particles were incubated with a fluorescent target to assess incorporation. Shown are DIC (b) and fluorecence (c) images of a particle after probe conjugation and target hybridization. 106

List of Tables

2.1 List of chemical and buffer acronyms and trade names. 34
2.2 List of nucleic acid probes and targets used in this work. For targets, subscripts indicate if the oligo is DNA (D) or RNA (R), and gives chemical modifications including biotin (bio), Cy3 (Cy3), or fluorescein (F). 35

5.1 Estimation of throughput and particle volume for tests done in triplicate (each probe appears on three particles). "Normal" particle size is $\sim 100 \times 200 \times 30$ μm, while "half" size is $\sim 50 \times 100 \times 15$ μm. Particle volume is based on 10^6 targets tested, which for single and two-probe particles corresponds to 3×10^6 and 1.67×10^6 total particles, respectively. 73
5.2 Estimation of raw material cost to produce 10^6 particles ($\sim 100 \times 200 \times 30$ μm) with DNA oligomer probe incorporated at a concentration of 50 μM. 74
5.3 Estimated cost of microdevices used for particle synthesis and flow-through reading. It was assumed that master wafers have 10 channels and can be molded 10 times, and that each device could be used 5 times before being discarded. 75

7.1 Signal efficiency factors for fluorophores using our detection system. 98

CHAPTER 1

Introduction

The work presented in this thesis revolves around the development of diagnostics tools through the combination of two prominent areas of research – microfluids and hydrogels. Microfluidics has emerged as a powerful approach for the miniaturization of complex processes, while hydrogels have been broadly applied to biological applications ranging from drug delivery to tissue engineering. In order to lay out a framework for the topics covered in this thesis, this chapter outlines (1) the application of microfluidics to biological processes, (2) the principles of cell sorting and biomolecule detection for medical diagnostics, and (3) the properties of hydrogel materials that make them ideal for biological assays.

1.1 Microfluidics for Biological Applications

The miniaturization of fluidic operations affords precise control over flows, reduction of sample usage, rapid analysis, and often times reduction in cost as compared to conventional lab-scale processes. For this reason, microfluidic analogs have been developed for several important biological tools including polymerase chain reaction (PCR) [1, 2, 3], electrophoresis of biological and chemical species [4, 5], protein separation and concentration [6], cell sorting [7, 8, 9, 10, 11], cell culture [12, 13], and immunoassays [14, 15, 16]. Examples of several of these systems are shown in Figure 1.1. As these tools provide the foundation of many medical diagnostic tests, microfluidics has been successfully applied to the diagnosis of several diseases including malaria [17], sexually-transmitted

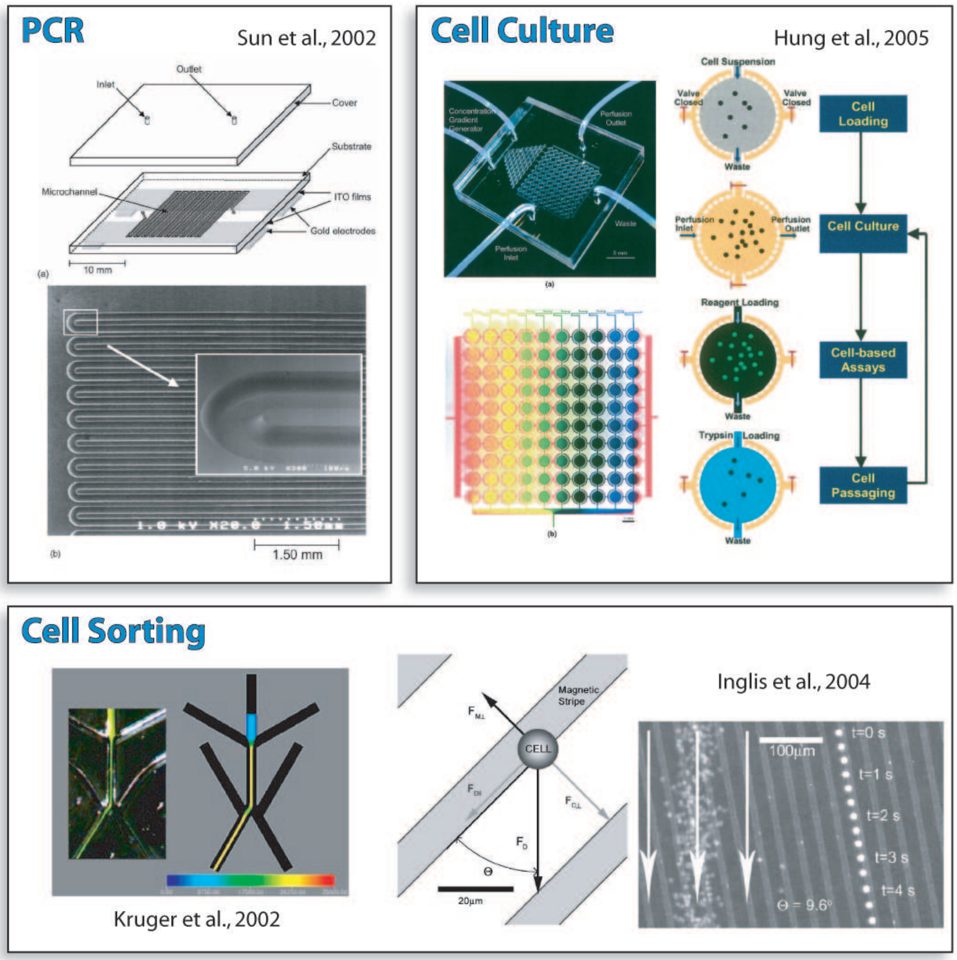
PCR
Sun et al., 2002
Inlet
Outlet
Cover
Substrate
Microchannel
ITO films
Gold electrodes
10 mm
(a)
(b)
1.50 mm
Cell Culture
Hung et al., 2005
Cell Suspension
Valve Closed
Valve Closed
Waste
Concentration Gradient Generator
Perfusion Outlet
Perfusion Inlet
Perfusion Inlet
Perfusion Outlet
Reagent Loading
Trypsin Loading
(a)
(b)
Cell Loading
Cell Culture
Cell-based Assays
Cell Passaging
Cell Sorting
Kruger et al., 2002
Magnetic Stripe
CELL
$F_{M\perp}$
$F_{D\parallel}$
$F_{D\perp}$
F_D
Θ
20µm
Inglis et al., 2004
100µm
t=0 s
t=1 s
t=2 s
t=3 s
t=4 s
Θ = 9.6°

Fig. 1.1: *Use of microfluidics used for biological processes. Shown are examples of polymerase chain reaction (PCR) [1], cell culture [13], fluorescence-activated cell sorting [10], and immunomagnetic cell sorting [11].*

diseases [18, 19], and HIV [20]. Low component cost, high sensitivity, simplicity of operation, and rapid analysis all make microfluidics an ideal platform for "point-of-care" diagnostic testing, particularly in settings where resources and funding are scarce [21]. A great deal of progress has been made in advancing microfluidic technologies over the past couple decades, demonstrating the incredible potential of miniaturized systems for hundreds of applications.

1.2 Medical Diagnostics Using Cells and Biomolecules

The cells, proteins, and nucleic acids comprising a physiological sample (a drop of blood for instance) contain a great deal of information that can be used to detect disease, direct treatments, or even predict disease. For example, a quantitative decline in the number of lymphocytes expressing CD4 surface markers is characteristic of HIV infections [22], while the over-expression of prostate-specific antigen (PSA) in serum indicates prostate cancer [23], and specific gene mutations suggest the presence of cystic fibrosis [24]. Because biological samples are often complex mixtures containing many entities, the accurate quantification of cells, proteins, and nucleic acids is typically no menial task. As the work in this document revolves around cells and nucleic acids (though the concept is similar for proteins), these will be the focus of discussion for this section.

Whole cells represent complex systems that not only have significant diagnostic value, but are often used in therapeutics. As such, methods of obtaining homogeneous populations from heterogeneous mixtures are constantly being developed and improved. Two examples of cell sorting methods include immunomagnetic sorting [25, 26] and fluorescence-activated sorting [27, 28]. Applications of cell sorting include isolation of hematopoietic stem cells for cell replacement and regeneration after chemotherapy or for cardiovascular disease [29], dendritic cells for induced immunity against cancer [30, 31], prenatal cells from maternal blood for preimplantation diagnostics [32, 33], osteoblasts for tissue engineering [34], and monocytes [35], nuetrophils [36], antigen-specific B-cells [37, 38, 39], or tissue cells for studies of immunity, proteomics, systems biology, or cellular metabolism. Cell sorting also encompasses cell depletion (negative selection) for purposes such as removal of tumor cells for autologous (self) hematopoietic stem cell transplantation or T-cells for allogenic (non-self) transplants to reduce risk of graft versus host disease [40, 41].

At a lower level in complexity than cells, nucleic acids (DNA and RNA) are extremely attractive targets for diagnostics. They are highly specific, can be amplified to increase abundance in most applications, and can be labelled (for detection) using a number of approaches. As mentioned earlier, mutations (changes in nucleic acid *sequence*) can indicate disease. In addition to sequence, the *abundance* of nucleic acid targets is also of great importance. The up- or down-regulation of nucleic acid production is an important indicator for applications like drug discovery [42] and cancer diagnostics [43]. Therefore, the assessment of both nucleic acid sequence and relative expression level is extremely important for diagnostic applications. Methods for sequence discrimination and nucleic acid quantification are discussed at length in section 1.4.

In any given diagnostic test, the targets (cells, proteins, nucleic acids, etc) must be manipulated, captured, or detected. For a test to be meaningful, it must be specific for the target(s) of interest and sensitive enough to detect entities at physiologically-relevant quantities. In order to very precisely control the capture of biological entities for this purpose, several methods have been developed to spatially pattern biological probes on substrates.

1.3 Patterning Probes

Biological probes that interact specifically with only certain species can be immobilized on a substrate (planar or bead) in order to selectively capture a target of interest. Thanks to great advances in immobilization techniques, probes including proteins, nucleic acids, whole cells, and other "active" components can be accurately patterned on surfaces. Because cells express unique "surface marker" proteins that typically vary greatly among cell types, protein probes that interact specifically with these markers can be used to immobilize desired cell phenotypes. Nucleic acids on the other hand, can simply be targeted using nucleic acid probes that have complementary sequences. In either case, the accurate patterning of these capture molecules is of great importance in many diagnostic processes.

1.3.1 Patterning Proteins

Spatially controlling the immobilization of proteins is valuable for developing immunoassays, protein microarrays, and cellular arrays for bio-sensor applications. Several techniques exist for patterning proteins including deposition using three-dimensional microfluidic systems [44], photochemical or pH-sensitive deprotection of protein-adhesive substrate coatings [45, 46], polymer on polymer stamping [47], plasma etching using a stamp with subsequent blocking or protein deposition [48], and chemical vapor deposition polymerization [49]. In contrast to planar substrates, microbeads adhered to gold [50] or polyelectrolyte [51] substrates have also been used as solid substrates for protein coupling and subsequent cell culture.

1.3.2 Patterning Microbeads

Microbead patterns are of interest for creating microlense arrays, optical materials, biosensor arrays, and substrates for protein coupling. Traditional techniques employed in patterning colloids on substrates include polymer stamping [52, 53], optical [54, 55, 56] or dielectric [57] manipulation, assembly on hydrophilic regions using capillary forces [58, 59], aggregation on patterned silane layers [60], assembly on physical templates [61, 62], and positioning using scanning electron microscopy [63]. Some of these are shown in Figure 1.2. In general, the current bead patterning technologies are imprecise and leave unstable patterns that can be easily disrupted upon drying or fluid shear stresses. In addition, wet stamping allows the use of only electrostatically charged particles and leaves behind charged polymer residue that must be shielded before device use. Lastly, these technologies do not permit the direct patterning of biologically-active microbeads that require no additional chemical modification prior to analyte capture. Beyond patterning applications, microbeads are commonly used in microfluidic devices for cell sorting [11, 64], immunoassays [65, 66, 67], and DNA hybridization [68, 69]. Quite often, magnetic beads are utilized because they can be addressed independently of all other non-magnetic species.

1.3.3 Patterning Magnetic Materials

Paramagnetic, ferromagnetic, and electromagnetic components are commonly used in microfluidic devices to capture or manipulate magnetic species. Magnetic patterns can be accomplished by electrodeposition of metals through a stencil [70] or onto an etched substrate with subsequent polishing of excess metals [11]. Other methods include the patterning of magnetic microbeads on polymer-stamped regions [72] and micromolding with magnetic-doped poly(dimethyl siloxane) [71]. Although these processes yield precise magnetic patterns, they require expensive equipment and time-consuming processes, and the resulting devices subsequently need to be rendered bio-inert for use in most biological applications. Protein-adhesive ligands and protein-resistant polymers are commonly used to modify microdevices for this purpose, defining bio-adherent and inert regions.

1.3.4 Patterning Nucleic Acids

Nucleic acid patterning lies at the foundation of DNA microarrays. As such, several methods have been developed to precisely arrange DNA probes onto surfaces (typically glass). The two broad methods for patterning DNA are robotic printing [73] and light-directed nucleotide synthesis [74]. Both of these methods allow a user quantify a huge number of targets (typically $\sim$ 10,000) in a single

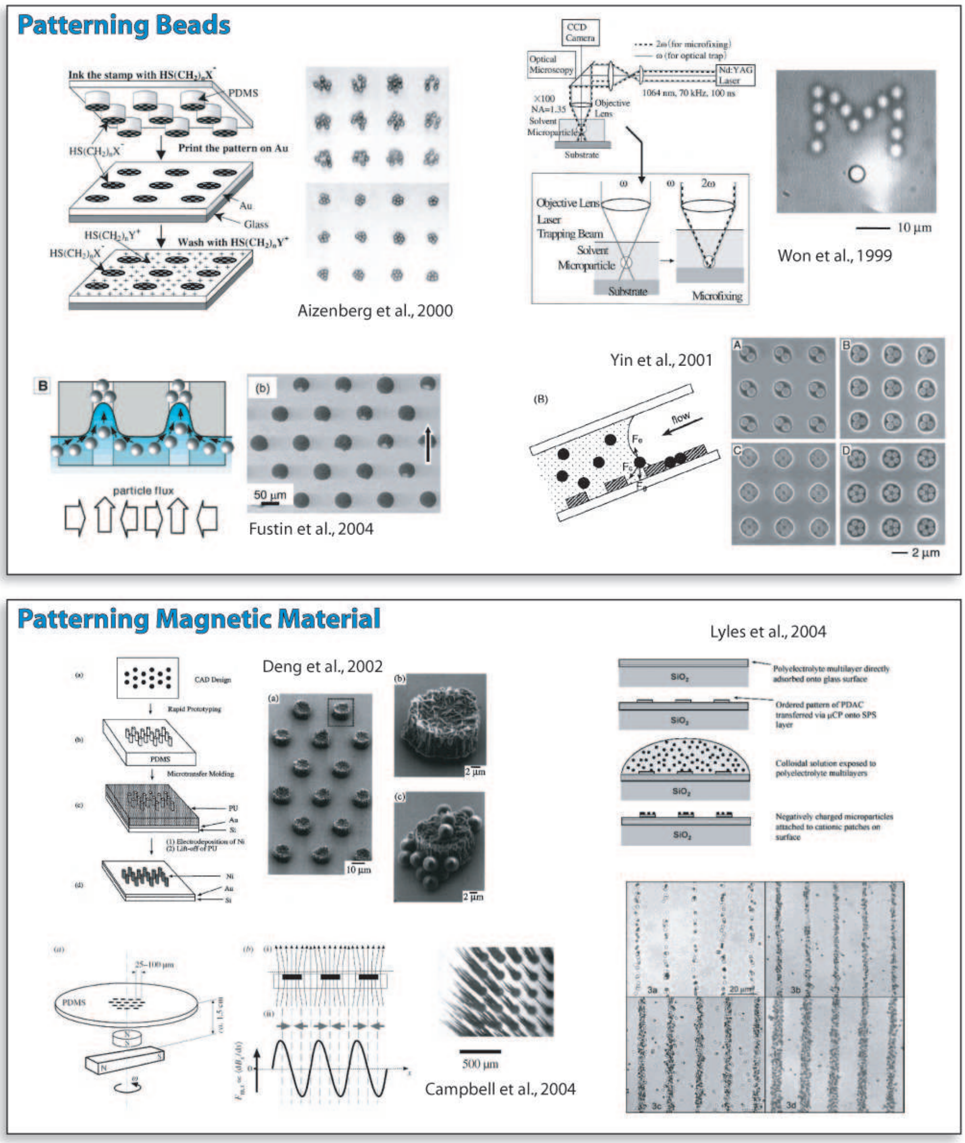
Patterning Beads
Ink the stamp with HS(CH2)nX
PDMS
HS(CH2)nX
Print the pattern on Au
Au
Glass
HS(CH2)nY+
HS(CH2)nX
Wash with HS(CH2)nY+
Aizenberg et al., 2000
CCD Camera
Optical Microscopy
2ω (for microfixing)
ω (for optical trap)
Nd:YAG Laser
1064 nm, 70 kHz, 100 ns
×100
NA=1.35
Solvent
Microparticle
Objective Lens
Substrate
Objective Lens
Laser
Trapping Beam
Solvent
Microparticle
Substrate
Microfixing
ω
2ω
10 µm
Won et al., 1999
B
particle flux
(b)
50 µm
Fustin et al., 2004
Yin et al., 2001
(B)
flow
A
B
C
D
2 µm
Patterning Magnetic Material
CAD Design
Rapid Prototyping
PDMS
Microtransfer Molding
PU
Au
Si
(1) Electrodeposition of Ni
(2) Lift-off of PU
Ni
Au
Si
Deng et al., 2002
(a)
(b)
(c)
10 µm
2 µm
2 µm
Lyles et al., 2004
SiO2
Polyelectrolyte multilayer directly adsorbed onto glass surface
Ordered pattern of PDAC transferred via µCP onto SPS layer
Colloidal solution exposed to polyelectrolyte multilayers
Negatively charged microparticles attached to cationic patches on surface
PDMS
25–100 µm
ca. 1.5 cm
N
S
500 µm
Campbell et al., 2004
3a
3b
3c
3d
20 µm

Fig. 1.2: *Examples of methods used to pattern beads and magnetic materials onto substrates. Bead-patterning methods shown include wet stamping [53], patterning of hydrophilic regions using capillary forces [59], optical positioning [55], and patterning using physical templates [61]. Magnetic patterns shown are made via electrodeposition of metal through a stencil [70], doping of PDMS [71], and stamp-patterning of magnetic beads [72].*

sample. Thus, the microarray provided the first platform suitable for "high-density" multiplexed analysis of biomolecules.

1.4 Multiplexed Analysis

The ability to quantify multiple proteins, cytokines, or nucleic acid sequences in parallel using a single sample allows researchers and clinicians to obtain high-density information with minimal assay time, sample volume, and cost. Such multiplexed analysis is accompanied by several challenges including molecular encoding and the need to retain assay sensitivity, specificity, and reproducibility while using complex mixtures.

There are two broad classes of technologies used for multiplexing – planar arrays and suspension (particle-based) arrays, both of which have application-specific advantages. Planar arrays, such as DNA and protein microarrays [75, 74, 73], are best suited for applications requiring ultra high-density analysis. In comparison, suspension arrays benefit from faster kinetics, ease of assay modification, higher sample throughput, and better quality control by batch synthesis [76]. Though particle-based arrays have been used for high-density genotyping applications [77], they are most favorable over microarrays when detecting a modest number of targets over large populations or when rapid probe-set modification is desired. As seen in Figure 1.3, bead-based arrays provide high *throughput*, planar arrays provide high *density*, but neither of these technologies can be applied efficiently to high-throughput, medium density applications, which include *in vitro* cancer diagnostics, neonatal diagnostics, and drug discovery.

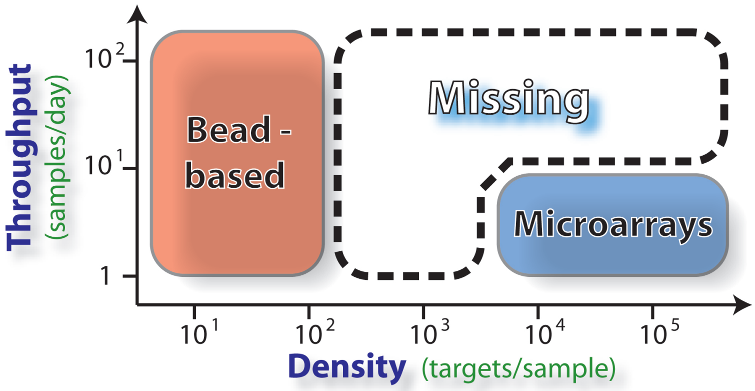

Fig. 1.3: *Comparison of multiplexing throughput and density for bead and planar arrays.*

1.4.1 Encoding Methods Used for Solution Arrays

While planar arrays rely strictly on positional encoding, suspension arrays have utilized a great number of encoding schemes that can be classified as spectrometric [78, 79, 80, 81, 82, 83, 84, 85], graphical [86, 87, 88, 89, 90], electronic [91, 92, 93, 94], or physical [95, 96]. Examples of these encoding methods are shown in Figure 1.4. Spectrometric encoding encompasses any scheme that relies on the use of specific wavelengths of light or radiation (including fluorophores [78, 79, 80, 81], chromophores [82], photonic structures [83], or Raman tags [84, 85]) to identify a species. Fluorescence-encoded microbeads [78, 79, 80, 81] can be rapidly processed using conventional flow-cytometry (or

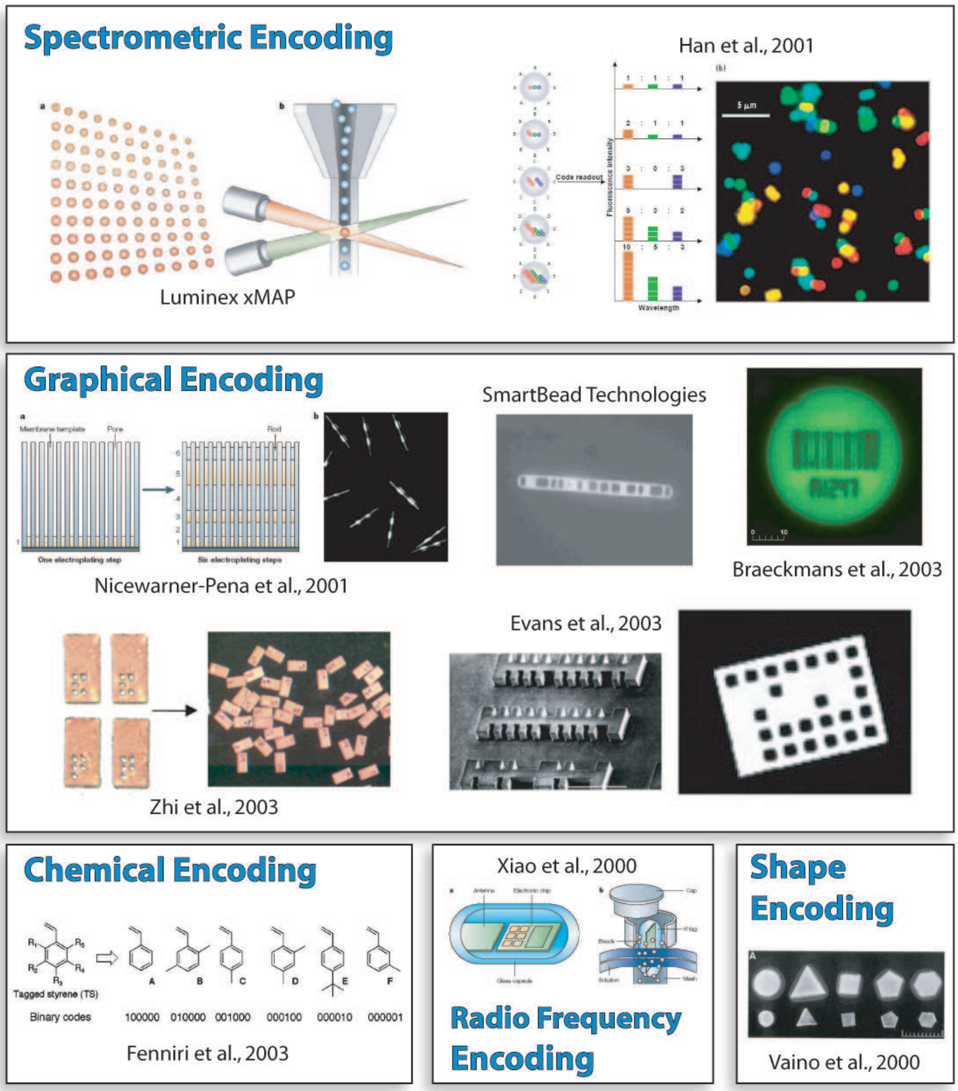
Spectrometric Encoding
Han et al., 2001
Luminex xMAP
Code readout
Fluorescence intensity
Wavelength
5 µm
Graphical Encoding
SmartBead Technologies
Membrane template
Pore
Rod
One electroplating step
Six electroplating steps
Nicewarner-Pena et al., 2001
Braeckmans et al., 2003
Evans et al., 2003
Zhi et al., 2003
Chemical Encoding
Tagged styrene (TS)
Binary codes
100000
010000
001000
000100
000010
000001
Fenniri et al., 2003
Xiao et al., 2000
Radio Frequency Encoding
Shape Encoding
Vaino et al., 2000

Fig. 1.4: *Methods for particle encoding. Shown are examples of spectrometric(wavelength) [81], graphical [86, 90, 89, 88], chemical [85], radio frequency [94], and shape [96] encoding schemes.*

on fiber-optic arrays [97]), making them a popular platform for multiplexing. However, there are several disadvantages of utilizing multiple fluorescent signals as means of barcoding including (1) the limited barcodes achievable (typically ∼100) due to spectral overlap, (2) the lack of portability for bulky flow cytometers, (3) added cost with each fluorescent exciter/detector needed, and (4) potential interference of encoding fluorescence with analyte-detection fluorescence. For these reasons, single-fluorescence methods exist that utilize graphical techniques to spatially embed barcodes on microcarriers.

Graphical barcodes are those that rely on the patterning of optical elements on a microcarrier – some examples include striped rods [86, 87], ridged particles [88], and dot-patterned particles [88, 89]. The chemistries used to fabricate such particles (metallic or photoresist) require additional coupling chemistries to conjugate biomolecules to the surface and in the case of striped rods, each metallic pattern needs to be generated one batch at a time. Typically, the patterns on the these particles can only be distinguished if the fluorescence of the target signal is sufficiently high. Another graphical method for microcarrier encoding is the selective photobleaching of codes into fluorescent beads [90]. In this method, both particle synthesis and decoding are time-consuming, making it an unlikely candidate for high-throughput analysis. A method that eliminates the use of fluorescence altogether is the use of radio frequency memory tags [91, 92, 93, 94]. This approach is very powerful because it allows for nearly unlimited barcodes ($>10^{12}$) and decouples the bacroding scheme from analyte quantification (fluorescence), but the synthesis of any appreciable number (thousands or millions) of these electronic microchip-based carriers may prove to be expensive and time-consuming. These and several other methods developed for multiplexed analysis are thoroughly reviewed elsewhere [98, 99].

1.4.2 Synthesis of Complex Particles for Solution Arrays

As seen in Figure 1.4, many of the particles used in solution arrays have complex morphologies. The use of complex particles extends far beyond multiplexed analysis, having impact on a broad range of applications including photonics [100], MEMS [101], biomaterials [102], and self-assembly [103]. While spherical particles can be synthesized fairly easily using bulk processes, complex particles require more sophisticated synthesis methods. Some methods for synthesizing complex particles include lithography [89, 88, 104], electrodeposition [86], stamp printing [105], or two-phase microfluidic systems [106, 107, 108, 109, 110]. Unfortunately, these technologies suffer from limitations on throughput, morphology, or available chemistries. For the purpose of DNA hybridization, the particle substrate onto which the nucleic acid probes are immobilized greatly affects the capture of targets.

1.4.3 Thermodynamics of Hybridization on Solid Substrates

The most important parameter in determining sensitivity and specificity of any given hybridization is the dissociation constant (K_d) of the nucleic acid complexes involved. For a system with target T, probe P, and target-probe complex TP, the dissociation constant is given by a ratio of their equilibrium concentrations ([mol/L]) as:

$$K_d = \frac{[T][P]}{[TP]}.$$

As such, when complex formation is favorable, K_d is very small. While complex formation (for oligomers 20bp or longer) in solution is very favorable ($K_d \sim 10^{-12} - 10^{-20}$), it is well know that solid-substrate methods suffer from dramatically inhibited kinetics ($K_d \sim 10^{-7}$) [111, 112]. The reason for this is that there is an energy cost associated with transferring target molecules into probe “forests” on solid surfaces where they can then associate with their complement strands. This is shown representatively in Figure 1.5 along with a comparison of association values (inverse K_d) seen experimentally versus those expected (solution hybridization constants).

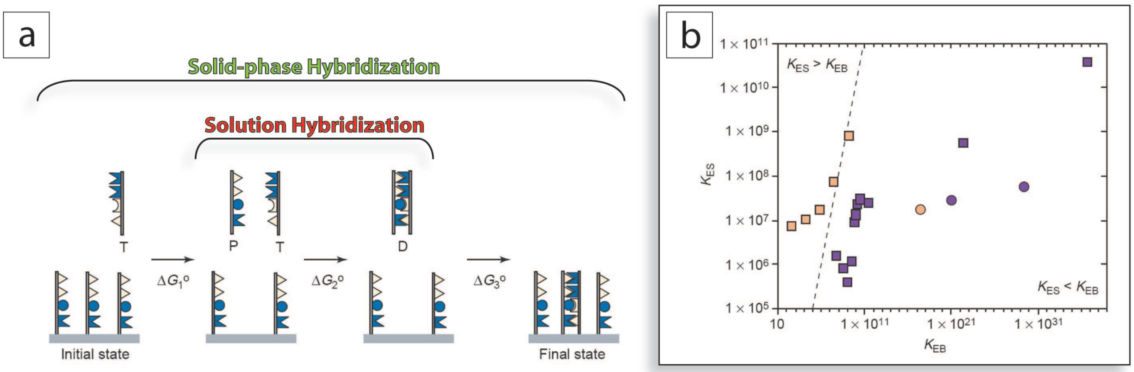

Fig. 1.5: *Comparison of hybridization kinetics on solid substrates and in solution (adapted from [112]). (a) Representation of free energies associated with target-probe hybridization on solid surfaces and that in solution. (b) Graph showing experimentally-observed association constants,* K_{ES}*, versus calculated constants for hybridization in solution,* K_{EB}*.*

To partially overcome the suppression of hybridization, locked nucleic acids are commonly used to increase complex stability approximately tenfold [113]. Although this improvement is substantial, it is important to know that solid-phase hybridization in LNA systems is still far inferior to hybridization in solution from a thermodynamic standpoint.

1.4.4 Hydrogel Substrates for Nucleic Acid Detection

As an alternative to solid surfaces, hydrogel-based substrates have been used for biomolecule detection. Hydrogels are a class of polymeric materials that are bio-friendly, three-dimensional structures that characteristically retain water. Mirzabekov's group has done a considerable amount of work in producing "MAGIC" and "IMAGE" chips [114, 115, 116], which are gel-based analogs of traditional microarrays. The most significant advantage of hydrogel systems over solid-substrates is that while hyrbidization thermodynamics are greatly suppressed on solid surfaces (as shown in Figure 1.5), hybridization in gels closely resembles solution kinetics. This is shown in Figure 1.6 along with a direct comparison of solid-phase and gel arrays.

In addition to favorable thermodynamics, gel arrays also offer a much higher effective probe density due to their 3D structure [114] and a broad range of materials and linkage chemistries. Planar hydrogel arrays have shown a great enhancement of both signal and sequence discrimination over their solid-substrate counterparts [116].

1.5 Other Uses of Hydrogels

Although several materials have been used in hydrogel synthesis, those made from poly(ethylene glycol) precursors provide a non-fouling surface to maximize assay specificity. Bio-inert substrates provide a favorable environment that is chemically transparent to biological species. Researchers

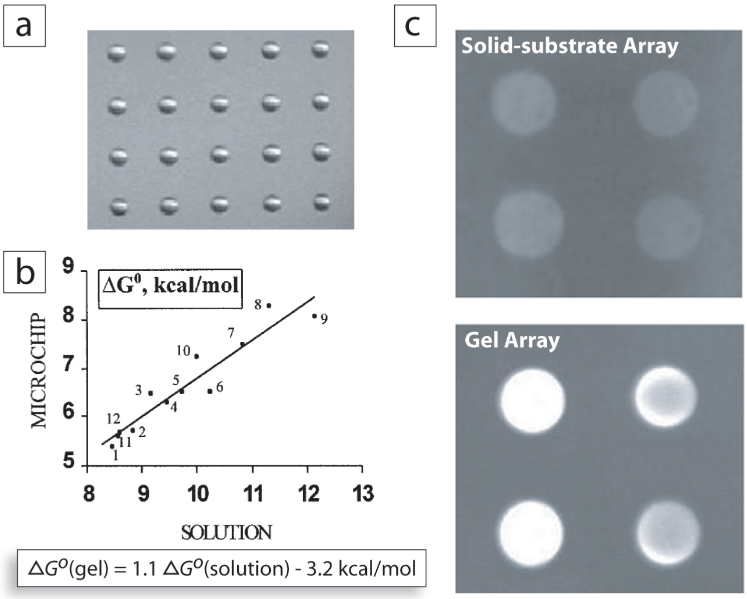

Fig. 1.6: *Hydrogels arrays. (a) Bright-field image of hydrogel-based microarray [114]. (b) Comparison of hybridization thermodynamics (Gibbs free energy) of gel systems versus solution hybridization [115]. (c) Direct comparison of hybridization on solid-substrate arrays versus gel arrays [116].*

have used UV-polymerizable hydrogels in microfluidics to fabricate stimuli-sensitive valves and pistons [117] as well as scaffolds for cellular arrays [118, 119]. Three dimensional, heterogeneous cell arrays have also been realized by polymerizing hydrogels around living cells [120]. In addition, PEG oligomers are available in a broad range of molecular weights and functionalities, providing versatility in material design. Because of their wide availability, bio-friendly nature, and favorable hybridization characteristics, hydrogels are ideal substrates for bioassays and many other biological applications.

1.6 Outline of Thesis

The objective of this work was to develop inexpensive microfluidic technologies capable of performing high-performance biological sorting and quantification as tools for diagnostic applications. It is divided broadly into three categories – patterning of surfaces with biologically-active materials, synthesizing complex microparticles, and utilizing such particles for molecular screening. The organization of this work is as follows:

> **Chapter 2** lists experimental protocols and materials for procedures used throughout this thesis.
>
> **Chapter 3** describes the synthesis of "bead-patterned hydrogels" and their use for cell sorting applications.

Chapter 4 describes the use of flow lithography to synthesize morphologically and chemically complex microparticles. The chapter describes both "continuous-flow" (CFL) and "stop-flow" lithography (SFL).

Chapter 5 describes the use of SFL for the production of multifunctional, encoded hydrogel particles that are subsequently used for multiplexed DNA detection.

Chapter 6 describes the optimization of particle composition, introduces new target detection schemes, and discusses messenger RNA profiling assays.

Chapter 7 discusses mathematical modelling of hybridization and assessment of the sensitivity and specificity of our system.

Chapter 8 outlines the findings of this thesis and discusses future work that can be done to further improve the approaches developed.

CHAPTER 2

General Materials and Experimental Methods

Several chemicals, buffers, and experimental methods were used for various processes throughout this thesis. For convenience and brevity, chemical names and abbreviations are presented below in a consolidated form and general experimental methods are presented in detail. Throughout this thesis, the materials and methods described in this chapter will be referenced. When applicable, any variation to the following methods will be described in the relevant chapter.

2.1 Materials

2.1.1 Chemicals and Buffers

Because chemical names are often cumbersome and inconvenient to use repeatedly, acronyms and chemical trade names will be used throughout this thesis. These abbreviations are defined in Table 2.1 below.

Oligomers and Elastomers	
PDMS	Polydimethoxysilane (Sylgard 184, Dow Corning)
PEG_{200}	Poly(ethylene glycol), n = 200 (Aldrich)
PEG_{400}	Poly(ethylene glycol), n = 400 (Aldrich)
$PEG\text{-}DA_{400}$	Poly(ethylene glycol) di-acrylate, n = 400 (Aldrich)
$PEG\text{-}DA_{700}$	Poly(ethylene glycol) di-acrylate, n = 700 (Aldrich)
TMP-TA	1,1,1–Trimethylpropane-triacrylate (Polysciences)
Fluorescent Monomers	
fluorescein-A	Fluorescein o-acrylate (Aldrich)
rhodamine-MA	Methacryloxyethyl thiocarbamoyl rhodamine B (Polysciences)
Photoinitiators	
Darocur 1173	2-hydroxy-2-methylpropiophenone (Aldrich)
Irgacure 2959	2-hydroxy-4'-(2-hydroxyethoxy)-2-methylpropiophenone (Aldrich)
Miscellaneous Chemicals	
MPTMS	Methacryloxypropyl trimethoxysilane (Sigma)
SAPE	Streptavidin – R-phycoerythrin (Invitrogen)
SDS	Sodium dodecyl sulfate (Invitrogen)
Tween-20	Polyoxyethylenesorbitan monolaurate (Sigma)
Buffers	
PBS	Phosphate Buffered Saline, pH = 7.2 (Invitrogen)
PBST	PBS with 0.05% Tween-20
TE (1×)	10mM Tris pH 8.0 (Rockland) and 1mM EDTA (OmniPur) in MilliQ water
TET	TE Buffer with 0.05% Tween-20
PTET	5× TET Buffer with 25% PEG$_{400}$
$HB_{0.5}$	TET Buffer with 0.5M NaCl (Mallinckrodt)
$HBS_{0.2}$	TET Buffer with 0.2M NaCl and 0.5% SDS
NEB2	New England Buffer #2 (New England Biosystems) with 0.05% Tween-20

Table 2.1: *List of chemical and buffer acronyms and trade names.*

2.1.2 Oligonucleotides

All oligonucleotides used were purchased from Integrated DNA Technologies (IDT). In this document, a "probe" refers to DNA that is incorporated in particles, while "target" oligonucleotides are those in solution to be detected. Unless otherwise stated, the probes were purchased from IDT end-functionalized with a 5' Acrydite^{TM} group that allowed covalent attachment into the hydrogels during particle synthesis. Targets were ordered with a 5' fluorophore (Cy3 or fluorescein), 5' biotin, or no modification.

Storage and Handling: DNA probes were received as lyopholized films (typical yields are $\sim 50 - 100$ nmol) while targets (DNA or RNA) were usually ordered "Lab Ready", suspended in TE to a concentration of 100 μM. For storage, DNA probes were resuspended in TE Buffer to a stock concentration (typically 1 mM). After vortexing the probes or targets for several seconds, some of the stock solution was further diluted to the desired working concentration (of typically 500 μM for probes and 10 μM for targets), which was pipetted at volumes of 5 μl into 0.6 ml Eppendorf tubes. The tubes were centrifuged for only a few seconds to ensure that the liquid was collected at the bottom and then placed in cardboard sample boxes and stored at -20^{o}C until used. *NOTE: RNA should be handled with extreme care as it is easily degraded. All reagents and materials used with RNA samples should be RNase-free. When necessary, an RNase Inhibitor (New England Biosystems) may be used.*

DNA Probes	
Name:	*Sequence and Modifications:*
P_1	5' – Acrydite-Sp18 – ATA GCA GAT CAG CAG CCA GA – 3'
P_2	5' – Acrydite-Sp18 – CAC TAT GCG CAG GTT CTC AT – 3'
P_{fluoro}	5' – Acrydite-FITC – GGA TGG GGA CTG TGG GTA GAT AGG GGA ACA ATG AGA GTC AAC TCA GGC TA – 3'
P_{lua7}	5' – Acrydite– ATT GGT AAA TTG GTA AAT GAA TTG – 3'
P_{lua27}	5' – Acrydite– AAA GTT GAG TAT TGA TTT GAA AAG – 3'
P_{lua59}	5' – Acrydite– AAA GTG AAA AAG ATT GAT TGA TGA – 3'
P_{lua68}	5' – Acrydite– AAA GAA AGA TTG TTG AGA TTA TGA – 3'
P_{lua95}	5' – Acrydite– TTA GTG TAG TAA GTT TAA AGT GTA – 3'
P_{7a}	5' – Acrydite – AAC TAT ACA ACC TAC TAC CTC A – 3'
P_{7b}	5' – Acrydite – AAC CAC ACA ACC TAC TAC CTC A – 3'
P_{7c}	5' – Acrydite – AAC CAT ACA ACC TAC TAC CTC A – 3'
P_{7d}	5' – Acrydite – AAC TAT GCA ACC TAC TAC CTC T – 3'
DNA/RNA Targets	
Name:	*Sequence and Modifications:*
$T_{1,D,Cy3}$	5' – Cy3 – TCT GGC TGC TGA TCT GCT AT – 3'
$T_{2,D,Cy3}$	5' – Cy3 – ATG AGA ACC TGC GCA TAG TG – 3'
$T_{20,D,bio}$	5' – biotin – CTC ATT GTT CCC CTA TCT AC – 3'
$T_{50,D,bio}$	5' – biotin – TAG CCT GAG TTG ACT CTC ATT GTT CCC CTA TCT ACC CAC AGT CCC CAT CC – 3'
$T_{100,D,bio}$	5' – biotin – [TAG CCT GAG TTG ACT CTC ATT GTT CCC CTA TCT ACC CAC AGT CCC CAT CC]$_2$ – 3'
$T_{200,D,bio}$	5' – biotin – [TAG CCT GAG TTG ACT CTC ATT GTT CCC CTA TCT ACC CAC AGT CCC CAT CC]$_4$ – 3'
$T_{7a,D}$	5' – TGA GGT AGT AGG TTG TAT AGT T – 3'
$T_{7a,D,F}$	5' – FITC – TGA GGT AGT AGG TTG TAT AGT T – 3'
$T_{7a,R}$	5' – UGA GGU AGU AGG UUG UAU AGU U – 3'

Table 2.2: *List of nucleic acid probes and targets used in this work. For targets, subscripts indicate if the oligo is DNA (D) or RNA (R), and gives chemical modifications including biotin (bio), Cy3 (Cy3), or fluorescein (F).*

2.2 Equipment Setup

2.2.1 Configuration of Microscope for Polymerization

All experiments were performed using an Axiovert 200 (Zeiss) inverted microscope with a VS25 shutter system (UniBlitz) in place to precisely control UV exposure dose. A 100W HBO mercury lamp in conjunction with wide-range excitation UV filter (11000v2:UV, Chroma) provided irradiation of the desired wavelength. Transparency masks designed using Autocad were printed by CAD/Art Services, Inc. (Bandon, OR) at 10,000 or 20,000 dpi resolution. Each mask was designed to be circular, 2.5 centimeter in diameter, with features typically printed no more then 0.5 centimeters radially from the mask center. During an experiment, a mask was sandwiched between two 25 mm circular glass coverslips (VWR), placed in the first slot of the filter slider bar, and secured with an O-ring. The filter slider was then positioned in the field-stop position of the microscope. Images were processed using NIH Image. The shutter system was controlled using a VMM-D1 shutter driver (UniBlitz), which was prompted using a script written in LabView. *NOTE: Care should be taken not to expose the polymer masks to UV for more than 2 seconds at a time as they tend to burn and deform with long doses.*

2.2.2 Syringe-Pump Sample Delivery

Samples were loaded into plastic syringes (typically 1 ml, BD Falcon) that were mounted on a KDS 100 syringe pump (KD Scientific). Tygon tubing, adapted with a blunt syringe needle at the syringe end and a metal tube adapter at the device end, was used to deliver samples to the microdevice.

2.2.3 Pressure System for Sample Delivery

For particle polymerization, samples were loaded into channels using pipette tips (10 or 200 μl, Molecular BioProducts), connected with rubber tubing (Tygon) to a common pressure source (regulated by a pressure valve, Controlair Inc.). The tips were filled with $\sim 5 - 150$ μl of polymer and inserted into the channel inlet ports. A three way solenoid valve (Burkert, operated manually or via computer) allowed for the oscillation between pressurized (typically ~ 2 psi, high velocity) and ambient-pressure (no flow) states. Visual alignment for polymerization was achieved using a CCD camera (KPM1A, Hitachi) with NIH Image software, and automated valve control was accomplished using a script written in LabView. *NOTE: Typical operating inlet pressures can vary from $< 1 - 4$ psi depending on channel dimensions.*

2.3 General Experimental Protocols

2.3.1 Soft Lithography

Microfluidic channels were molded on four inch silicon wafers using soft lithography with SU-8 photoresists. Briefly, SU-8 photoresist (MicroChem) was spin-coated on a clean silicon wafer for 30 seconds at a speed selected to obtain the desired layer thickness. After a brief 65^oC prebake on a hotplate, the wafer was exposed to UV-irradiation through a transparency mask. The photoresist was then post-baked at 95^oC and subsequently, unexposed photoresist was removed using a developer. PDMS was mixed at a base to curing agent ratio of 10:1. The elastomer was degassed for 30 minutes and poured over the silicon wafer mold. The PDMS was then cured overnight at 65^{o}C. The PDMS mold was peeled from the wafer and individual channels were cut out using a scalpel. Holes for syringe connection were punched out using a blunt ended syringe needle. If desired, wells were cut at the end of the channels using a scalpel. The channels were sonicated in ethanol, rinsed with water, and dried under argon prior to use to remove any debris or dust.

2.3.2 Making PDMS-Coated Slides

PDMS was mixed at a 10:1 base to curing agent ratio and $\sim$ 100 μl was spread crudely over one face a glass slide (24 × 60 mm, VWR) using a spatula. Another glass slide was then placed atop the first, sandwiching the PDMS between. The slides were sheared apart along the long dimension of the slides. This was repeated until the PDMS coating was fairly homogeneous across the two slides (with the exception of a few small bubbles or striations). Coated PDMS slides were placed in a large plastic petri dish and allowed to sit for 30 minutes before baking to remove all inhomogeneities. Slides were then cooked at 65^{o}C for 20 minutes or 2 hours for a partial or full cure, respectfully.

2.3.3 Assembling Microfluidic Devices

Sealing Devices with Plasma

In order to protect areas subsequently used for particle polymerization, square regions of channels and PDMS-coated slides were protected with small pieces of cured PDMS. These two components were then treated with oxygen plasma for 90 seconds on high (Harrick Plasma Cleaner, PDC–32G). The sacrificial PDMS layers were the removed, and the device was sealed to the PDMS-coated slides with the two non-exposed regions aligned. The sealed devices were allowed to bond for at least 15 minutes before use. *NOTE: If the protected area of the channel is too large, this region of the channel may delaminate under flow pressures exceeding only a couple psi. The protected region should be as small as possible, and should also be located as far downstream as possible.*

Sealing Devices via Partial PDMS-Curing

Glass slides were coated with PDMS and partially cured (for 20 minutes at 65^{o}C). Cleaned channels were then placed on the slides and contact-sealed. The assembled devices were then baked for an additional 45 minutes at 65^{o}C. *NOTE: The partial bake time may vary depending on PDMS layer thickness, actual oven temperature, etc. There should be no indication that the PDMS layer is at all liquid when the channel is sealed – if there is, bake times should be increased accordingly.*

2.3.4 Activating Glass Slides with Methacrylates

Glass slides were soaked in 1M sodium hydroxide for at least 30 minutes prior to use. The slides were rinsed thoroughly with deionized water, dried under argon, and treated with oxygen plasma for 90 seconds. In a 6 ml vial, a solution of 2% MPTMS in pH 5 ethanol was prepared and allowed to hydrolyze for 5 minutes. In a plastic petri dish, 250 μl of the MPTMS solution was pipetted on each clean glass slide and rocked back and forth for 3 minutes to assure homogeneous coverage. Excess MPTMS solution was then dabbed off the edge of the slides using an absorbent towel, and the slides were dipped briefly in ethanol to remove excess MPTMS. The slides were placed on a hotplate in a glass petri dish at 75^{o}C for 15 minutes to cure. Lastly, the slides were rinsed thoroughly with ethanol followed by deionized water, and dried under argon.

2.3.5 Cell Culture

Raji B cells and Molt-3 T cells (both from ATCC) were cultured in 150cm^2 tissue culture flasks in an incubator adjusted to 5% CO_2/95% air at 37^{o}C. The cells were incubated in RPMI-1640 media supplemented with 10% fetal bovine serum and 200U/ml penicillin. Prior to use, the cells were centrifuged at 150 g for 5 min. After aspiration of excess media, the cells were resuspended in phosphate buffered saline containing 0.1% bovine serum albumin (BSA) and 2 mM EDTA (both OmniPur).

2.3.6 Suspending Fluorescent Monomers

The fluorescent monomers used in this work (rhodamine-A and fluorescein-MA) were received in powder form and were not particularly soluble in aqueous buffers. Suspension was achieved using PEG TE (PEG_{200} with 10 mM of Tris and 1 mM of EDTA). Depending on the application and desired fluorescence, fluorescent monomers were prepared at 1 or 10 mg/ml in PEG TE and stored at 4^{o}C prior to use.

2.3.7 Preparation of Prepolymers

Monomer precursors were typically mixed in 1.5 ml Eppendorf tubes. First, reactive monomers (ex. PEG-DA) were added to inert monomer species (ex. PEG_{400}, TE, etc.). This mixture was then vortexed for 20 seconds. The photoinitiator (ex. Darocur 1173) was added and the solution was again vortexed for 20 seconds. The monomer solution was spun down in a microcentrifuge for 30 seconds to pellet debris at the bottom before use. *NOTE: It is important to minimize exposure of prepolymers to light and heat. If a monomer solution is to be stored, it should be stored at 4^{o}C in an amber vial.*

2.3.8 Preparation of Prepolymers Containing Beads

Prepolymer solutions prepared using a protocol similar to 2.3.7 were mixed with beads and an appropriate stabilizing surfactant. These prepolymer solutions consisted of PEG-DA_{400} with up to 3.3% Irgacure 2959 photoinitiator, 33% PBS, and 1% surfactant. To generate magnetic bead patterns, we used Dynabeads M-450 epoxy (4.5 μm, Dynal) with 1% Tergitol NP-10 (Sigma) surfactant. Protein-decorated bead patterns were generated using Dynabeads CD19 (4.5 μm, Dynal) in 1% Tween-20 surfactant. *NOTES: (1) Tergitol should not be used with protein-coated beads or cell samples as this non-friendly surfactant leads to protein denaturation and cell lysis. (2) It is important to include at least $\sim$ 33% buffer for prepolymers used with protein-coated beads in order to maintain protein functionality.*

2.3.9 Preparation of Prepolymers Containing DNA

Prepolymers made using protocol 2.3.7 were added to DNA probes (at 10 – 1,000 μM in TE) at a 9:1 ratio. The solutions were vortexed for 20 seconds. This monomer solution was spun down for 30 seconds prior to use. *NOTE: It is important to use at least $\sim$ 33% buffer in order to maintain*

DNA stability. If the amount of buffer is insufficient, the DNA tends to agglomerate, leading to speckled hybridization signals.

2.3.10 Particle Recovery and Rinsing

After polymerization, particles were pipetted from the reservoir or collection tube into a 1.5 ml Eppendorf storage tube, where they were diluted in rinse buffer (typically TET) to 1 ml total volume. The particles were spun down using a microcentrifuge and all but 50 - 100 μl was removed from the top of the liquid and discarded. Fresh buffer was added to the tube and the process was continued 4 to 8×. If a fluorescent monomer was used (rhodamine-MA or fluorescein-A), the particles were rinsed with 200 μl of PEG_{400} and allowed to sit for 3 minutes before rinse buffer was added and the rinse process repeated. After rinsing, the particles were stored in TET at 4^{o}C. *NOTE: it is important to have at least 0.05% Tween-20 in all rinse buffers, as this prevents particle loss via adhesion to tube surfaces. More surfactant may be used if desired, but should be kept below 0.5% to avoid noticeable disruption of biological interactions.*

2.3.11 Hybridization with Nucleic Acids

Hybridization buffer ($HBS_{0.2}$ or $HB_{0.5}$, typically 40 μl) and particles (typically 5 μl) were pipetted into 0.65 ml Eppendorf tubes. The nucleic acid samples (5 μl) were then added to the tubes to obtain the desired concentration. The samples were incubated at the desired temperature and duration using a thermomixer (Quantifoil Rio) with a mixing speed of 1800 rpm. *NOTE: Targets include unlabelled, biotinylated, or fluorophore-labelled DNA or RNA. For this work, the relative signal brightness for a hybridization with respect to fluorophore was: SAPE > PicoGreen > Cy3, FITC.*

2.3.12 Labelling Biotinylated Targets

After hybridization, particles were rinsed 1× with TET and 1× with PBST. Then, SAPE was diluted 1:50 in PBS and added to obtain a final dilution of 1:500. The samples were then incubated at RT for 30 min with mixing at 1800 rpm. Before imaging, particles were rinsed 2× with TET.

2.3.13 Direct-Labelling of Hybridized Targets

After hybridization, particles were rinsed 1× with TET and then 1× with NEB2, leaving all but 50 μl of liquid in each tube. Then, 1 unit of Exonuclease I (New England Biosciences) was added to each tube, which was then centrifuged for 3 seconds to ensure all liquid was at the bottom. The samples were then incubated at 37^{o}C for 30 minutes on a thermomixer with mixing at 1800 rpm. Samples were rinsed 1× with TET and then 1× with PTET. After centrifuging for 30 seconds, all but 50 μl of buffer was pipetted from each sample and 5 μl of PicoGreen (Invitrogen), diluted 1:50 in TE, was added to each tube for a final dilution of $\sim$ 1:500. The samples were then mixed for 15 minutes at RT with mixing at 1800 rpm. At this point, the particles were ready for imaging with no additional rinsing. *NOTES: (1) For direct-labelling, it is very important not to use any buffers that contain SDS. (2) As PicoGreen has a tendency to bind to glass surfaces, PDMS or another resistant substrate should be used. The preferred method of analysis is to sandwich a sample (~ 40 μl between 2 PDMS-coated slides. (3) The addition of PEG to buffer tends to increase the fluorescent signal* *of PicoGreen, but because these polymers tend to be slightly acidic, care should be taken to obtain pH ∼ 7 – 8.*

2.3.14 Imaging Particles

Imaging for Visualization

Particles were pipetted into PDMS reservoirs that were mounted on an inverted microscope (Axiovert 200). Low-resolution, black and white images were captured in NIH Image using a CCD camera (KPM1A, Hitachi) mounted to the sideport of the microscope. High-resolution, color images were captured using a Nikon D200 digital SLR camera. For fluorescence images, the appropriate filter set was used (rhodamine-b: XF101-2, fluorescein: XF100-2 or XF100-3, PicoGreen: XF100-3).

Imaging for Quantitative Analysis

Rinsed particles were pipetted into PDMS reservoirs on an inverted microscope with an Exfo UV Lamp. Ten-frame, one-second movies were taken in NIH Image using an EB-CCD camera (C7190-20, Hamamatsu) mounted to the sideport of the microscope. The movies were averaged over all 10 frames and saved as a single image. Images were analyzed using ImageJ software.

CHAPTER 3

Bead-Patterned Hydrogels

The ability to pattern magnetic and/or biologically-active microbeads in a bio-inert environment has important implications for the development of diagnostic, therapeutic, and basic science tools for lab-on-a-chip technologies. Microbeads suspended in aqueous solutions are commonly used in microfluidic devices for chemical reaction and cell binding due to their excellent specificity, wide availability, and appreciable monodispersity. In addition to being industrially standardized, microbeads are available with several protein, electrostatic, or reactive coatings and range in size from hundreds of nanometers to several microns. Methods for the precise manipulation and positioning of microbeads (or bead-bound biological targets) at a microscale may have significant impact on the development of new medical devices.

To address the need for simpler, more reliable techniques, we have developed a method to precisely pattern both magnetic material and proteins in a bio-inert polymer using photopolymerization of bead-containing hydrogel precursors. As such, our approach combines patterning and passivation into a single process. Additionally, the simple method we present requires minimal reagents, only around an hour to complete, and results in stable patterns that are covalently linked to glass substrates. The material in this chapter was reproduced from Pregibon, Toner, and Doyle, *Langmuir*, 2006 [121].

3.1 Description of Bead-Patterened Hydrogels

We demonstrate a simple technique to fabricate intricate monolayer patterns of paramagnetic and antibody-decorated microbeads on glass substrates via photopolymerization using a standard inverted microscope. Our approach provides a simple, inexpensive, versatile method for generating free-standing or poly(ethylene glycol)-surrounded magnetic and biologically active patterns. Using magnetic and fluid forces, we demonstrate the ability to pattern self-assembled, dispersed-bead patterns, and also close-packed bead patterns. The scheme we use for polymerization is similar to that demonstrated by Love et al. [122]. This microscope-based projection lithography (Setup 2.2.1), which we employed with a 20X objective (providing an overall 7.78X reduction of feature sizes printed on our masks), allows us to fabricate structures over regions greater than 1 mm × 1 mm with resolution near 1 μm using repeated short dose pulsing.

3.2 Principles of Patterning

Bead-embedded PEG microstructures were fabricated by photopolymerizing mixtures of beads and UV-sensitive prepolymer (protocol 2.3.8) in low height channels 9.6 μm tall for disperse-bead patterns or 6.1 μm tall for packed patterns. A schematic of the patterning protocol we have developed for creating dispersed patterns is shown in Figure 3.1; the method is discussed in more detail later. We postulate that during the free-radical reaction, the bifunctional PEG molecules covalently link with the methacrylate-treated glass substrate and also interact with the microbeads, either by means of molecular entanglement or chemical linkage, rendering the beads immobilized on the substrate. Once the primary bead pattern is polymerized to the substrate, the surface can be rinsed and secondary patterns of beads or PEG can be deposited.

It is very important to account for the diffusion of oxygen through PDMS when polymerizing low-profile (less than 10 μm) structures as we have. Oxygen is known to inhibit free-radical polymerization [123]. During the crosslinking reaction, oxygen diffuses rapidly through the PDMS walls and into the monomer, necessitating the use of a relatively high concentration of photoinitiator (or excitation) when polymerizing thin films. Under the conditions we use, there is always an unreacted, liquid "inhibition layer" near the PDMS surface. We have visually confirmed the presence of this inhibition layer near PDMS sidewalls by UV-exposing regions that extend beyond the width of an oligomer-filled channel (data not shown). Similar results are observed when UV-exposing across an oligomer/air bubble interface, thus supporting the proposed mechanism of oxygen inhibition.

Because of this phenomenon, we postulate that polymerization always initiates from the glass surface (where oxygen must diffuse the furthest) and proceeds toward the PDMS to a height that is dependent on initiator concentration, UV intensity, and exposure duration [124]. To validate this postulation, we polymerized PEG structures at various doses with UV irradiation both through the glass substrate and also through the PDMS as shown in Figure 3.2. Using a precursor solution of 2.5% Irgacure 2959 photoinitiator in PEG-DA oligomer, we show that the heights of the square structures asymptotically approach a value near 9 μm (in a channel 9.6 μm tall) with increasing exposure dose. Most importantly, the structures were similar in heights, regardless of irradiation direction (through glass or PDMS). We have also demonstrated that the structure heights approached different values when the amount of photoinitiator or UV intensity were altered (not shown).

Beyond controlling structure height, we also exploit the opacity of the beads used to generate patterns of beads whose surfaces are exposed in a PEG platform. Thus, by varying the direction

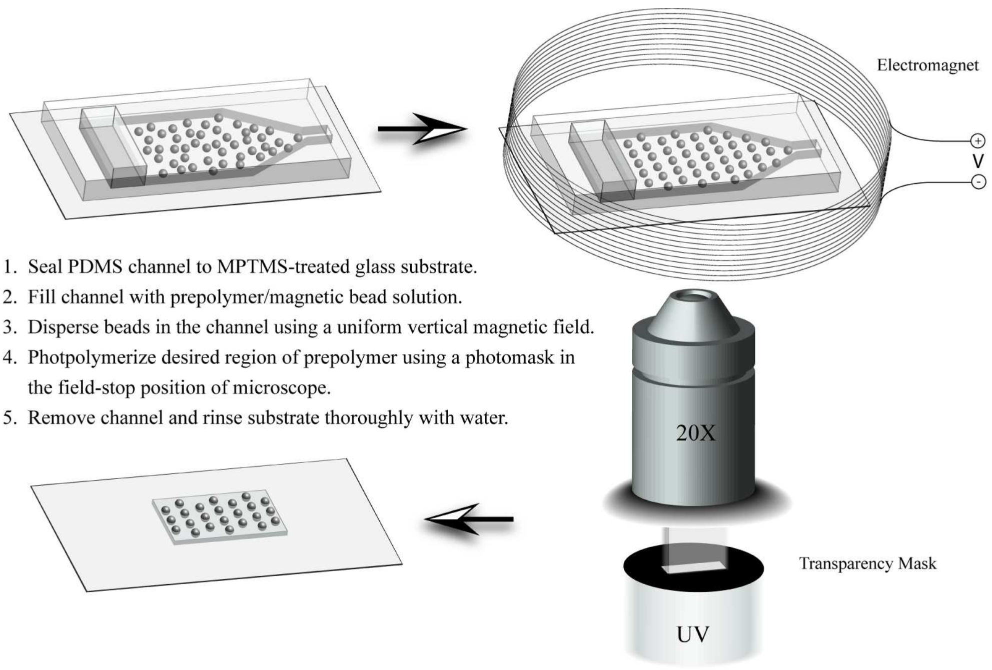

1. Seal PDMS channel to MPTMS-treated glass substrate.
2. Fill channel with prepolymer/magnetic bead solution.
3. Disperse beads in the channel using a uniform vertical magnetic field.
4. Photpolymerize desired region of prepolymer using a photomask in the field-stop position of microscope.
5. Remove channel and rinse substrate thoroughly with water.

Fig. 3.1: *Schematic of structure polymerization for dispersed magnetic bead patterns.*

of polymerization (i.e. through the glass or through the PDMS channel), we can generate exposed or totally encapsulated bead patterns. We have patterned encapsulated magnetic microbeads as well as exposed protein-decorated microbeads in order to perform different functions in microfluidic devices.

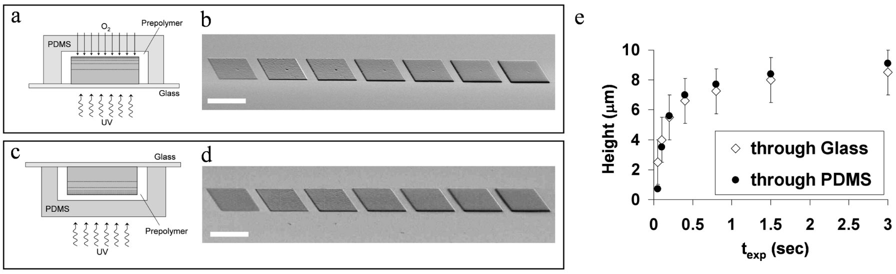

Fig. 3.2: *Variation of structure height with exposure dose when UV-irradiated through the glass substrate (a, b) or PDMS channel (c, d). (a, c) Schematic of hydrogel polymerization through glass substrate or PDMS channel. (b, d) Scanning electron micrograph of PEG structures polymerized for 0.05, 0.1, 0.2, 0.4, 0.8, 1.5, and 3 seconds in a 9.6 µm-tall channel. (e) Graph showing structure height with varying UV exposure times, estimated from SEM images shown in (b) and (d). The height measurement uncertainty (shown as error bars in (e)) is due to the SEM image resolution (pixel size). Scale bars are 200 µm.*

3.3 Dispersed-Bead Magnetic Patterns

We used the self-assembly of colloidal monolayers in a homogeneous magnetic field to generated patterns of paramagnetic microbeads semi-regularly dispersed in PEG hydrogels. The protocol for fabricating a dispersed-bead pattern is outlined in Figure 3.1 as mentioned before. Briefly, we treated a glass slide with MPTMS (Protocol 2.3.4), bonded a wide, 9.6 μm tall PDMS channel to the treated glass by conformal contact, filled the channel with prepolymer solution (Dynabeads M-450 epoxy dispersed in 2.5% Irgacure 2959/1% Tergitol NP-10/96.5% PEG-DA$_{400}$) using capillary action, dispersed the beads using an electromagnet-generated vertical magnetic field (10 – 30 mT), and polymerized mask-defined shapes using a 20× microscope objective for 0.5 – 3 sec. The structures were then rinsed thoroughly with deionized water and dried under argon. The rectangular shapes we polymerized were approximately 200 × 500 μm. By adjusting the concentration of microbeads in the prepolymer solution, were able to tune the spacing between patterned beads (approximately 53, 40, and 28 μm) as shown in Figure 3.3.

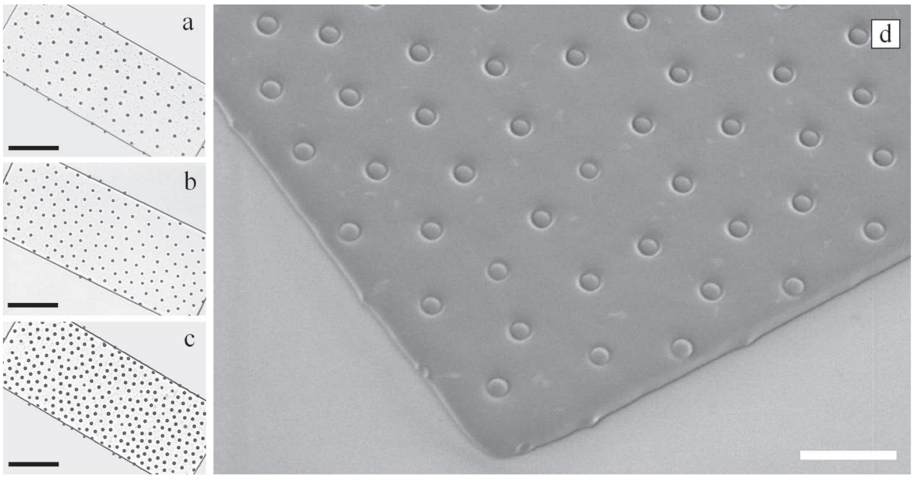

Fig. 3.3: *Dispersed magnetic bead patterns in rectangular PEG structures. (a) – (c) Bright field images of PEG structures with varying concentrations of beads. (d) Scanning electron micrograph of structure shown in (c). Scale bars: 100 μm (a – c); 20 μm (d).*

We also fabricated composite pattern structures with pads of dispersed beads in rectangular PEG platforms as shown in Figure 3.4. Circular pads of dispersed beads were polymerized as previously described for 0.5 sec. We then rinsed excess polymer from the slide, dried the pattern under argon, and placed a clean 9.6 μm-tall channel over the pattern. The channel was filled with a bead-free prepolymer solution. We changed the mask in the microscope and polymerized a rectangular structure around the magnetic bead pads for 2 sec.

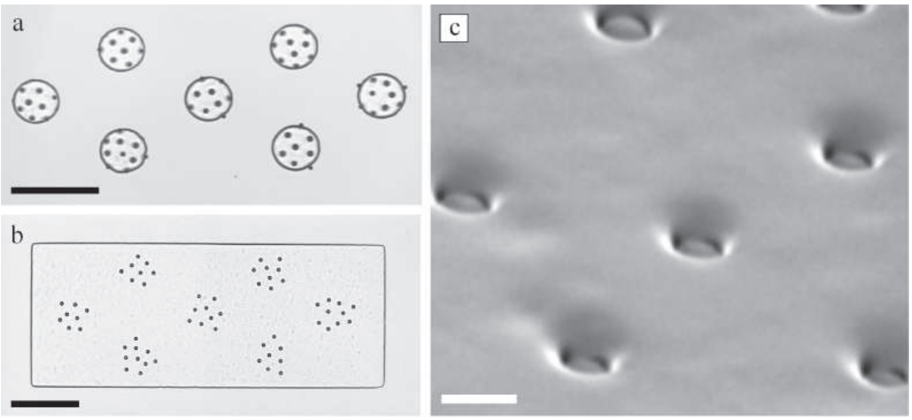

Fig. 3.4: *(a) Bright field image of magnetic bead islands polymerized to a glass substrate. (b) Composite structure with PEG rectangle polymerized around the magnetic bead islands. (c) Scanning electron micrograph of exposed beads in PEG structure. Scale Bars: 100 μm (a, b); 5 μm (c).*

3.4 Packed-Bead Magnetic Patterns

Close-packed bead patterns were generated using a protocol slightly different from that used for the dispersed bead patterns. In order to create a tightly-packed array of microbeads, it is essential to use a channel whose height is only slightly greater than a bead diameter and that has a constriction small enough to impair bead passage. Instead of designing multi-tiered microchannels for this purpose, we simply polymerized a small slug of prepolymer in a 6.1 μm-tall channel to block the bead flow. As previously mentioned, the gel does not polymerize all the way to the PDMS surface, leaving room for fluid flow while blocking the beads from passing.

With the constriction in place, we flowed a solution of Dynabeads in 1% surfactant (in deionized water) through the channel using suction from a syringe. Once the wide region of the channel was loosely packed with beads, we placed the device directly on top of the water bath of an ultrasonic cleaner for 3 sec to facilitate the close-packing of beads within the channel. We then removed excess fluid from the reagent well and added our prepolymer solution (2.5% Irgacure 2959/1% Tergitol NP-10/96.5% PEG-DA), filling in the void space between the packed beads. As before, we polymerized mask-defined patterns for 0.5 – 3 seconds, removed the PDMS channel, rinsed the patterns with deionized water, and dried the substrate under argon. If desired, we placed a 9.6 μm-tall channel over the bead pattern and polymerized PEG structures around the bead patterns as described before.

Using a narrow, 5 μm-wide PDMS channel, we have also demonstrated the ability to pattern a single rail of magnetic beads totally encapsulated in PEG. When polymerizing such small structures, it was necessary not only to use a high concentration of photoinitiator, but also to soak the PDMS channel in 0.1 g/ml solution of 1-hydroxycyclohexyl phenyl ketone photoinitiator (Aldrich) for 10 min prior to use. Examples of the various packed bead patterns we have generated are shown in Figure 3.5.

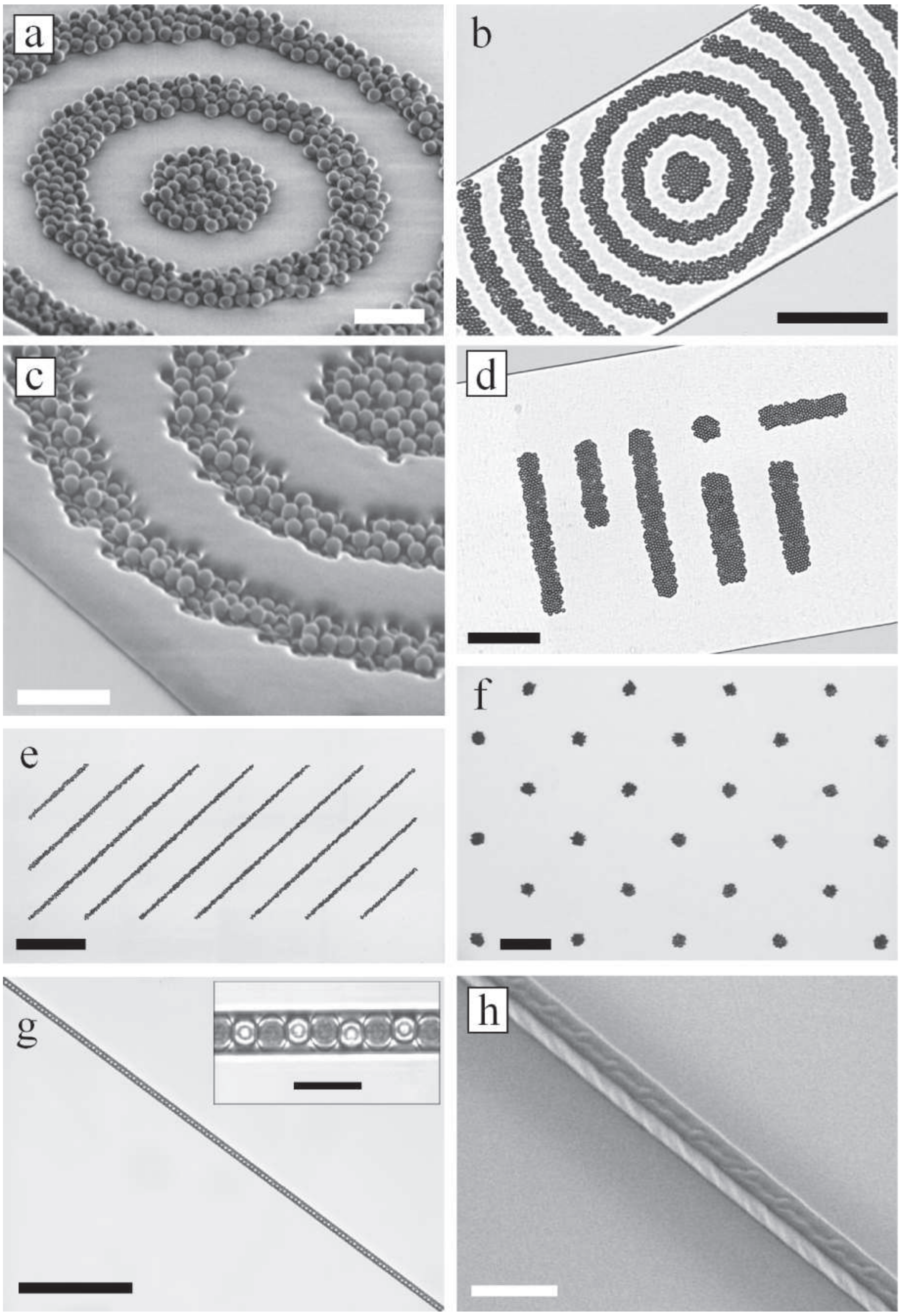

Fig. 3.5: *(a) Scanning electron micrograph of magnetic beads patterned in a target shape on a glass substrate. (b) Bright field image and (c) scanning electron micrograph of a target bead pattern with a rectangular PEG structure polymerized around it from below the substrate. (d) Bright field image of another packed-bead pattern with a rectangular PEG film polymerized around it. (e) Lines and (f) dots patterned to glass over lengths greater than 1 μm. (g) Bright field image with close-up inlay of a single rail of magnetic beads encapsulated in PEG. (h) Scanning electron micrograph of the rail in (g), showing that the beads are completely encapsulated in PEG. Scale bars: 20 μm (a,c); 100 μm (b, d, f, g); 200 μm (e); 10 μm (g inlay, h).*

3.5 Exposed Versus Encapsulated Bead Patterns

As mentioned, we have fabricated both exposed and PEG-encapsulated bead patterns. The UV irradiation cannot penetrate the magnetite-loaded microbeads due to their high opacity. The beads act as masks, preventing the monomer from polymerizing on the side of the beads opposite to the light source. Exposed-bead patterns are desirable when patterning surface-active beads. Conversely, patterns encapsulated in thin PEG films may be more useful when exploiting the beads solely for their magnetic properties while avoiding non-specific protein and cell adhesion. In order to generate PEG-encapsulated bead patterns, we simply inverted the device and polymerized the PEG structures through the PDMS channel. When generating encapsulated patterns, we used channels made from thin slabs ($\sim$ 1 mm) of PDMS to fit within the working distance for the microscope objective. From our experience, thinner slabs of PDMS also provided the highest fidelity structures. Figure 3.6 shows beads patterned to a glass substrate with subsequent polymerization of PEG around the bead cluster from below and above the structure.

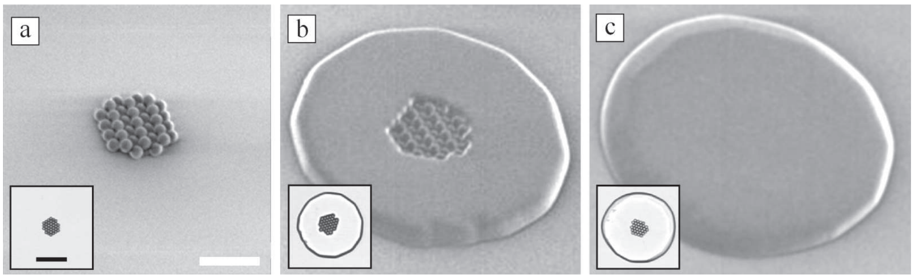

Fig. 3.6: *Scanning electron micrographs of (a) free-standing packed bead cluster polymerized to glass, (b) cluster with outer PEG structure polymerized from below the glass substrate, and (c) cluster with outer PEG structure polymerized through PDMS channel, each with bright field image inlays. Scale bars: 20 μm (a – c); 50 μm (a – c inlays).*

3.6 Protein-Bound-Bead Patterns

All of the aforementioned structures generated using magnetic microbeads can also be fabricated using protein-decorated beads with slight variations of the reagents used. Firstly, it is very important to use Tween-20, or another bio-friendly, non-ionic surfactant, in all processing steps. The proteins bound to the microbeads tend to stick to the methacrylate-modified glass surface in absence of surfactant. The surfactant appears to protect the proteins during processing, helping retain protein activity while patterning. The prepolymer solution we use when patterning the anti-CD19 coated microbeads was 3.3% Irgacure 2595/33.3% PBS/63.4%PEG-DA. The dilution of prepolymer with PBS, like the addition of surfactant, appeared to help maintain the stability of the protein during the polymerization process. In addition to these alterations, we also flushed the channel with 10% BSA in PBS prior to removing the channel after pattern polymerization. We rinsed the patterns with water and while still wet, added a few microliters of 30% glycerol atop the wet pattern. The glycerol protected the proteins from drying, which is known to compromise protein function [125].

For many applications, it is desirable to capture multiple specific cell types or proteins in well-defined patterns. Bead-patterned hydrogels containing several chemically-unique beads may provide an efficient, inexpensive platform to accomplish this. The patterning of diverse microbeads can be acheived by either (1) sequentially immobilizing pads of beads in a composite pattern similar to that shown in Figure 4, (2) patterning beads in adjacent channels (each filled with a unique bead type), or (3) mixing bead types (potentially fluorescently barcoded for later identification) in the oligomer solution and generating chemically randomized bead patterns.

3.7 Cell Capture Experiments

To demonstrate the utility of our patterning method, we fabricated microfluidic devices to (1) capture magnetic-bound cells on bio-inert magnetic pads and (2) directly capture cells on patterned, antibody-decorated beads. The patterns we generated are by no means optimized for these applications, but were used solely to show exploitation of the magnetic and bio-active nature of two bead-patterned hydrogels. The cellular specificity of immunomagnetic microbeads has been well documented [126] and not is not emphasized in our experiments. We simply demonstrated selective binding of the beads to targeted B cells as shown in Figure 3.7a.

3.7.1 Capture of Magnetic-Bound B Cells

We patterned PEG-encapsulated clusters of magnetic beads to filter magnetic-bound B cells from T cells. An encapsulated pattern was used to deter non-specific cell adhesion to the epoxy (glycidyl ether) magnetic bead surfaces. The microfluidic device we constructed consisted of a long 500 μm wide, 75 μm tall microchannel aligned over the PEG-encapsulated bead pattern. We positioned a circular electromagnet about the device, using a power source to control the current and hence magnetic field generated. We incubated Raji B cells and Molt-3 T cells with Dynabeads CD19 as recommended by the bead supplier for 10 min. After flushing the channel for 20 minutes with 10% BSA solution, the cell mixture was flowed through the channel. With a magnetic field strength of $\sim$20 mT, we were able to capture bead-bound B cells over the patterned magnetic clusters as shown in Figure 3.7. The magnetic-bound cells were released into the flow when the magnetic field was turned off.

3.7.2 Direct Capture of B Cells on Patterned Beads

Using the protein-friendly protocol previously described, we patterned anti-CD19 beads directly to a glass substrate in an arbitrary target shape. We aligned a PDMS microchannel 1 mm wide and 50 μm tall over the pattern and flushed it with 10% BSA for 20 minutes. We flowed a solution of B cells in through device, capturing the cells directly on the bead patterns as show in Figure 3.8. The cells adhered very well to the patterns and remained attached even under considerable shear stresses. It appears as though very little protein functionality was lost in the bead patterning process.

The intent of this experiment was to show that the antibodies conjugated to the surface of the beads maintained activity through what might seem to be a harsh process with high-intensity UV exposure, free-radical formation, exposure to a hydrophobic photoinitiator, etc. We are not suggesting (or denying) that this method is superior to systems that utilize surface patterning for the specific application of cell capture, but used this scenario as a proof-of-principle. We

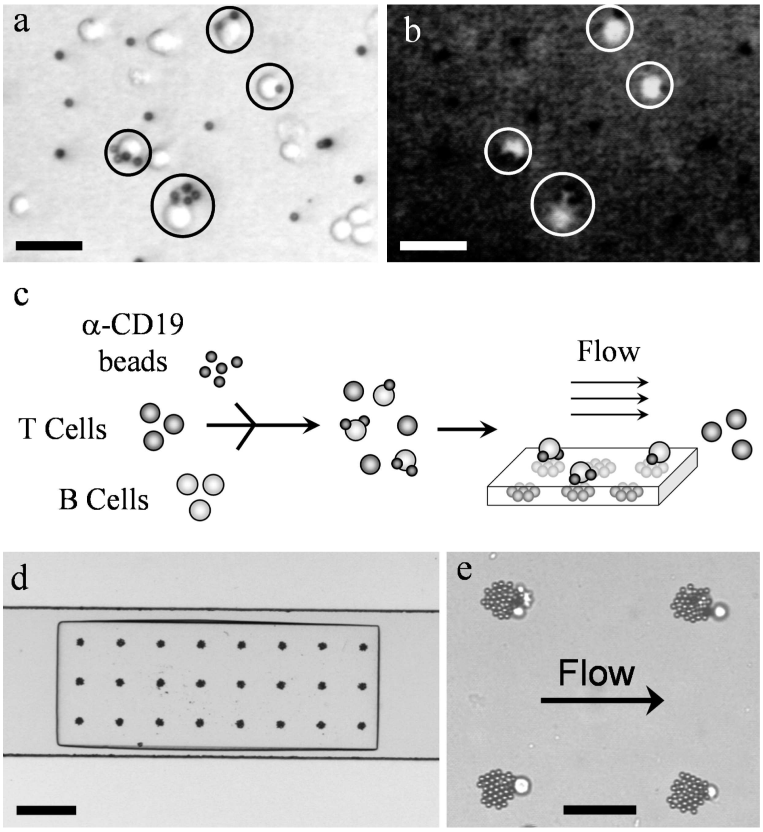

Fig. 3.7: *(a) Bright field image of B and T cells incubated with α-CD19 decorated microbeads (with bead-bound cells circled). (b) Fluorescence image of cells in (a), showing the specificity of the beads for the fluorescently dyed B cells. (c) Schematic of magnetic-bound cell capture experiment. (d) Bright field image of PEG-encapsulated magnetic bead cluster platform in a microchannel. (e) Bead-bound B cells captured over the magnetic pads in a flow. Scale bars: 30 μm (a,b); 200 μm (d); 50 μm (e).*

would like to emphasize that for certain biological applications, the use of patterned beads may have advantageous features including three-dimensionality and ultra-small antibody spotting. The spherical nature of the beads provides a higher protein density per planar area than flat surfaces and a "bumpy" contour that might promote better interaction between flowing cells and the antibody-decorated substrate. In addition, the use of monodisperse, antibody-decorated beads provides a means to make very small (< 5 μm), homogeneous spots of various chemistries. This is very difficult to achieve using traditional approaches and may be useful when fabricating protein or DNA arrays.

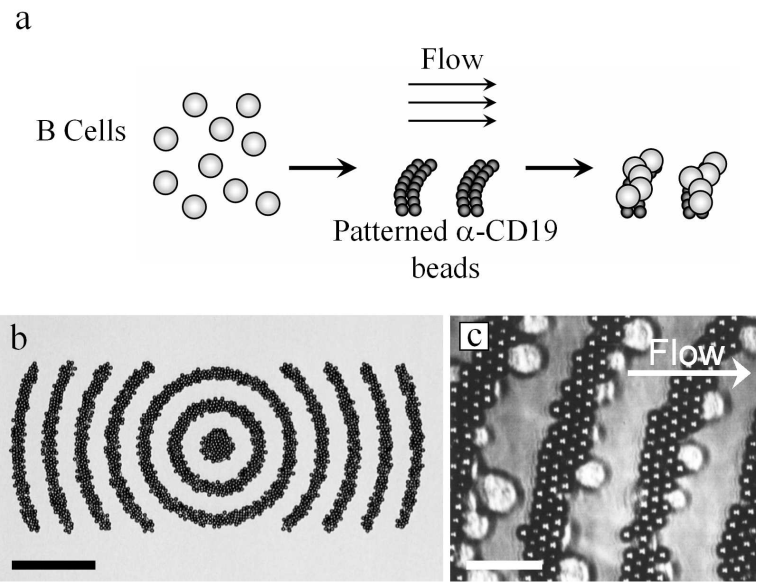

Fig. 3.8: *(a) Schematic of direct cell capture experiment. (b) Bright field image of patterned anti-CD19 microbeads on a glass substrate. (c) Cells captured directly on the patterned beads in a fluid flow. Scale bars: 100 μm (b); 25 μm (c).*

3.8 Conclusions

We have developed a new method to pattern magnetically-active and protein-decorated microbeads on glass substrates or in bio-inert PEG platforms for use in microfluidic separations. The process is fast, inexpensive, versatile, and shows potential for applications in cell sorting, generating protein or nucleic acid microarrays, and patterning biosensor arrays. We have exploited PEG-encapsulated magnetic patterns to filter bead-bound B cells from T cells and also directly capture B cells on exposed bead patterns. Beyond the development of bead-patterned, bio-inert substrates, we have discovered that the polymerization of a monomer species in a microdevice is inhibited at PDMS surfaces – a phenomenon that enables the production of free-floating structures in an all-PDMS device. The application of this concept to the production of functional microparticles provides the foundation for the rest of the material covered in this thesis.

CHAPTER 4

Flow Lithography

The discovery that free-radical polymerization was inhibited near PDMS surfaces, as discussed in the previous chapter, led to the advent of flow lithography – a powerful technique that allows continuous lithographic "printing" and flowing of polymeric microparticles in a microfluidic device. Previous approaches to particle synthesis were either batch processes [127, 128, 129, 130, 131] or flow-through microfluidic schemes [106, 107, 108, 109, 110, 132] that were based on two-phase systems, limiting the throughput, shape, and functionality of the particles generated. In contrast to these methods, flow lithography can be used to generate morphologically-complex particles, bearing multiple distinct regions, from a broad range of precursor materials. The method is straightforward and can be implemented using a standard fluorescence microscope.

As discussed in this chapter, flow lithography can be implemented as a continuous-flow process (Continuous Flow Lithography, CFL) or with a stop-polymerize-flow scheme (Stop Flow Lithography, SFL). The work presented here was done mostly in collaboration with Dhananjay Dendukuri, with help from Jesse Collins (CFL), Shelley Gu (SFL) and Stephen Maltas (Armored Droplets). Much of this chapter was reproduced from Dendukuri, Pregibon, Collins, Hatton, Doyle, *Nature Materials*, 2006 [124] and Dendukuri, Gu, Pregibon, Hatton, Doyle, *Lab-on-a-Chip*, 2007 [133].

4.1 Continuous-Flow Lithography

Continuous-Flow Lithography is accomplished by simply flowing a UV-sensitive monomer through a micrcrofluidic device and lithographically printing microparticles on the moving stream. In a representative experiment, an acrylate oligomer (typically PEG-DA) containing a photosensitive initiator was passed through a rectangular, all-PDMS microfluidic device using syringe-pump driven flow as shown in Figure 4.1a (see setups 2.2.1, 2.2.2, and protocols 2.3.2, 2.3.3, 2.3.7). Particle arrays of mask-defined shapes (see squares in Figure 4.1b) were formed by exposing the flowing oligomer to controlled pulses of UV light using an inverted microscope and collected in the device reservoir (Figure 4.2). Unless otherwise stated, particles were made using monomers consisting of PEG-DA$_{400}$ with 5% Darocur 1173.

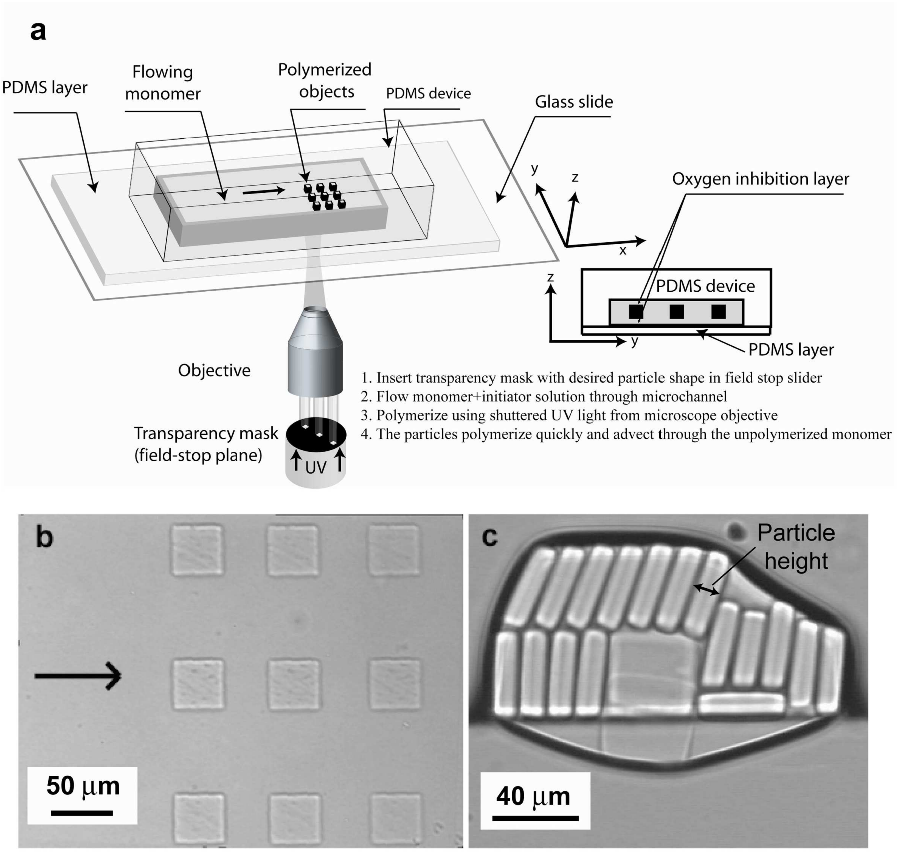
a
PDMS layer
Flowing monomer
Polymerized objects
PDMS device
Glass slide
y
z
x
Oxygen inhibition layer
z
PDMS device
y
PDMS layer
Objective
Transparency mask (field-stop plane)
UV
b
50 µm
c
Particle height
40 µm

1. Insert transparency mask with desired particle shape in field stop slider
2. Flow monomer+initiator solution through microchannel
3. Polymerize using shuttered UV light from microscope objective
4. The particles polymerize quickly and advect through the unpolymerized monomer

Fig. 4.1: *Experimental Setup. (a) Schematic of setup, where bursts of UV light are shown through a transparency mask and microscope objective onto a flowing monomer stream in an all-PDMS microdevice. (b) A brightfield image (xy plane) of an array of cuboids moving through the unpolymerized monomer. (c) A cross-sectional view of the cuboids seen in (b) upon collection in a droplet that has turned most particles on their sides.*

Rapid polymerization kinetics permitted the particles to form quickly (< 100 ms) while oxygen-aided inhibition near the PDMS surfaces allowed for particle flow within the unpolymerized oligomer stream. This serendipitous ability of the particles to flow is because molecular oxygen diffusing through the PDMS surfaces reacts with initiator species to form chain-terminating peroxide radicals [134], leaving a non-polymerized lubricating layer near the PDMS walls (inset of Figure 4.1a). The phenomenon of oxygen inhibition at the PDMS walls is applicable to any free-radical polymerization, rendering our approach suitable for a broad range of polymer chemistries.

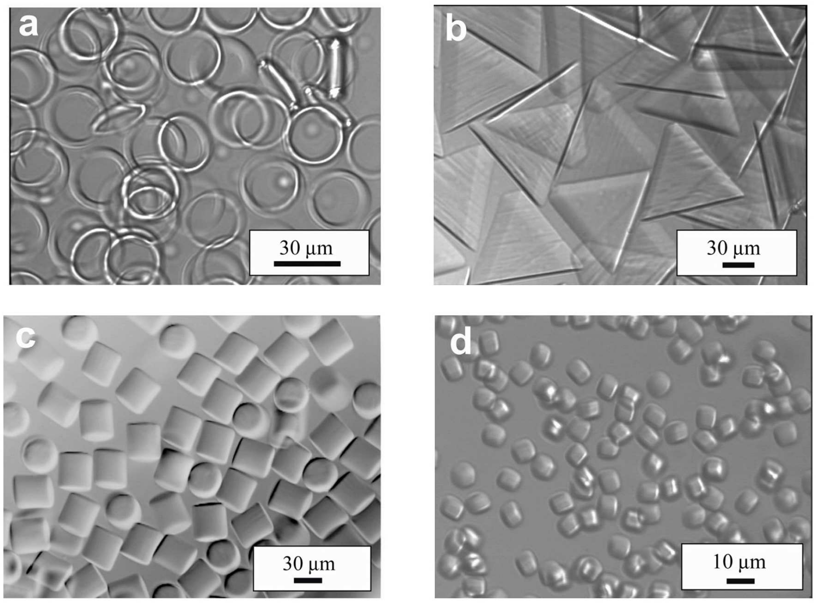

Fig. 4.2: *Differential Interference Contrast images of collections of particles. Particles were generated in a high-throughput fashion and collected in a reservoir. (a) Rings formed using a 9.6 μm high channel and the 20× objective . (b) Triangles formed in a 38 μm high channel using a triangular mask and the 20× objective. (c) Cylinders were synthesized using circular masks in channels 38 μm tall using the 20× objective. (d) Colloidal cuboids synthesized using a square mask and the 20× objective in a 9.6 μm high channel.*

The shape of the particles in the x-y plane (Figure 4.1b) is determined by the shape of the feature used on the transparency mask (Figure 4.1a) while the z-plane projection (shown in Figure 4.1c) is dependent on the height of the channel used and the thickness of the oxygen inhibition layer. Using our microscope projection setup, the transparency feature sizes were reduced by a factor dictated by the objective used, ranging from 7.8 times using a 20× objective to 39 times using a 100× objective. For example, using the 20× objective, a 350 μm square mask feature was used to synthesize cuboids (rectangular parallelepiped objects) that had 45 μm sides (350 μm/7.8 = 45 μm) in the x-y plane (Figure 4.1b). The height of the particles was equal to the height of the channel minus the thickness of the inhibition layers. Cuboids with a height of 15 μm (Figure 4.1c) were synthesized in a 20 μm high channel because of the 2.5 μm thick oxygen inhibition layer at both the top and bottom walls of the device. By designing masks with varied features and selecting channels of differing heights, we synthesized particles of several distinctive shapes, sizes and aspect ratios (Figures 4.2, 4.3).

We have synthesized various polygonal shapes such as triangles, squares, and hexagons (Figures 4.3a – c); colloidal entities (Figure 4.3d); high aspect ratio objects such as posts with circular, triangular, and square cross-sections (Figures 4.3e, f); and non-symmetric or curved objects (Figures 4.3g – i). All the particles showed good fidelity to the original mask features and had straight sidewalls.

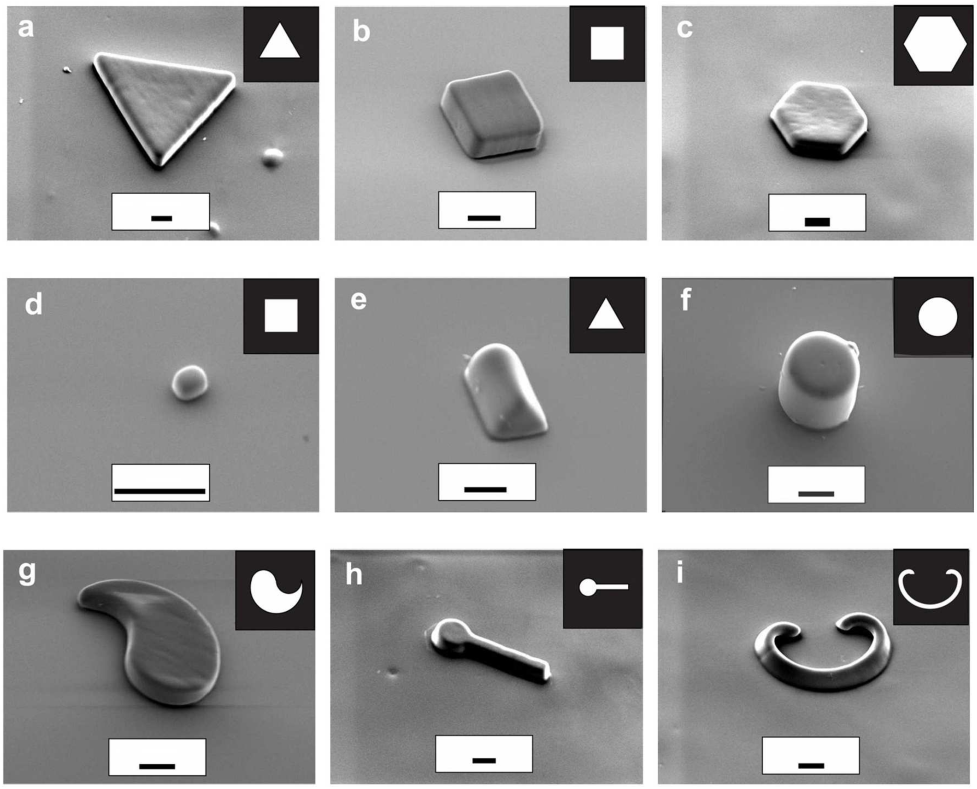

Fig. 4.3: *SEM images of particles. Microparticles formed using a 20× objective (except d was formed using a 40× objective) were washed before being observed using SEM. The scale bar in all the figures is 10 μm. (a – c) Flat polygonal structures that were formed in a channel of height 20 μm. (d) A colloidal cuboid that was formed in a channel of height 9.6 μm. (e – f) High aspect ratio structures with different cross-sections that were formed in a channel of height 38 μm. (g – i) Curved particles that were all formed in a channel of height 20 μm. The inset in the figure shows the transparency mask feature that was used to make the corresponding particle.*

4.1.1 Synthesis of Janus and Multifunctional Particles

Entities with multiple chemistries [135, 136, 137] are proving to be important in sorting and targeting applications [138] or in self-assembly studies [103]. Using our technique, particles with two or more functionalities may be easily and controllably synthesized. Exploiting the diffusion limited mixing seen in laminar flow (Figures 4.4a, b), we have synthesized bi-functional Janus particles (Figures 4.4c – e) by polymerizing rectangular particles across the interface of co-flowing oligomer and rhodamine-labelled oligomer streams. By controlling the location of the interface using the flow rates of the streams or the location of the projected light by moving the microscope stage, we can synthesize particles that contain variable proportions of different chemistries. By simply flowing multiple, concurrent, laminar streams through a microfluidic device and polymerizing particles across these streams, our approach may be used to generate particles with several adjacent chemistries. The ability to tune the proportion of so many chemistries allows for great flexibility in the design of barcoded particles.

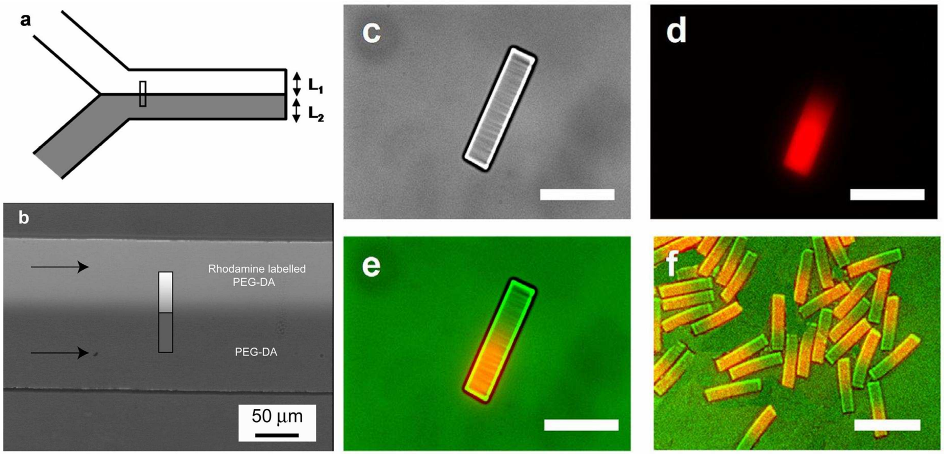

Fig. 4.4: *Synthesis of Janus particles. (a) A cartoon showing the synthesis of Janus (two-faced) particles. The widths of the streams, L1 and L2 can be altered by changing the flow rates of the streams. (b) Two streams containing PEG-DA (grey) and PEG-DA with rhodamine labelled cross-linker (white) are co-flowed through a channel. A cartoon representing the formation of a bar-shaped particle 130 µm in length and 20 µm width is overlaid on the picture. Diffusion limited mixing seen in laminar flow is exploited to ensure the streams flow distinctly. (c) DIC image of a Janus particle. (d) Fluorescence microscopy image of the particle in (c). The rhodamine labelled portion is seen in red. (e) An overlaid image of the entire particle showing both the fluorescently labelled (orange) and the non-labelled (green) sections. The scalebar in figures (c – e) is 50 µm. (f) Multiple Janus particles with the fluorescent portion shown in orange. The scalebar is 100 µm.*

4.1.2 Armored Droplets

Beyond polymerization in one-phase systems, continuous flow lithography can be implemented in two-phase systems. By co-flowing hydrophilic and hydrophobic monomers, particles have been made to mimic micro-scale surfactants [139]. Here, we will show that CFL can also be used with *discrete* droplets in a two-phase system. Using active, computer-based monitoring and shutter control, it is possible to detect and trap mobile droplets in ring-shaped "2-D cages" when using a monomeric continuous phase.

Fluidic microdroplets are commonly used as discrete vessels for chemical and biological reaction. Emulsion droplets are formed when one fluid is dispersed in a second, immiscible fluid, providing isolated, nanoliter-scale chambers. These entities have been used for a variety of appications including emulsion polymerase chain reaction (emPCR) [140], DNA sequencing [141], enzyme engineering [142], glucose detection [143], and protein crystallization [51]. Photosensitive polymers have also been used in droplets, enabling a method to produce solid particles upon UV-irradiation [144, 108].

Droplets are often formed using microfluidic devices designed to shear or pinch off small moieties of a "disperse" fluidic phase into an immiscible, "continuous" phase. Droplet formation relies heavily on device geometry and the surface chemistries of the system. Flow-focusing [145] and T-junction [146] geometries are the most commonly used designs for the continuous generation of monodisperse fluidic droplets. These designs have been studied in depth and devices can now be made to generate droplets of varying size using many different immiscible fluidic systems.

Droplet stability is dictated by the interfacial tension between the two fluid phases. This property is unique for each pair of liquids and can be modified by the addition of surfactants or emulsifying agents. These chemicals help to stabilize droplets against coalescence upon contact [147] and can be beneficial when close packing droplets. Unfortunately, surfactants can interfere with chemical reactions occurring within the droplets and would ideally not be used.

It is of great scientific interest to immobilize, array, and analyze droplets, particularly those containing biological entities such as cells or proteins. This has been accomplished by either (1) stopping flow so the droplets remain immobilized periodically along narrow channels [51] or (2) using double emulsion systems to encapsulate droplets in solid shells [148]. Double emulsions exploit the use of three fluid streams such that one droplet phase is encapsulated in a second droplet, which often contains a photosensitive polymer. Upon UV-irradiation, the outer shell of the droplet is crosslinked and solidified. These shells protect the encapsulated droplets, allowing the particles to be arrayed.

Although solid shells protect droplets from coalescing, they also make it difficult to recover droplet contents. This is necessary when selecting cells, enzymes, or other rare entities that exhibit desirable characteristics. In addition, it is often desirable maximize the number of droplets with only one target encapsulated; this necessitates the use of dilute samples, and increases the number of droplets that contain nothing of interest. Current droplet technologies do not provide a means to discriminate and sort droplets of interest from those that contain irrelevant samples.

Here, we introduce a new method for identifying, protecting, and arraying droplets in a single microfluidic process. Using a photosensitive monomer as the continuous phase during emulsion formation, we recognize and analyze droplets with a simple computer algorithm, and employ continuous flow lithography [124] to polymerize ring-shaped particles around droplets of interest (Figure 4.5). These "armored droplets" can be arrayed in large, tightly packed matrices for analy-

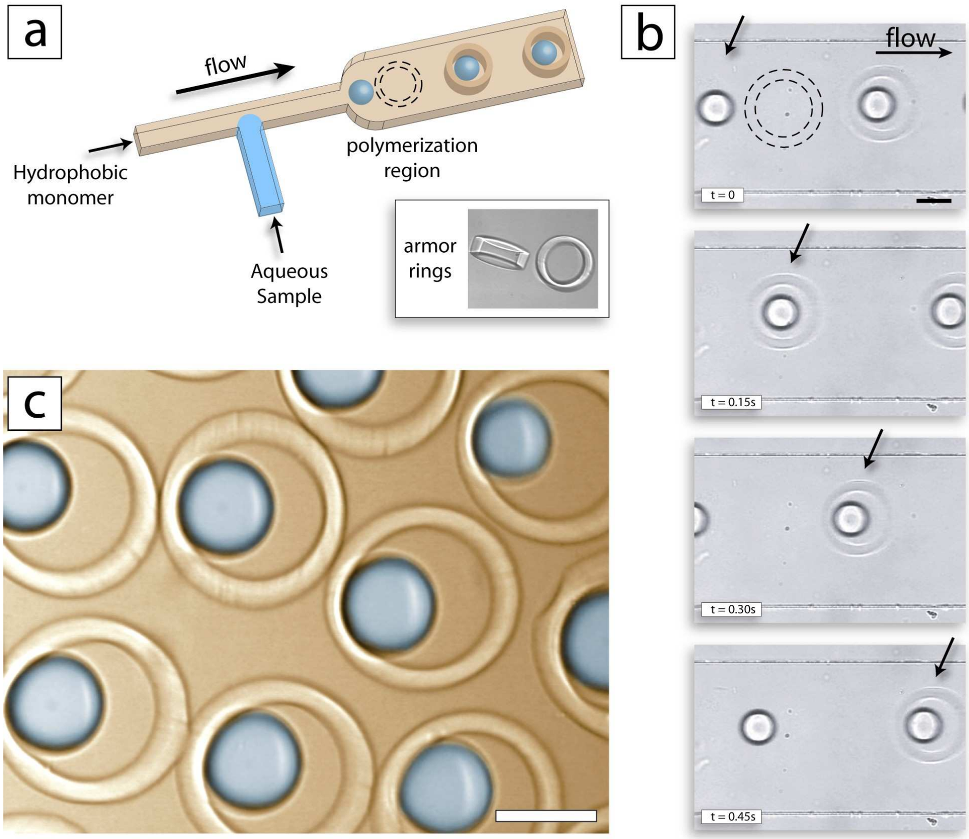

Fig. 4.5: *Synthesis of armored droplets. (a) Aqueous droplets were broken off in a 40 µm-tall, 40 µm-wide T-junction channel with an organic monomer used as the continuous phase. A computer script was used to monitor droplets as they entered the polymerization region, triggering the UV shutter to polymerize an armor ring around each. Shown with the schematic is an image of arrayed droplets collected at the end of the channel (bottom), artificially colored to designate monomer (tan) and droplets (blue). (b) Time sequence images showing polymerization around a droplet. Scalebars are 50 µm.*

sis while protected from coalescence without the use of surfactants. Moreover, the protective 2D shell formed around the particles does not fully encapsulate the droplets, enabling straightforward recovery of samples.

In our proof-of-principle experiments, we used TMP-TA with 5% Darocur 1173 as the organic monomer with pure water as the aqueous phase. After breakoff in a T-junction, rings were successfully polymerized around droplets with 30 ms UV doses at a rate of ∼2 droplets/second (Figure 4.5b). The armored droplets then flowed along the channel and were collected at a widening near the channel exit (Figure 4.5a, bottom). Similar experiments were performed to capture polymeric beads suspended in a PEG monomer stream (data not shown). These experiments demonstrate the feasibility of using flow lithography to actively capture, immobilize, or encapsulate entities contained in monomeric streams. This system may be used with a dynamic mask (such as a digital micromirror device) to give each armored shell a unique barcode; when used with cells, this could provide a means of high-throughput single cell analysis with subsequent sorting.

4.1.3 Limitations of CFL

The fundamental limitations of a projection photolithography technique, such as ours, are mainly governed by the optical resolution and the depth of field of the microscope objective used (see the Supplemental Information from Dendukuri *et al.* [124] for details). The resolution of an objective is the smallest distinguishable feature that can be discerned while the depth of field is the length over which the beam of light emanating from the objective can be considered to have a constant diameter. In our case, the resolution limits the size of the smallest particle that can be made while the depth of field restricts the length over which the sidewalls will be straight. Better resolution comes at the cost of decreased depth of field. Additionally, practical constraints on particle synthesis are imposed by finite polymerization times and the minimum feature size currently printable on a transparency mask ($\sim$10 μm).

The exposure time required to polymerize particles was inversely proportional to both the height of the channels used and the size of the transparency mask feature; particles required longer polymerization doses when either of these two parameters was decreased. The oxygen inhibition layer thickness is independent of channel height, leading to more pronounced effects in low-height channels, where the layer occupies a larger fraction of the channel height. Smaller transparency feature sizes require increased polymerization doses as a result of diffraction induced limitations in the internal microscope optics. Longer polymerization times lead to constraints on the maximum velocity of the oligomer stream, in order to avoid shape deformation of the particles.

4.2 Stop-Flow Lithography

Although flow is necessary to synthesize particle continuously, the movement of monomer during polymerization detracts from the feature resolution that can be achieved and also limits the throughput when high fidelity is required. To overcome this effect, we have developed a variation of CFL that operates with a stop-polymerize-flow scheme as shown in Figure 4.6. In this scheme, the monomer flow is stopped, particles are polymerized, and the flow is started again to flush the synthesized structures out of the polymerization region.

In this method, called Stop-Flow Lithography (SFL), air pressure is used to drive the flow (setup 2.2.3), providing a rapid response that is unattainable using syringe pumps. Fluid flow is stopped by releasing the pressure in the sample inlet chamber to the atmosphere (using a 3-way solenoid valve). The system has been automated and can be controlled using a single computer (Figure 4.6).

This method provides several benefits over CFL. Firstly, because particles are polymerized on a stagnant versus flowing monomer stream, SFL provides better feature resolution than CFL. Also, the flowrates used in SFL are typically very high, allowing a higher average flow velocity and hence better throughput than CFL. Lastly, the synthesis of multifunctional particles benefits from this increased flowrate, which provides sharper interfaces between functionalities. These attributes are discussed in more detail below.

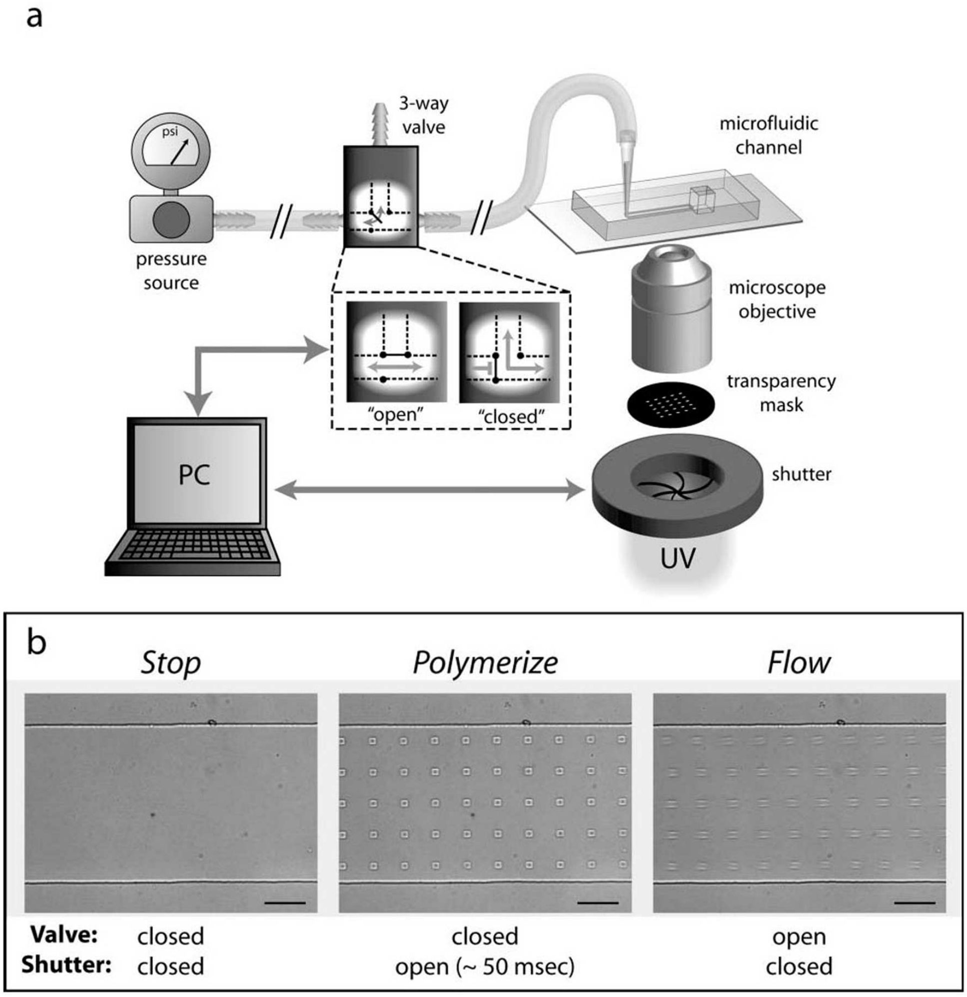
a
psi
pressure source
3-way valve
microfluidic channel
microscope objective
transparency mask
shutter
UV
PC
"open"
"closed"
b
Stop
Polymerize
Flow
Valve:
Shutter:
closed
closed
closed
open (~ 50 msec)
open
closed

Fig. 4.6: *Schematic of stop-flow lithography setup. Pressurized air is controlled using a 3-way solenoid valve to selectively drive monomer through a channel. A computer is used to control the valve and UV shutter synchronously to facilitate flow stoppage, polymerization of particles, and particle flushing with flow. Shown also is a brightfield image of the three-step process. Scalebars are 50 μm.*

4.2.1 Improvement of Resolution and Throughput over CFL

Maximum resolution of polymerized structures is achieved on a stagnant monomer film, where any effects of smearing over the exposure time (as seen with CFL) are nonexistent. After pressure release, a finite response time is required for the monomer flow to cease – this time is related to that required for the elastic PDMS channel to relax from a stressed state. According to theory [133], the response time required for flow stoppage (τ_r) is given by

$$\tau_r \sim \frac{\mu L^2 W}{E H^3}$$

where μ is the fluid viscosity, L, W, and H, are the channel length, width, and height, respectively, and E is the Young's modulus of the channel material. The theory was supported by experimentation over a broad range of channel geomteries, with response times varying from tens of milliseconds to tens of seconds [133].

The throughput of SFL is determined by the number of particles polymerized per cycle and the total cycle time ($t_{stop} + t_{polymerize} + t_{flow}$). The stop time is determined by τ_r, polymerizion time is determined by reaction kinetics (and is typically < 100 ms), and the flow time is determined by the length of channel over which particles were polymerized and the velocity used to flush them out. Using this calculation, it was shown that the attainable throughput of SFL is orders of magnitude greater that that using CFL, particularly at finer feature resolution [133].

4.2.2 Synthesis of Multi-functional Particles with Sharp Interfaces

One of the unique advantages of flow lithography in microfluidic devices is the ability to exploit laminar flow to polymerize across multiple distinct streams, forming particles with multiple adjacent chemistries. Such particles are finding use in several applications including multiplexed detection [149] and self assembly [139]. When using miscible fluids, the diffusion of species between the streams can deplete the sharpness of the interfaces between adjacent chemistries – an occurrence that is typically undesirable. We demonstrate how stop-flow lithography can be used to minimize diffusion across streams, improving the sharpness of the interfaces between particles chemistries.

We made tri-functional, striped rods to investigate the interfaces between fluorescent and non-fluorescent particle chemistries when using CFL and SFL (Figure 4.7). We used a channel with three inlets that were connected in parallel to the same pressure source: this eliminates lateral flow and maintains constant stream widths. As such, any "smearing" of the interfaces between the particle chemistries is expected to result only from diffusion of the fluorescent species between streams.

We made particles that were ~ 270 μm-long, and 30 μm-deep using an exposure time of 50 ms in a 40 μm-tall channel approximately 200 μm after the stream junction (Figure 4.7a). For particle synthesis using CFL, we chose a flow velocity of $\sim$50 μm/sec to limit the expected distortion of the width (during polymerization) to $\sim$10% (50 μm/sec × 0.05 sec = 2.5 μm) while for SFL, we used a much higher velocity of $\sim$1,000 $\mu m/sec$ with a t_{stop} of 50 ms. Because of the small exposure times used (50 ms), the diffusion of fluorescent species across the interface between the adjacent streams is expected to be small ($l = \sqrt{D t_{polymerize}} \sim 2$ μm).

After particles were synthesized and rinsed, we took scans of fluorescent intensity along the length of the particles (and entire width) at the fluorescent/non-fluorescent interfaces (Figure 4.7b). As can be seen, the particles made using SFL show a dramatically sharper interface than those using CFL because we were able to use a higher velocity. This difference would be even more dramatic if it was necessary to preserve smaller feature sizes, which would further decrease the velocity for CFL.

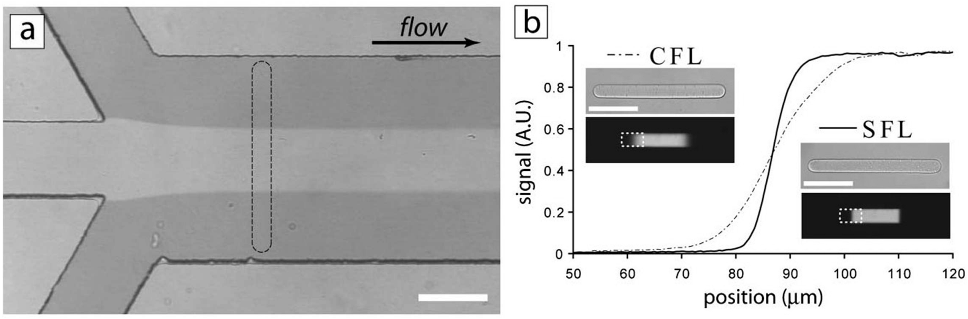

Fig. 4.7: *Interface comparison of multifunctional particles made using CFL and SFL. (a) Striped, rod-shaped particles were polymerized across adjacent streams, the center of which was loaded with a fluorescent monomer. (b) Scans of fluorescent intensity were taken along particles at a fluorescent/non-fluorescent interface. Insets show DIC and fluorescence images of particles made using CFL (with flow velocity of* ∼*50* μ*m/s) and SFL (with a velocity of* ∼*1,000* μ*m/s). Scalebars are 100* μ*m.*

4.2.3 Valve System for Independent Stream Control

The use of SFL to generate particles with multiple adjacent chemistries is extremely attractive but requires special attention in experimental design. When using SFL to polymerize particles across multiple adjacent streams, it is imperative that the flow of all streams cease simultaneously. This is most conveniently accomplished using a common pressure source split multiple ways to drive flow at each inlet. If the pressure at every inlet is equal, the relative width of each adjacently-flowing monomer stream will remain constant (as determined by the inlet branch geometries, monomer viscosities, etc). The ability to actively control the width of each monomer stream, regardless of channel geometry, is extremely desirable for the synthesis of multifunctional particles, as will be seen in later chapters of this thesis.

In order to make multifuncitonal particle synthesis more robust, we developed a simple system that allows independent control over multiple monomer streams as seen in Figure 4.8. Similar to the setup described previously (setup 2.2.3), a pressure source is connected to a 3-way solenoid valve that allows pressurization of the sample chambers or venting from the sample chambers to the atmosphere. The pressure is split into as many separate chambers as there are inlets for the device. Each sample pressure chamber has a manual 2-way relief valve (Whitey), which purges air to the atmosphere, causing a pressure drop over a resistive element (filter pipette tip) leading into the chamber. The system is connected simply using tygon tubing and plastic 3-way connectors (VWR).

This simple plug-and-play flow control systems allows inexpensive, precise, real-time control over multi-stream flow in a microfluidic device. As shown in Figure 4.8, streams can be adjusted down to ∼5 μm (bottom, right) without noticeable flow fluctuations. This system works well with SFL, and has been used to generate particles with up to seven tightly controlled functional regions, as shown in Chapter 6.

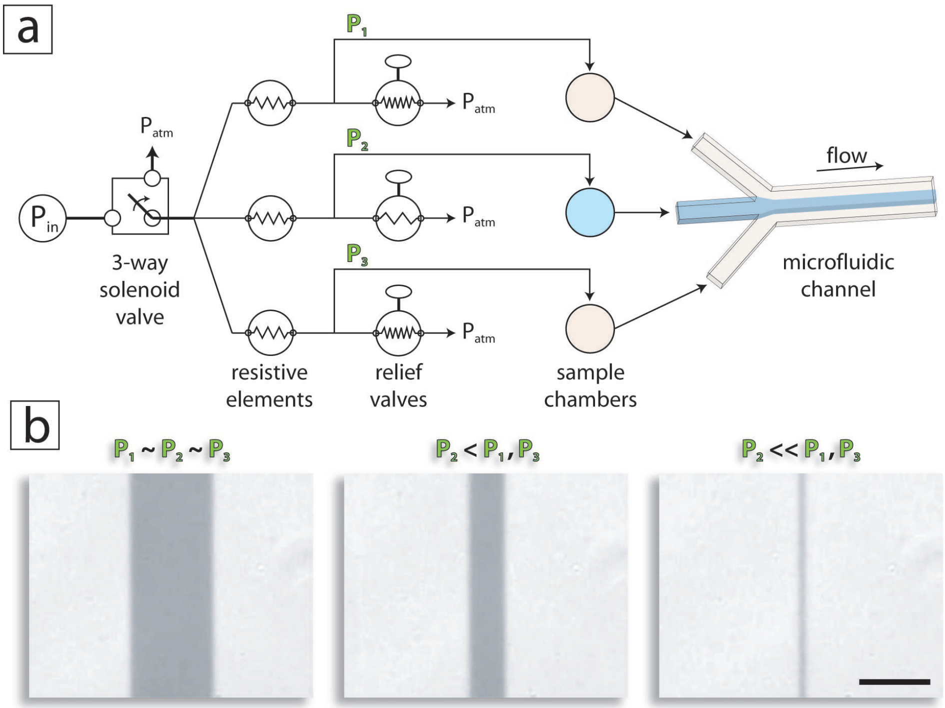
a
P1
P2
P3
Patm
Pin
3-way solenoid valve
resistive elements
relief valves
sample chambers
flow
microfluidic channel
b
P1 ~ P2 ~ P3
P2 < P1, P3
P2 << P1, P3

Fig. 4.8: *Valve system for independent flow control. (a) Schematic of flow-control system, consisting of a pressure source, 3-way solenoid valve, and independent sample chambers with pressure-control relief valves. (b) Bright-field images of stream adjustment (flow from top to bottom), showing reduction of central stream width upon opening of its respective relief valve. Scalebar is 50 μm.*

4.3 Conclusions

We have demonstrated a photolithography-based microfluidic technique that can be used to continuously synthesize polymeric particles that are morphologically-complex and may bear multiple chemistries. The system is high-throughput, is applicable to a broad range of materials, can be used to continuously capture and array entities contained in a monomer stream, and can be implemented using a standard fluorescence microscope. We have demonstrated increased resolution, throughput, and sharpness of interfaces using a stop-polymerize-flow scheme, and have developed an inexpensive system for independent stream control when making multifunctional particles.

CHAPTER 5

Encoded Hydrogel Particles

Flow lithography provides a means to generate microparticles that can have complex morphologies and multiple functional regions. In addition, particles composed of hydrogel may be co-polymerized with a functional biomolecule probe, allowing direct, one-step synthesis of bio-active particles. In this chapter, we will discuss how these attributes can be exploited to make particles that are well-suited for high-throughput biomolecule detection.

High-throughput screening for genetic analysis, combinatorial chemistry, and clinical diagnostics benefits from the use of multiplexing – an avenue that allows for the simultaneous assay of several analytes, but necessitates an encoding scheme for molecular identification. Current approaches for multiplexed analysis involve complicated or expensive processes for encoding, functionalizing, or decoding active substrates (particles or surfaces), and often yield a very limited number of analyte-specific codes.

We present a method based on continuous-flow lithography that combines particle synthesis, encoding, and probe incorporation into a single process to generate multi-functional particles bearing over a million unique codes. Using such particles, we demonstrate a multiplexed, single-fluorescence detection of DNA oligomers with encoded particle libraries that can be scanned rapidly in a flow-through microfluidic channel. Furthermore, we demonstrate with high specificity the same multiplexed detection using single, multi-probe particles. Much of the material covered in this chapter was reproduced from Pregibon, Toner, Doyle, *Science*, 2007 [149]. The sequences of nucleic acids mentioned in this chapter are listed in Table 2.2.

5.1 Synthesis of Multifunctional Encoded Particles

By exploiting laminar flows characteristic of microfluidics, we demonstrate the ability to generate mutlifunctional particles with distinct regions for analyte encoding and target capture (Figure 5.1). Particles were synthesized using setups 2.2.1 and 2.2.3, and protocols 2.3.3 and 2.3.9. Unless otherwise noted, prepolymers were prepared using a monomer mixture containing 67% PEG-DA$_{700}$, 30.5% TE buffer, and 2.5% Darocur 1173 blended at 9:1 with DNA probe to obtain final probe concentration of 50 μM. In a typical experiment, we flow two monomer streams (one loaded with a fluorescent dye, and the other with an acrylate-modified probe) adjacently down a microfluidic channel and use a variation of continuous-flow lithography [124] to polymerize particles (with 30 ms bursts of ultraviolet (UV) light) across the streams. In this manner, particles with a fluorescent, graphically-encoded region and a probe-loaded region can be synthesized in a single step.

Each particle is an extruded 2-D shape (Figure 5.1b) whose morphology is determined by a photomask that is inserted into the field-stop position of the microscope, and whose chemistry is determined by the content of the co-flowing monomer streams. The crosslinked polymer particles then flow down the channel (without sticking due to oxygen inhibition near the channel surfaces [124]) where they are collected in a reservoir. The particles can be rinsed of excess monomer and then used for biological assays.

We use poly(ethylene glycol) (PEG) (well known as a bio-inert polymer) as the particle foundation to eliminate the need to “block” surfaces after probe conjugation and as a transparent material, to allow transmission of fluorescent signal from both particle faces. These properties should enhance the both specificity and sensitivity of analyte detection. We use a simple dot-coding scheme to generate particles that can bear over a million (2^{20}) codes (Figure 5.1c). Particles are designed to be “read” along five lanes down their length with alignment indicators that are used to identify the code position and “read direction” despite the particle orientation (Figure 5.1c). The flat, long shape of the particles helps align them for scanning in a flow-through device. The spatial separation of various chemistries on the particles allows decoding and target detection to be achieved using a single fluorophore.

To demonstrate the versatility of particle synthesis, we selectively labelled monomer streams with a fluorohpore and used a variety of channel designs to generate particles bearing a single probe region, multiple probe regions, and probe-region gradients (Figure 5.1e–g). Multi-probe particles (Fig. 5.1f), made using channels with several inlet streams, allow for a direct, single-particle comparison of several targets. Furthermore, probe gradients (Figure 5.1g), made by simply allowing diffusion of the probe across streams in a long channel, are useful for broadening the detection range of an analyte when using a fixed detection sensitivity (when the signal can saturate). If magnetic nanoparticles are incorporated in a gradient, it may be possible to produce a temperature variation along particles when stimulated in an oscillating magnetic field [150].

A key feature of our method is the direct incorporation of probes into the encoded particles. This is accomplished by simply adding acrylate-modified biomolecules into the monomer solution. After polymerization, the probes are covalently coupled to the polymer network. This process is applicable for both oligonucleotide and protein probes [151, 152, 153]. We demonstrate in this work that the short bursts of UV used to synthesize probe-conjugated particles are not detrimental to the functionality of incorporated oligonucleotides. Previously, we showed similar results with bead-bound antibodies that were incorporated into polymer structures made from nearly identical monomer constituents [121].

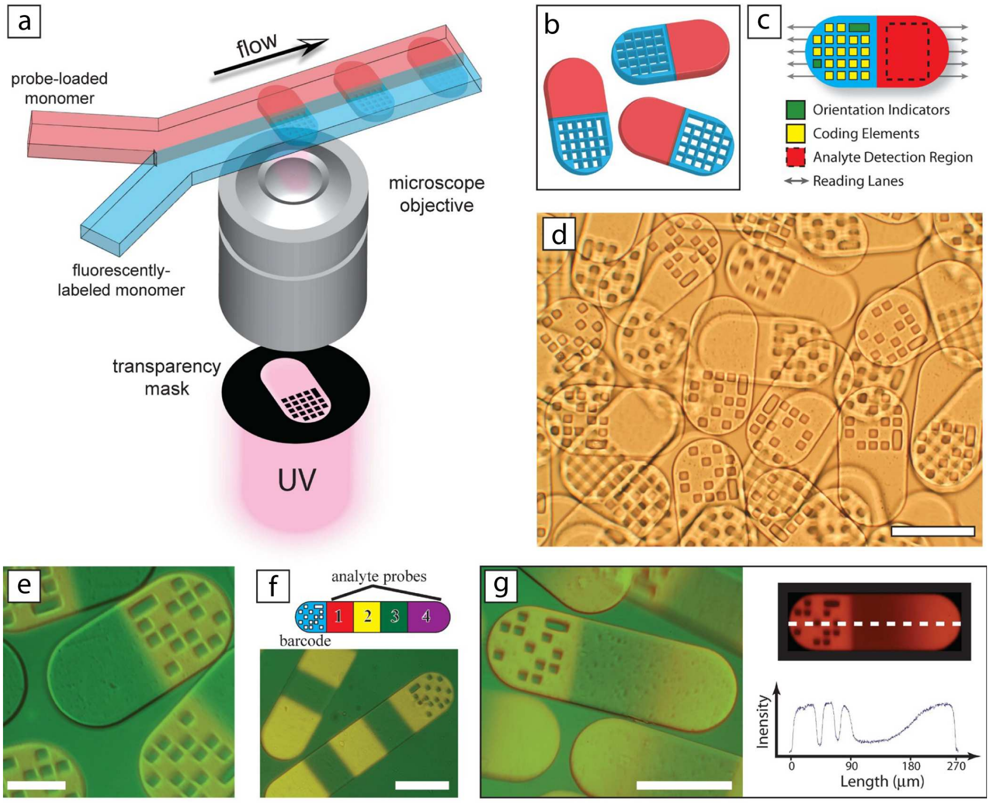
a
flow
probe-loaded monomer
fluorescently-labeled monomer
microscope objective
transparency mask
UV
b
c
Orientation Indicators
Coding Elements
Analyte Detection Region
Reading Lanes
d
e
f
analyte probes
1
2
3
4
barcode
g
Inensity
0
90
180
270
Length (μm)

Fig. 5.1: *(a) Schematic diagram of dot-coded particle synthesis showing polymerization across two adjacent laminar streams to make single-probe, half-fluorescent particles (shown in (b)). (c) Diagrammatic representation of particle features for encoding and analyte detection. Encoding scheme shown allows the generation of* 2^{20} *(1,048,576) unique codes. (d) Differential interference contrast (DIC) image of particles generated using the scheme shown in (a). (e – g) Overlap of fluorescence and DIC images of single-probe (e), multi-probe (f, bottom), and probe gradient (g, left) encoded particles. Shown also is a schematic representation of multi-probe particles (f, top) and a plot of fluorescent intensity along the centerline of a gradient particle (g, right). Scale bars are 100* μ*m (d, f, g) and 50* μ*m (e).*

5.2 Multiplexed DNA Detection

To demonstrate multiplexing capabilities, we used acrylate-modified oligonucleotide probes (which are commercially available) for DNA sequence detection (Figure 5.2a–c). We synthesized three batches of particles – one of which was loaded with 20bp oligonucleotide Probe #1 (P_1), another with Probe #2 (P_2), and a third with no probe to serve as a control. Targets were fluorescently-labelled oligonucleotides with complementary sequences to the two probes. We mixed the particles and incubated them for 10 min at room temperature in microwells containing either Target #1 ($\mathrm{T}_{1,D,Cy3}$, at 1 μM), Target #2 ($\mathrm{T}_{2,D,Cy3}$, at 1 μM), both targets (both at 0.5 μM), or no target. A positive target detection was indicated by probe-region fluorescence, which was more pronounced near the particle edges. This indicated that targets were able to diffuse and hybridize several microns into the particle body (see section 5.5.2). In each instance, the particles showed uniformity with high specificity to the oligomers, exhibiting fluorescence only when the target was present (Figure 5.2c).

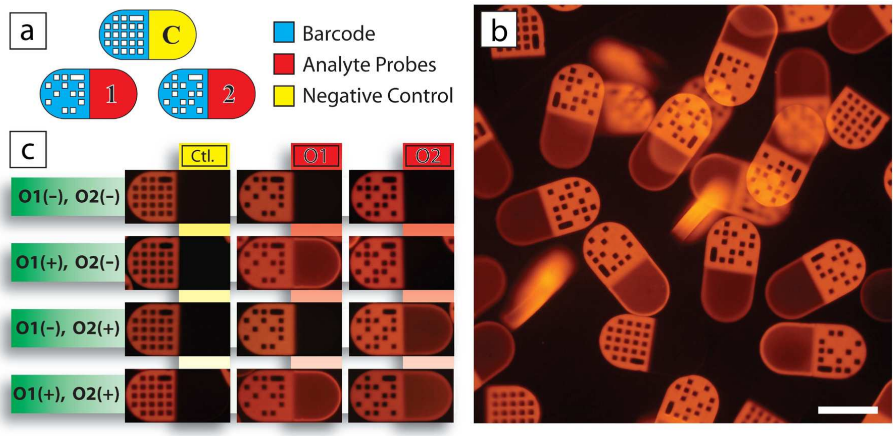

Fig. 5.2: *Multiplexed analysis using single-probe encoded particles. The particles were loaded with DNA oligomer probes (Probe #1, Probe #2, or no probe (negative control, C) as shown schematically in (a). (b) Shown are representative fluorescence images of particles after a 10min incubation with both fluorescent-labelled targets. Fluorescence in the probe-regions indicates target detection. Also shown are individual particles after incubation in solutions containing no targets, Target #1 only, Target #2 only, and both targets (c). Scalebar is 100 μm.*

To further demonstrate the power of our multiplexing scheme, we performed the same sequence detection assay using particles with multiple adjacent functionalities (Figure 5.3a–c). In this manner, we were able to simultaneously assay for the two target sequences (with a negative control) on a single particle. Again, the assay was highly specific (Figure 5.3c) and very uniform from particle to particle (Figure 5.3a). The interfaces between probes on the particles are very sharp and thinner stripes could be used for even greater multiplexing capabilities.

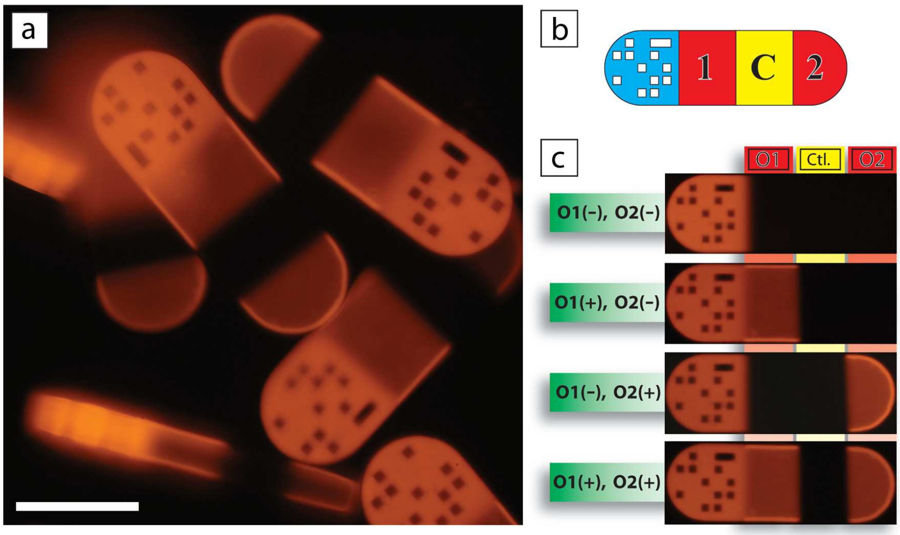

Fig. 5.3: *Multiplexed analysis using multi-probe particles. (a, c) Fluorescence images of particles with regions containing Probe #1, #2, and no probe (as shown in b) after a 10min incubation with targets #1, #2, or no target. Scalebar is 100 μm.*

5.3 Flow-through Particles Scanning

In order to prove that this method of multiplexed analysis is practical for high-throughput applications, we developed a simple scheme to scan particles in a flow-through device (Figure 5.4). Multi-probe particles used in the hybridization experiment previously described (Figure 5.3a–c) were flown through a microfluidic channel and observed on an inverted fluorescence microscope. Particles were aligned using flow-focusing and travelled down a channel only slightly larger than the particle width (Figure 5.4a). We used a bio-friendly surfactant (Tween-20) to ensure that the particles flowed smoothly down the channels without sticking. Images were taken at a designated detection region in the channel with an exposure of 1/125 sec as the particles passed the field of view (using a 20× objective). Image sequences were later analyzed to determine the particle code and quantify targets.

Shown in Figure 5.4b is a representative particle image with corresponding intensity plots along the five particle "reading lanes". The code along each lane can be determined by analyzing the sharp dips and plateaus in the intensity plots. Using the control-region fluorescence, we defined a positive target detection as the control average intensity plus 3 standard deviations for each particle. We were able to accurately identify the presence of both oligonucleotide targets after only a short 10 minute incubation.

The throughput of our system is primarily determined by the detection scheme and also particle size. The particles synthesized for this study are relatively large compared to those in other flow-through methods, measuring 90 μm in width, ∼30 μm in thickness, and 180 to 270 μm in length. Large size not only limits the throughput of a system, but also increases the sample volume.

However, the great particle-to-particle reproducibility we have demonstrated (see section 5.5.1) will afford a much lower redundancy than is typical in flow-through systems, improving efficiency. Using conservative estimates, we found that our system should be capable of providing rapid, high-density analysis with a manageable sample volume (see section 5.5.3) despite the seemingly large particle size.

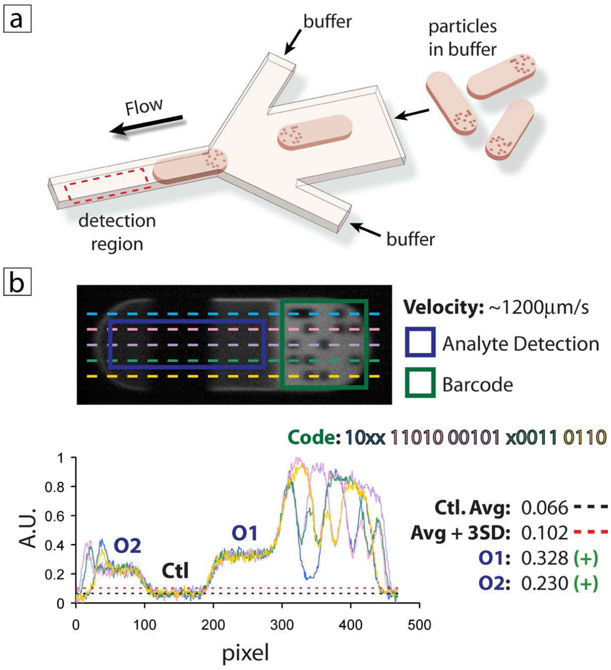
a
buffer
particles
in buffer
Flow
detection
region
buffer
b
Velocity: ~1200µm/s
Analyte Detection
Barcode
Code: 10xx 11010 00101 x0011 0110
A.U.
1
0.8
0.6
0.4
0.2
0
O2
Ctl
O1
0
100
200
300
400
500
pixel
Ctl. Avg: 0.066
Avg + 3SD: 0.102
O1: 0.328 (+)
O2: 0.230 (+)

Fig. 5.4: *Flow-through particle reading. (a) Schematic representation of a flow-focusing microfluidic device used to align and read particles after hybridization experiments. Particles are directed down a narrow channel and are imaged using fluorescence microscopy. (b) A typical image of a particle taken in a flow-through device as shown in (a). The image was captured using a microscope-mounted camera with an exposure of 1/125 sec as the particle flowed at a velocity of ∼1200 µm/s through the channel. Scans of fluorescent intensity were taken across the 5 "lanes" of the particle to reveal the code and detect oligomer targets (O1 and O2). With the particle in this orientation, the code is read from right to left, top to bottom where 1, 0, and x represent a hole, no hole, and an alignment marker, respectively. Particle shown is 90 µm × 270 µm.*

5.4 Preliminary Investigation of Particle Composition

5.4.1 Probe Concentration

We used serial dilution of an oligomer probe in precursor to determine the effect of concentration on signal detection. We synthesized particles with precursor probe concentrations of 150, 75, 37.5, and 18.75 μM. Control particles (no probe) were used to determine the background intensity (I_b). The particles were incubated for 30 min with a fluorescent-labelled target at 1 μM, rinsed, and imaged to determine fluorescent intensity (I_p). The fluorescent signal is reported in arbitrary units (AUs) taken as the difference $I_p - I_b$. The results are shown in Figure 5.5. The error bars on the graph represent the standard deviation in each measurement, with an average coefficient of variation (COV) of 9%.

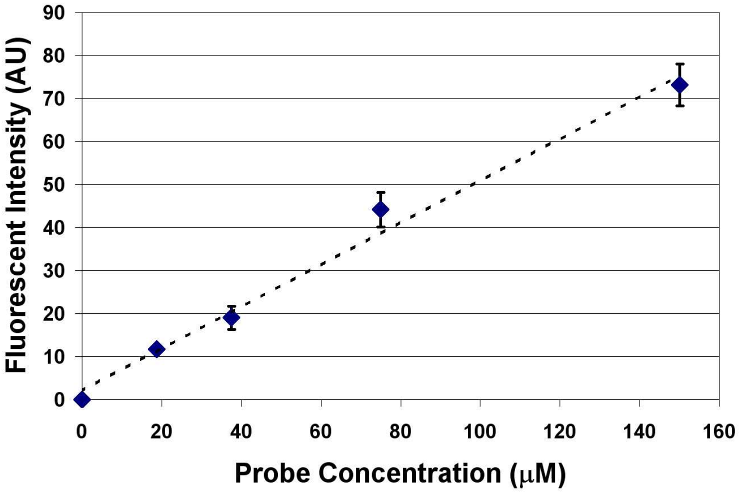

Fig. 5.5: *Fluorescent intensity of particles with varying precursor probe concentrations.*

As can be seen, the intensity increases linearly with probe concentration. This finding is expected when considering the binding of two complementary oligomers – at equilibrium, the relationship is given as:

$$T + P \rightleftharpoons TP$$

where T = target, P = probe, and TP = double stranded complex. At equilibrium, the concentrations of the species can be characterized by a dissociation constant, K_d, such that:

$$K_d = \frac{[P][T]}{[TP]}$$

If target is in great excess, as is the case in our experiment, then $[T] \approx [T]_o$. Using this, and the relationship $[P] = [P]_o - [TP]$, we obtain:

$$[TP] = \frac{[P]_o[T]_o}{K_d + [T]_o}$$

Thus, for a given initial concentration of target, we can expect the signal (which is proportional to [TP]) to be linear with respect to the probe concentration. Although we could obtain a much higher signal with increased probe concentration, we chose to use a precursor probe concentration of 50 μM probe for proof of principle experiments – this concentration gave sufficient signal for target detection with minimal usage of oligomer.

5.4.2 Choice of Monomers

We investigated the use of several polymers for barcoded particles, including poly(ethylene glycol) diacrylate of three chain lengths ($M_n = 200$, 400, 700) and also a blend of acrylamide with PEG-DA as crosslinker. The characteristics investigated when selecting a polymer blend were (1) fast polymerization kinetics, (2) low background fluorescence before hybridization, and (3) a strong fluorescence signal after hybridization. All solutions we made consisted of monomer (pure or at 2:1 with TE buffer), 2.5% photoinitiator, and DNA oligomer at 50 μM. Particles were made using 30 ms UV exposure with a 20× objective.

We found that hybridization signals were significantly higher when TE buffer was included in the monomer blend. This is consistent with our previous work [121], in which we discovered that bead-bound proteins incorporated in polymerized PEG hydrogels lost functionality in the absence of buffer. We found that PEG-DA$_{700}$ had significantly faster reaction kinetics than the other monomers and also showed significantly less background signal. The monomer solution we chose for initial hybridization experiments was a 2:1 blend of PEG-DA:TE with 1 – 2.5% photoinitiator.

5.5 Characterization of Particles

5.5.1 Polydispersity

It is very important that the particles being used for quantitative biomolecule analysis be consistent both morphologically and functionally. We have already shown that particles synthesized using continuous-flow lithography have a very low coefficient of variation ($< 2\%$) with respect to physical size [124]. We also performed experiments to investigate the variation of fluorescent signal for particles used in a hybridization study.

The fluorescent intensity of particles used in a hybridization study gives evidence of the "functional" polydispersity of the particles. However, this measure is not only dependent on the particles, but also on the hybridization experiment itself – the numbers we present should be a conservative estimate. We found the COV of fluorescent signal to range from 6 – 10% when incubating with target at concentrations of 1 μM – 10 nM and increase to ∼15 – 30% for lower concentrations (down to 10 pM).

5.5.2 Active Probe Concentration

In order to estimate the effective "density" of probe accessible to targets during our short incubations, we used the concentration of probe incorporated into our monomer solution (50 μM) with an estimate of the depth to which oligomers can diffuse into particles and react. Shown in Figure 5.6 is a typical particle used in a hybridization study with a scan of fluorescent intensity across its sensing region.

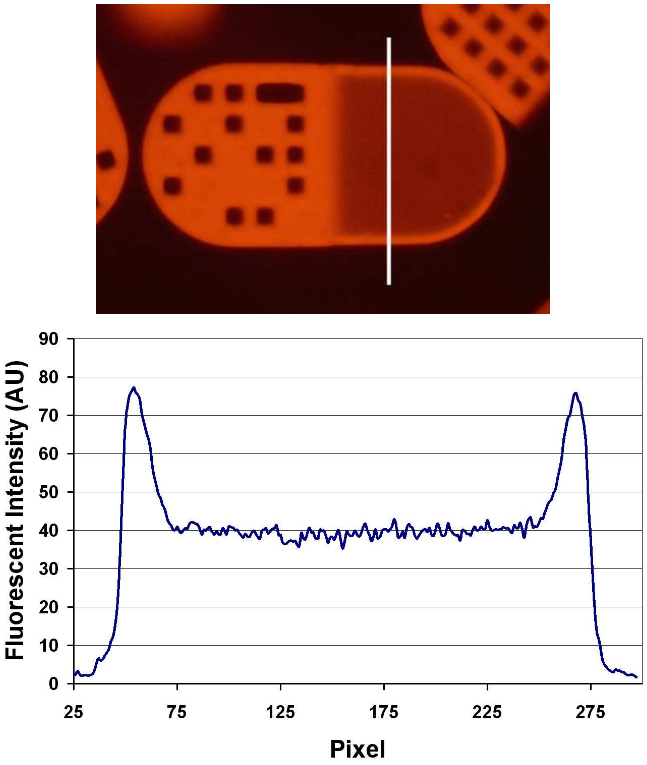

Fig. 5.6: *Plot of fluorescent intensity across a particle section after target hybridization. The white line on the particle image indicates the region that was scanned.*

As can be seen, the particle shows a significantly higher signal at the edges of its sensing region – the coded region does not show this characteristic because the fluorescent dye incorporated has been homogeneously distributed throughout. We assumed that this "edge" signal was proportional to the amount of oligomer bound to the 30 μm-thick edge of the particle. The intensity in the interior of the particle was almost exactly $\frac{1}{2}$ that of the edge for the several particles we investigated. Assuming that all surfaces are similar, we deduced that the active binding thickness in the interior of the particle must be 30 $\mu m \times \frac{80AU}{40AU}$ = 15 μm, or ~7.5 μm per face. As validation, we can see that the width of the high-intensity region at each particle edge is $\sim$ 20 pixels = 8 μm. Physically, this can likely be explained by kinetics (as described in Chapter 7). Based on the work of others, the PEG polymer we used should have a pore size of $\sim$ 10 Å when completely crosslinked [154, 155], which is larger than the expected radius of gyration for a 20bp target. This imposes a diffusion limitation on target penetration, which in turn limits hybridization kinetics.

Using the probe concentration of 50 μM (in monomer), with an active thickness of 7.5 μm per face and a 50% incorporation efficiency, we estimated the effective surface concentration to be:

$$\frac{50\mu M}{7.5\mu m} \times 50\% \simeq 1 \times 10^5 \frac{molecules}{\mu m^2}\ per\ face$$

Because the particles are transparent, the fluorescence of both faces should give a projected probe concentration of $2 \times 10^5 \frac{molecules}{\mu m^2}$. This is a similar "surface" concentration to those reported by others [156]. As mentioned previously, we can incorporate a substantially greater amount of probe into our particles to make the surface concentration much higher, thus increasing the rate of target hybridization.

5.5.3 Estimation of Throughput

Recently, microfluidic-based flow cytometers have been developed with integrated photomultiplier tubes to achieve a very high throughput. The fluid velocities in these systems can be on the order of 10 m/s (similar to conventional flow cytometers) while detection is carried out at a high sample rate of 5MHz, allowing a particle read rate of 17,000/sec [157]. We use this as a basis to estimate the throughput we can achieve with our system when incorporating more sophisticated sensing schemes. Conservatively, we estimated a flow velocity of 1 m/s and a spacing of 10 particle lengths between particles (each 200 μm in length). Thus, we can calculate a throughput of

$$THROUGHPUT = 1\frac{meter}{sec} \times \frac{1}{2,200}\frac{particle}{\mu m} \approx \mathbf{450}\frac{\textbf{particles}}{\textbf{sec}}.$$

Although this "particle/sec" throughput seems lower than that typically seen in flow cytometry, we discuss why on a "target/sec" basis, the technology should provide a sufficient throughput for high-density analysis.

We have shown that our system exhibits excellent particle-to-particle reproducibility (as discussed previously). Enzyme-linked immunosorbant assays (ELISAs), which are considered to be the gold standard in sensing, show similar precision [158] to our technology and are typically done only in duplicate. This level of redundancy is significantly lower than seen in flow cytometry-based assays. We will assume for estimation purposes that our assays can be performed in triplicate to yield accurate information. With a redundancy of 3, our "target/sec" throughput becomes

$$THROUGHPUT = 450\frac{particles}{sec} \times \frac{1}{3}\frac{target}{particles} \approx \mathbf{150}\frac{\textbf{targets}}{\textbf{sec}}.$$

Two simple modifications that will provide an even higher throughput are (1) reduction of particle size, and (2) incorporation of several probes on a single particle. We have demonstrated in our lab the ability to produce particles with features on the order of ~1 μm, so it is well within reason to consider the production of encoded particles that are half-sized in each dimension. This would increase the number of particles/volume by a factor of 8. Furthermore, if the particles have 3 functionalities (two probes and a control as in Figure 5.3), this increases the throughput by another factor of 2. Using these arguments, we can calculate some expected throughputs:

From this simple analysis, it seems reasonable to analyze one million targets in less than one hour when using reduced-size and/or multi-probe particles. This analysis also highlights the importance of particle size in terms of volume – reduced-size particles will likely be necessary for high-density analysis.

Particle Size	**Probes/Particle**	**Throughput** ($\frac{targets}{sec}$)	**Particle Volume** ($\frac{\mu L}{10^6 targets}$)
Normal	1	**150**	**1,800**
Half	1	**300**	**225**
Normal	2	**300**	**900**
Half	2	**600**	**113**

Table 5.1: *Estimation of throughput and particle volume for tests done in triplicate (each probe appears on three particles). "Normal" particle size is* $\sim 100 \times 200 \times 30$ μm*, while "half" size is* $\sim 50 \times 100 \times 15$ μm*. Particle volume is based on* 10^6 *targets tested, which for single and two-probe particles corresponds to* 3×10^6 *and* 1.67×10^6 *total particles, respectively.*

5.5.4 Initial Study of Detection Limits and Dynamic Range

We hybridized particles with fluorescent target at concentrations spanning over several orders of magnitude in order to determine a suitable range of detection. Samples of particles from a common batch (with 50 μM precursor probe concentration) were incubated with 50 μl of target solution for 30 min at room temperature on a vortex mixer – target concentrations ranged from 10 nM – 10 pM corresponding to 500 fmol – 500 amol (500×10^{-18} moles) of oligomer. After hybridization, the particles were rinsed and imaged under fluorescence for detection with an EB-CCD camera (C7190-20, Hamamatsu) mounted to our microscope. Because the system had an 8-bit limited dynamic range, it was necessary to use three different sensitivity settings to accommodate the broad range in fluorescent signal. As such, two of the particle batches were imaged at two of the three sensitivity settings so the signals could be normalized and plotted on a common scale. The results of the detection study are shown in Figure 5.7.

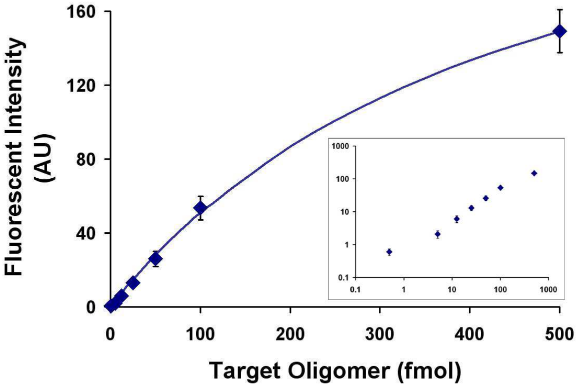

Fig. 5.7: *Hybridization signal (fluorescent intensity) of particles incubated at varying target concentrations.*

We found the assay to be quite sensitive, detecting oligomer comfortably at the lowest amount tested (500 amole). This finding suggests that our system has a comparable sensitivity to the current state of the art multiplexing systems including Affymetrix [159] and Luminex [160]. In addition, the graph shows a broad linear region, which represents the wide dynamic range of our high-capacity particles. Beyond these initial studies, we will show in Chapter 7 that the sensitivity can be dramatically improved by optimizing particle design and detection scheme.

5.5.5 Cost of Materials

At standard non-bulk pricing, the raw material cost to produce 1 million single-probe particles similar to those presented in the chapter is only \$ 4.28 (\$ 0.14 without DNA probe) as outlined in Table 5.2.

Component	**Unit Price**	**Price per 10^6 Particles**
PEG Monomer	\$ 50/500ml	\$ 0.06
Photoinitiator	\$ 80/250ml	<\$ 0.01
Fluorescent Dye	\$ 560/1g	\$ 0.08
20bp DNA Probe	\$276/1μmole	\$ 4.14
		Total: \$ 4.28

Table 5.2: *Estimation of raw material cost to produce* 10^6 *particles* ($\sim 100 \times 200 \times 30$ μm) *with DNA oligomer probe incorporated at a concentration of* 50 μM.

As described earlier, it would be reasonable to make particles half-sized in each dimension, which would reduce particle volume and cost by a factor of 8 (to only \$ 0.54 per 10^6 particles). It is also important to note that very little sample is wasted due to the low-volume microfluidic processing.

The microchannels used for particle synthesis and flow-through reading are of simple design and can be generated very economically. A single 4” wafer (< \$ 100), generated using standard SU-8 lithography, can easily bear over 10 channels and be molded from many times (we assume 10 times for subsequent calculations). In addition, each device may be used several times (we will use 5). Therefore, using very conservative estimates, the device cost would be as shown in Table 5.3.

Component	**Unit Price**	**Price per Device**
Fabrication of Master	\$ 100/100 channels	\$ 1.00
PDMS	\$ 0.10/g	\$ 0.25
Microscope Slide	\$ 100/400	\$ 0.25
		Total: \$ 1.50
		Price per use: \$ 0.30

Table 5.3: *Estimated cost of microdevices used for particle synthesis and flow-through reading. It was assumed that master wafers have 10 channels and can be molded 10 times, and that each device could be used 5 times before being discarded.*

The material cost for a single multiplex experiment with a million particles would be < \$ 5.00 (\$ 4.28 for the particles and \$ 0.60 for one “synthesis” and one “read” channel). This estimate does not include the buffer used in particle reading, which consists of inexpensive materials and would be negligible in the overall cost.

5.6 Conclusions

We have demonstrated the use of encoded hydrogel particles for multiplexed detection of nucleic acids. Importantly, our approach is particle-based, affording both high-throughput and versatility, and also utilizes hydrogel substrates, affording favorable solution-like thermodynamics. In addition to being very reproducible, our approach is very sensitive and specific, as will be discussed more in Chapter 7. Compared to commercially-available technologies, our system offers all-in-one particle synthesis, incorporation of multiple probes, low cost, virtually unlimited codes, and can be implemented using little more than a standard fluorescence microscope.

CHAPTER 6

Assay Optimization and Validation for mRNA Profiling

In the previous chapter, we demonstrated a new approach to multiplexed nucleic acid detection using encoded, multifunctional hydrogel particles. Although proof-of-principle experiments were done, it was necessary to further explore particle and assay design, and also to demonstrate that the system could be used practically for real-world applications. To this end, in this chapter we introduce a simplified encoding scheme, study a range of particle compositions, introduce two detection schemes, and demonstrate profiling of messenger RNA (mRNA) in a drug discovery setting.

6.1 1–D Encoding for Medium-Density Applications

Although we introduced a 20-bit encoding scheme that allows for over a million unique codes, it is unclear whether this level of multiplexing is practically feasible (given our current setup) or even desirable in most circumstances. There are many applications including neonatal screening, *in vitro* cancer diagnostics, and drug discovery that require only a modest number of targets on the order of $\sim$100 – 3,000. This level of "medium-density" multiplexing cannot be achieved efficiently using current technologies. In addition to providing an excessive number of codes, our 20-bit scheme requires two dimensional (2–D) decoding, which adds complexity to the design of a scanning system.

For these reasons, we designed a more modest one-dimensional (1–D) encoding scheme that can accommodate multiplexing of up to 2,500 targets.

Our 1–D code is designed such that particles are scanned across their entire width – thus, only a single signal is required for decoding and target quantification (versus 5 signals as shown in Figure 5.1). In contrast to the 20-bit "digital code", the 1–D code utilizes "analog" levels in fluorescence, which are achieved by using 0–4 holes across the particle width at each coding location (Figure 6.1a). For a given number, the holes are distributed symmetrically across the long axis of the particle (ex. Figure 6.1b, top). The scheme incorporates an orientation indicator (last digit always 4, first digit always < 4), which also acts as a code calibration (the fluorescent signal is proportional to the number of holes at a given cross-section). As shown, the scheme provides $4 \times 5 \times 5 \times 5 \times 5 \times 1 = 2,500$ unique codes, but can be adjusted by adding or deleting columns to accommodate a given application. Particles are designed to be $\sim 225 \times 90 \times 30$ μm in size.

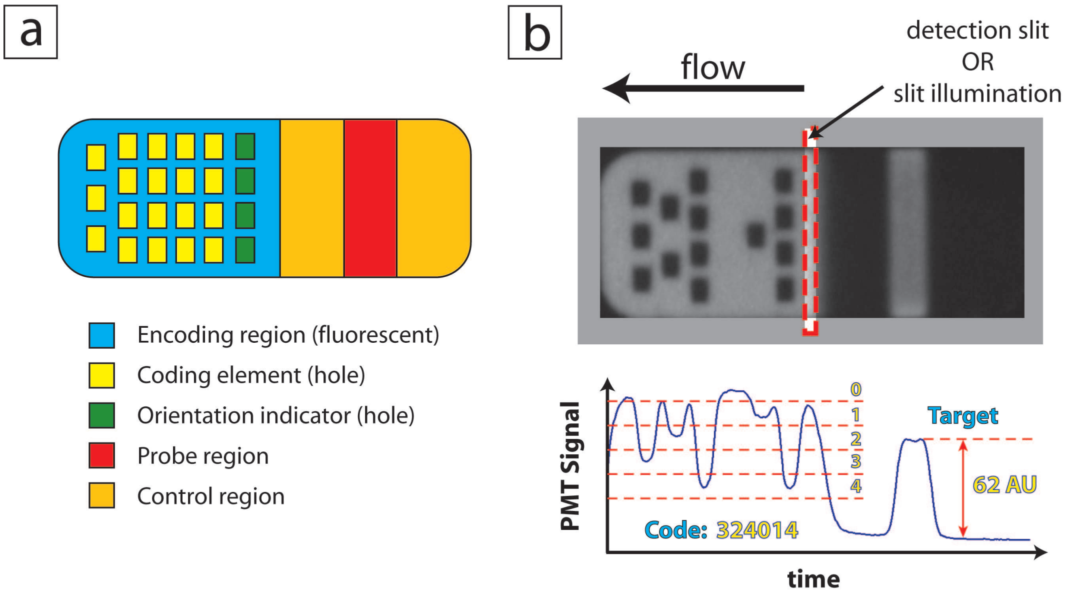

Fig. 6.1: *1–D encoding scheme. (a) Schematic of particle design with symmetric, analog dot-coding scheme (providing 2,500 codes) and probe region flanked by two control regions. (b) Sample fluorescence image and scanning. Particles are designed to be flowed along a channel and analyzed using slit illumination/detection that is perpendicular to the channel. Scans can then be analyzed to reveal the code (using trough depths) and target amount.*

As shown in Figure 6.1b, particles are designed to be read with slit illumination and/or slit detection that is perpendicular to the direction of flow. During flow-through scanning, light can be continuously collected with a single detector (such as a photomultiplier tube, PMT) to give a temporal signal as shown in Figure 6.1b. Using this signal, the code is determined by measuring the depth of each trough with respect to the calibration trough (which has a value of 4). The target is determined by measuring the fluorescent signal of the probe region, which is flanked by control regions on each side to eliminate residual fluorescence of the encoding region or subsequent particles. This 1–D code provides a dramatic simplification in decoding while maintaining sufficient encoding for medium-density applications.

6.2 Investigation of Particle Composition

By altering the composition of prepolymer solutions, we can tune the properties of hydrogel particles made using flow lithography. As the diffusivity of targets through a gel is related to the porosity of the gel, the ability to finely tune pore size would allow adjustment of hybridization rates and also permit selective filtering of targets based on size. However, it is also expected that larger pore sizes will lead to a decrease in probe incorporation efficiency as well as particle rigidity. In order to investigate the effects of prepolymer composition, we have used a semi-interpenetrating network (semi-IPN) consisting of both reactive PEG-DA and inert PEG (a porogen), mixed at different ratios.

Using SFL, we made penta-functional "ladder" particles as shown in Figure 6.2a, where each rung of the ladder had a unique composition (Setups 2.2.3 and 2.2.1). Each monomer solution contained a total of 60% PEG (PEG-DA$_{700}$ + PEG$_{200}$), with the amount of PEG-DA ranging from $15-35\%$ (Protocol 2.3.9). In each monomer solution, we used 5% Darocur 1173 and 35% of 3× TE. The monomer solutions were mixed at 9:1 with a 50bp DNA probe (P_{fluoro}), which was modified with a fluorescein group to assess incorporation efficiency, to obtain a precursor solution with a probe concentration of 5 μM.

Probe Incorporation Efficiency

Prior to incubation with a target, the particles were assessed for fluorescence to quantify probe incorporation (Figure 6.2b). To find absolute values, the fluorescence at each particle composition was normalized using the fluorescence obtained from particles made using 60% PEG-DA$_{700}$. At this high concentration of PEG-DA, it can be assumed that nearly all of the probe is incorporated within the particles, either by covalent linkage or physical entrapment (as fully-crosslinked PEG-DA$_{700}$ is known to have a pore size of ~ 1 nm [154, 155]).

The results of this analysis show that the amount of reactive species in precursor solutions affect probe incorporation in a linear fashion, with incorporations ranging from $\sim 5-25\%$ over the compositions studied. Although this is by no means a limitation of our system, it is possible that the incorporation efficiency may be increased by matching the reaction rates of the monomer and probe species, which in this experiment were acrylates and methacrylates, respectively. It is known that acrylates react faster than methacrylates, so it is possible that if methacrylated monomers or acrylated probes were used, the probe incorporation would be higher.

Target Hybridization Signal

We expected that changing the particle composition would alter the resulting pore size. To study this in the context of DNA hybridization, we performed assays using DNA targets with varying sizes of 20, 50, 100, and 200bp ($T_{20,D,bio} - T_{200,D,bio}$). Using the Kratky-Porod equation [161], we can estimate that oligonucleotides of these lengths have radii of gyration (r_g) on the order of 2, 4, 7, and 10 nm with the ionic strength used (0.1M). It is important to realize that the use of polymer

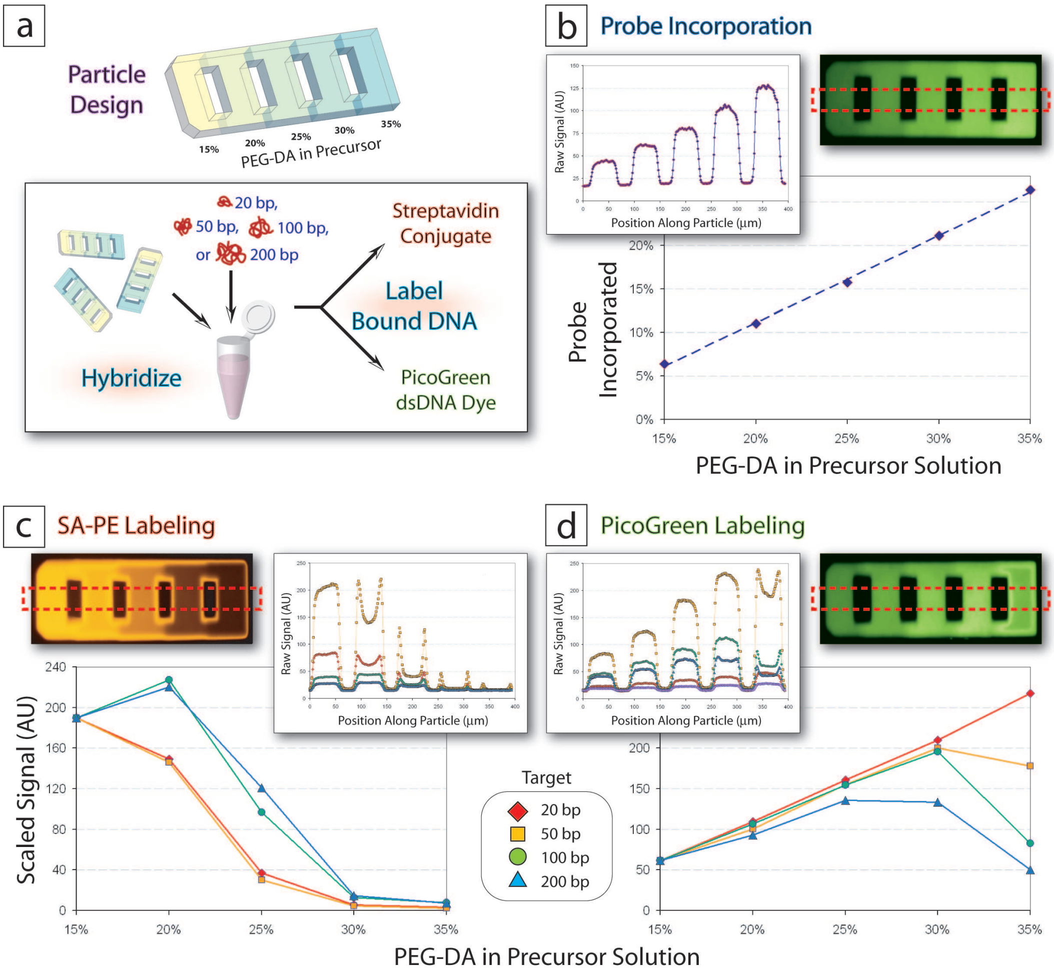

Fig. 6.2: *Particle composition study. (a) Penta-functional particles made from monomer solutions containing 15 - 35% PEG-DA were investigated for probe incorporation (b) and hybridization signal using two methods of fluorescent detection (c, d). Fluorescent scans along the particles (c, d, small plots) were scaled (large plots) to show penetration of streptavidin-PE (SAPE) reporter (c) and DNA targets (d) that varied from 20 – 200bp in size. Particles have dimensions of* $400 \times 100 \times 30$ *µm.*

targets (such as DNA) will not provide a direct measurement of the hydrogel pore size as these non-rigid polymer chains can traverse the gel via reptation.

Particles were hybridized with each target (at 1 µM) for 90 minutes and assessed for fluorescence using one of two methods (Figure 6.2c,d). It was not expected that the system would reach equilibrium with such a short hybridization time, in which case kinetic effects should be taken into concern. As shown in Figure 6.2, the absolute values of fluorescence depended greatly on target length. This discrepancy is likely a result of DNA secondary structure, which varies greatly across the targets used, and is known to alter the association rate of complex formation [162]. For this reason, signals were normalized using the signal intensity observed at 15% PEG-DA in order to emphasize trends with respect to particle composition.

One traditional method of labeling a target for fluorescent detection is biotinylation. After hybridization with biotinylated targets, a streptavidin-conjugated fluorescent reporter (SAPE) may be used for detection. However, this method is only suitable for particles that have a pore size larger than the relatively large streptavidin complex, which has a radius on the order of ~ 5 nm. After hybridization with biotinylated targets, particles were incubated with SAPE reporter for 30 minutes prior to analysis. As can be seen in Figure 6.2c, there appears to be a sharp transition in hybridization signal at 25% PEG-DA. This reveals the point at which the gel pore size is approximately that of the streptavidin reporter molecule, indicating that when using this fluorescent labelling method, a particle composition containing less that 25% PEG-DA must be used.

In order to get a better understanding of DNA hybridization regardless of pore size, we used a second labeling method that relies on a small molecule dsDNA dye (PicoGreen). The dye interacts with DNA and shows dramatic fluorescent enhancement when bound to DNA/DNA (or DNA/RNA) complexes. As this dye can easily penetrate the polymer network in comparison to the bulky SAPE reporter, this labeling scheme gave a much better view of DNA hybridization throughout the particles as shown in Figure 6.2d.

Using the PicoGreen labeling method, we see that the 20bp target penetrates into all sections of the particle, with fluorescent intensities that mimic those for probe incorporation (Figure 6.2b). All targets show this trend for for lower PEG-DA compositions, but deviate at 30% PEG-DA for the 50 and 100bp targets, and around 25% for the larger 200bp target. These results confirm that particle composition can be tuned to selectively inhibit hybridization of larger oligonucleotide targets.

In selecting an “optimized” monomer composition for general assay use, we chose the composition of 20% PEG-DA. This composition allows use of both fluorescent labeling schemes (as described in the next section) and ensures that particles are mechanically robust, as no deformation or breaking was observed for this composition. As shown in Figure 6.2b, particles made from this particle composition retain $\sim 11\%$ probe included in the precursor solution.

6.3 Schemes for Labeling Targets

For a fluorescence-based detection scheme, it is necessary to label targets with a fluorophore. For small RNA targets (∼20bp), this can actually be quite difficult. Approaches to labeling small targets include biotinylation [163, 164], Cy3/Cy5 labeling [165, 113, 166], and enzymatic approaches [167, 168]. These methods typically suffer from sequence bias, the requirements of small RNA purification and high input total RNA, high cost, and time-consuming protocols often requiring ∼ four [167] to 16 hours (overnight) [113, 166].

In order to show the versatility of our hydrogel particle-based method, we demonstrate the use of traditional biotin-SAPE labeling (as used in the Section 6.2) and introduce a rapid labeling scheme that is particularly attractive when quantifying small nucleic acid targets. The two schemes are shown schematically in Figure 6.3.

The traditional scheme requires biotinylation of a nucleic acid sample (which can be done using a commercially-available kit), hybridization with particles, and the subsequent attachment of a fluorescent reporter as shown in Figure 6.3b and described in Protocol 2.3.12. Protocols for biotinylation typically require 1 hour (or more) and labeling with reporter requires and additional

30 minutes. The method allows for detection with an efficient fluorophore (phycoerytherin) but methods of labeling nucleic acids prior to hybridization are often affected by sequence and secondary structure.

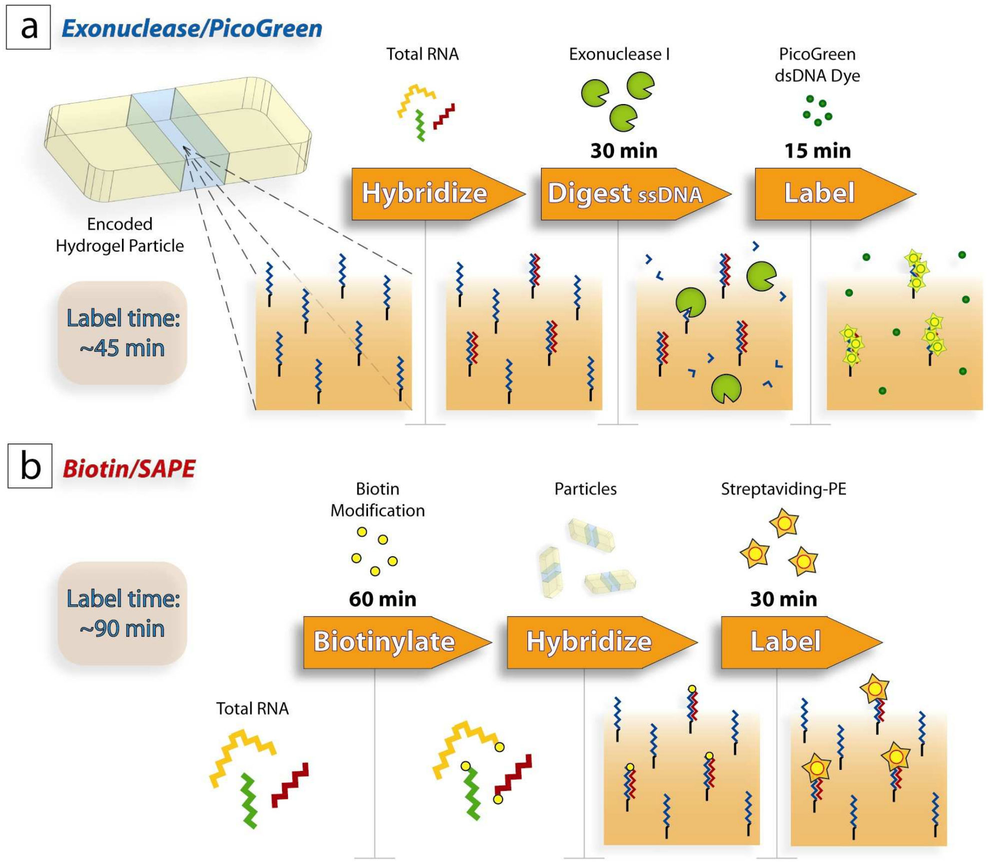
a
Exonuclease/PicoGreen
Total RNA
Exonuclease I
PicoGreen
dsDNA Dye
30 min
15 min
Hybridize
Digest ssDNA
Label
Encoded
Hydrogel Particle
Label time:
~45 min
b
Biotin/SAPE
Biotin
Modification
Particles
Streptaviding-PE
Label time:
~90 min
60 min
30 min
Biotinylate
Hybridize
Label
Total RNA

Fig. 6.3: *Schematic illustrations of the two assay protocols used for detection. (a) With the "Exonuclease/PicoGreen" scheme, targets are hybridized with particles, unbound probes are digested using exonuclease I, and target-probe complexes are directly labelled using a dsDNA dye (PicoGreen). (b) With the "Biotin/SAPE" scheme, targets are biotinylated, hybridized with particles, and then fluorescently labelled using a streptavidin-PE reporter.*

As an alternative to labeling targets, we developed a method to fluorescently label target-probe complexes after hybridization has occurred (Figure 6.3a). As such, this approach eliminates the sequence bias frequently observed in end-labeling schemes; these schemes are very sensitive to target secondary structure. Our method is rapid, easy to implement, and requires only a few readily-available reagents. In this scheme, particles are directly hybridized with a sample, incubated with Exonuclease I to digest unbound probe, and then complexes are labelled with PicoGreen dsDNA dye (as described in Protocol 2.3.13). Exonuclease I is known to selectively digest ssDNA with 3' – 5' directionality and does not digest RNA, DNA/DNA complexes, or DNA/RNA complexes.

PicoGreen is fluorescent nucleic acid stain typically used for quantifying dsDNA in solution. The stain shows flourescent enhancement upon biding with nucleic acids, which is dramatically higher for double-stranded species. Together, exonuclease digestion and PicoGreen staining provide a reliable, sensitive method for target quantification in hydrogel particles.

Although digestion of DNA probes using Exonuclease I has been applied to planar arrays [167], to our knowledge, this approach has not been used with gel systems. As such, it was necessary to optimize both incubation time and exonuclease concentration for our system. To asses the incubation time needed for probe digestion, we incubated particles (made using monomer with 20% PEG-DA) with a 22bp DNA probe (P_{7a}) incorporated at $\sim$5 μM (50 μM $\times$ 11% incorporation efficiency) for varying times with various levels of exonuclease. The results, shown in Figure 6.4a, suggest that regardless of the concentration used, the exonuclease seemingly digested the probe after only a few minutes of incubation. To be conservative and ensure proper digestion, we chose to use 30 minute incubations for future experiments.

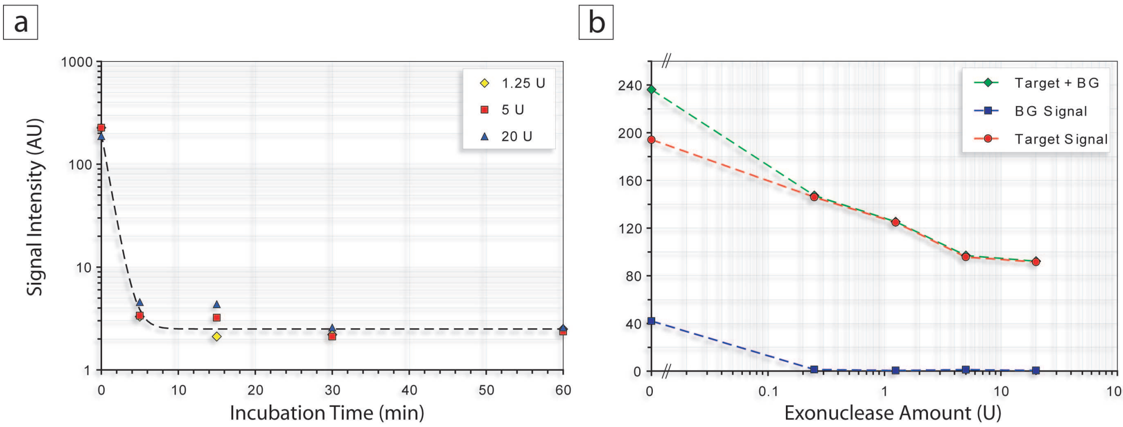

Fig. 6.4: *Determination of fluorescence background and target signal depletion during exonuclease incubation. (a) Particles with 50 μM probe were incubated with varying amounts of Exonuclease I for up to 60 minutes. Shown is probe-region flourescence after rinsing and dying with PicoGreen. (b) Particles were incubated with target DNA and subsequently subjected to exonuclease digestion. Shown is the resulting flourescent signal, background signal, and difference between the two (the "target" signal).*

If exonuclease is used in great excess, nonspecific digestion of double-stranded complexes may occur. To assess this, we incubated our test particles for one hour with 5 fmol DNA target ($T_{7a,D}$) and then for 30 minutes with varying concentrations of Exonuclease I, ranging from 0.25 U – 20 U. By subtracting the background signal (particles incubated with no target) from the sample signal, we obtained the corresponding "target signal" for each exonuclease concentration used. As shown, the signal is depleted at higher exonuclease concentrations. Again using a conservative approach, we decided to use 1 U of Exonuclease I for all subsequent experiments.

Another consideration that will be important when assessing the sensitivity of this method is the noise of background measurements. The background fluorescence seen using this method is a result of undigested, single-stranded probe, which provides a slight fluorescent enhancement of the PicoGreen stain. To investigate the effect of probe concentration on resulting noise (standard deviation of the signal), we assessed particles with precursor probe concentrations ranging from 5 – 50 μM. After exonuclease digestion, the particles were incubated with PicoGreen and fluorescent measurements were taken over ten particles. The results are shown in Figure 6.5 below.

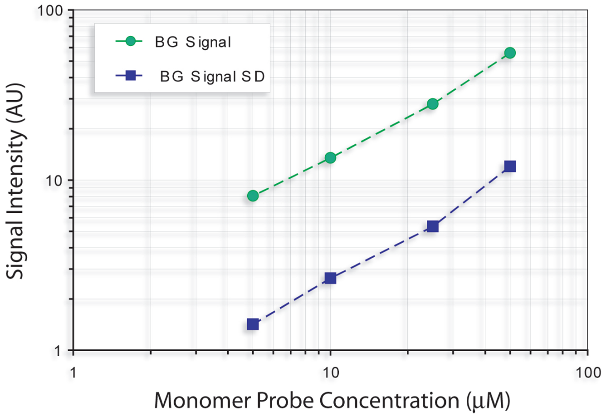

Fig. 6.5: *Assessment of noise with varying precursor probe concentrations. Particles made with monomer solutions containing 5, 10, 25, or 50 μM probe were digested with Exonuclease I and subsequently measured for fluorescent signal and signal standard deviation (SD).*

As may be expected, the residual fluorescent signal (from undigested probe) is proportional to the amount of probe originally incorporated, showing a linear trend. The "noise" in these measurements also appears to be linear with respect to incorporated probe. Although lower probe concentrations give less noise, it will be shown in the next chapter4 that hybridization rate is related to probe concentration – for this reason, we chose to use a precursor probe concentration of 10 μM as the standard for this labeling scheme.

6.4 Method Validation via mRNA Profiling

One approach to drug discovery is to determine how a given chemical effects the production of RNA targets that are associated with a disease [42]. This can be achieved by measuring transcription levels of messenger RNA (mRNA) targets from two cell populations, one which has been treated with the drug and another that has not. Typically, the RNA harvested from these cell samples needs to be amplified and labelled to allow for detection via fluorescence. This can be accomplished in several ways, including ligation-mediation amplification (LMA) and *in vitro* transcription (IVT) [169]. To validate our method for mRNA profiling, we performed assays using samples prepared by both LMA and IVT. The sample preparation, target selection, capture probe design, and Luminex assays for the experiments shown in this section were done by Dr. Golub's group at the Broad Institute.

Ligation-mediated amplification is used to selectively amplify only transcripts of interest. During amplification, each transcript is adapted with a unique 24bp capture sequence (user defined) and biotin modification for post-hybridization detection. The resulting LMA samples contain mostly targets that are relatively small ($\sim$ 100bp) and similar in size. To validate the use of encoded hydrogel particles for expression profiling with LMA samples, we performed a 5-plex experiment, comparing the results to those obtained using a commercially-available system (Luminex). The target RNAs were chosen such that two were known to be upregulated with drug treatment, two downregulated, and one unaffected to act as an internal control. The LMA samples were prepared using RNA from HELA cells treated with a drug (tretinoin, all-trans retinoic acid, ATRA) or vehicle (dimethyl sulfoxide, DMSO) alone.

We used multi-probe particles, as shown in Figure 6.6a, to simultaneously assay for all five targets using probes for their associated capture sequences (denoted LUA7, 27, 59, 68, and 95). We used a monomer blend consisting of 25% PEG-DA$_{700}$, 35% PEG$_{200}$, 5% Darocur, and 35% 3× TE buffer. As discussed in Section 6.2, this provided a larger pore size suitable for streptavidin-based reporting. The monomer was mixed at 9:1 with 50bp DNA probes to achieve a final probe concentration of 100 μM in the precursor solution.

The particles were hybridized with LMA samples for 2 hours at 45^{o}C (protocol 2.3.11), after which targets were fluorescently labelled using a streptavidin-conjugated reporter (protocol 2.3.12). Fluorescent scans were then taken for five particles from each sample and averaged (Figure 6.6b). Using the internal control (LUA95) to normalize target signals, the differential expression (log(ATRA signal/DMSO signal) was calculated for each target and plotted in Figure 6.6c. The data agreed

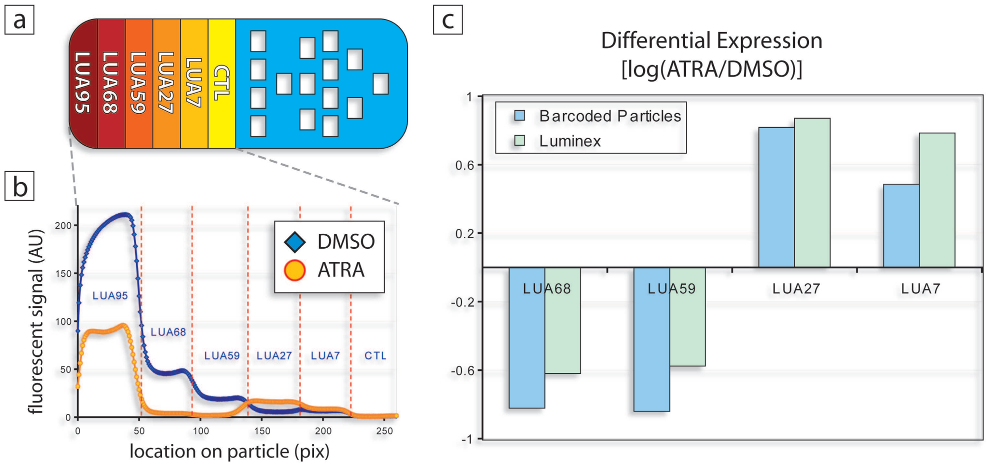

Fig. 6.6: *Expression profiling of mRNA prepared by ligation mediated amplification (LMA). (a) Multifunctional particles were designed to test for five mRNA targets with a built-in negative control and arbitrary code. (b) After hybridization with LMA samples (ATRA or DMSO), the probe-regions of several particles were analyzed to quantify the amount of target captured (using fluorescent signal). (c) Target quantities were normalized using the internal control (LUA95) and their differential expression was plotted alongside expression data measured using a Luminex system.*

very well with that found using the Luminex system, correctly showing up- and down-regulation of the mRNA targets.

In contrast to LMA preparation, when using *in vitro* transcription, RNA is amplified and biotinylated blindly – the result is a complex mixture of nucleic acids with a broad range of sizes. These characteristics make IVT samples particularly difficult to assay. To assess our system with this more challenging assay, we again performed a 5-plex experiment. We used multifunctional particles similar to those used in the LMA experiment (with 50bp probes for targets CD38, CCL2, ASS1, ASNS, and ABT1) with an identical hybridization and labelling procedures. The differential expression data from this experiment is shown Figure 6.7. As can be seen, our results were once again similar to those found using the Luminex system.

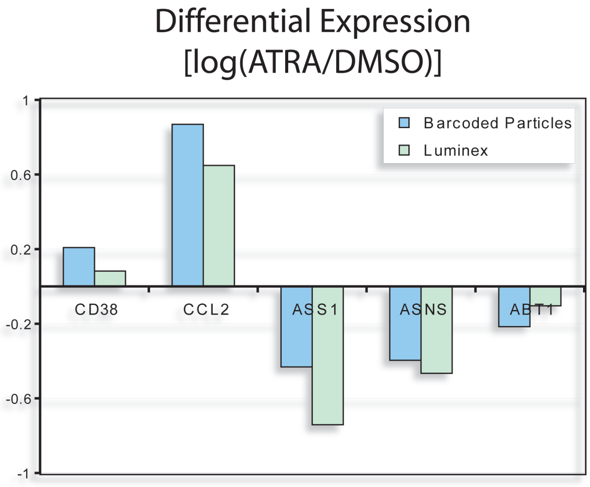

Fig. 6.7: *Expression profiling of mRNA prepared by in vitro transcription (IVT). Five targets of interest were quantified using RNA obtained from ATRA and DMSO-treated cells. Shown is the differential expression of those targets alongside data obtained using a Luminex system.*

6.5 Conclusions

In optimizing our system for real world applications, we have introduced a simpler encoding scheme that can accommodate medium-density screening with a single detector. We have also investigated the effect of particle composition on probe incorporation and hybridization signal. Furthermore, in order to eliminate sequence bias during target labeling, we have developed a new method for directly labeling target-probe complexes. The method is extremely rapid and low cost. Lastly, we validated our system for mRNA profiling, showing favorable comparison to one of today's state-of-the art screening systems.

CHAPTER 7

Kinetic Modelling and Assessment of Performance

Having optimized particle composition and target labeling schemes, we wanted to understand the kinetics behind target hybridization. As such, we developed mathematical models to give insight into the parameters governing hybridization dynamics. Using our findings to optimize particle design, we then investigated the performance of our system, probing both sensitivity and specificity. We will show that our system can be used for applications that require inexpensive and rapid labeling, attomole-sensitivity, single-nucleotide specificity, and operation over a broad dynamic range.

7.1 Modelling Hybridization

Before assessing the sensitivity of our system, we developed models to understand the kinetics of target hybridization. We consider hydrogel particles with thickness $2l$ and a probe region of width d that is flanked by negative control regions, as shown in Figure 7.1. For simplicity, we will view this system as one-dimensional, using a single coordinate system with directionality into the particle surface (this simplification will be justified for the specific models subsequently presented). We will assume perfect mixing (validated later in Section 7.1.3) meaning that while species in particles vary with respect to position and time, the target in solution varies only with time.

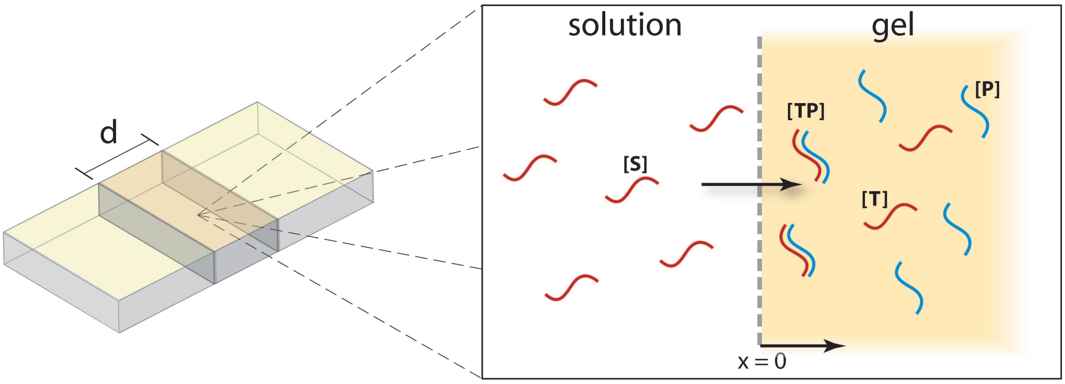

Fig. 7.1: *Schematic of hybridization. Target oligonucleotes (S is solution, T within particles) in solution diffuse into the particle surface and bind with incorporated probes P to form complexes TP.*

During sample hybridization, target oligonucleotides in solution penetrate the particles and bind with complementary probes that are homogeneously distributed throughout a designated region of the particle (Figure 7.1).

The basic equations governing the concentrations (mol/L) of target ($[T](x,t)$), probe ($[P](x,t)$), and target-probe complexes ($[TP](x,t)$) in the particles, as well as the target in solution ($[S](t)$)are as follows:

$$\frac{\partial[T]}{\partial t} = D_{gel}\frac{\partial^2[T]}{\partial x^2} - k_a[P][T] + k_d[TP] \tag{7.1}$$

$$\frac{\partial[P]}{\partial t} = -k_a[P][T] + k_d[TP] \tag{7.2}$$

$$[TP] = [P]_o - [P] \tag{7.3}$$

$$V_s\frac{\partial[S]}{\partial t} = D_{gel}N_pA_p\frac{\partial[T]}{\partial x}|_{x=0} \tag{7.4}$$

where t is time, D_{gel} is the diffusivity of target in the gel, k_a and k_d are the second-order association and first-order dissociation constants, respectively, V_s is the sample volume, x is distance into to the particle surface, N_p is the number of particles, and A_p is the surface area of the probe region per particle. The initial conditions of the problem are such that:

$$[T](x,0) = 0 \tag{7.5}$$

$$[P](x,0) = [P]_o \tag{7.6}$$

$$[TP](x,0) = 0 \tag{7.7}$$

$$[S](t=0) = [S]_o \tag{7.8}$$

The boundary conditions for target are determined by concentration matching at the particle surface (ie. using a partition coefficient of 1), and zero-flux at the particle center due to symmetry, as given by:

$$[T](0,t) = [S](t) \tag{7.9}$$

$$\frac{\partial [T]}{\partial x}|_l = 0. \tag{7.10}$$

These equations provide the basic problem statement. There are two regimes we are interested in studying. A “reaction-diffusion” model will be developed to design particles for high-sensitivity applications, while a “diffusion-limited” reaction model will be developed to design particles for applications requiring signal suppression. The latter will be useful in situations where certain targets are vastly abundant compared to others being detected, which is commonly the case in biological samples. For each model, we will find the appropriate variable scalings, and then using some approximations, find simple analytical solutions that give insight to hybridization kinetics.

7.1.1 Reaction Diffusion Model

In order to maximize the rate of target hybridization, it is desirable to use particles with probe incorporated at a high concentration – this is the first scenario we will investigate. We are interested in a “reaction-diffusion” (RD) regime where:

1) probe is in great excess (ie. $V_s[S]_o << V_p[P]_o$),

2) hybridization is very strong at the target concentration (ie. $K_d = k_d/k_a \ << \ [S]_o$), and

3) the reaction rate is much faster than the rate of diffusion over the particle thickness.

With probe in great excess, its concentration will not vary substantially during hybridization (ie. $[P](x,t) \sim [P]_o$). Thus, the reaction rates for the problem are dictated by the lumped association constant, $k_a[P]_o$, and dissociation constant, k_d. With strong hybridization and moderate probe concentrations, as used with our system, the rate of association is dominant (ie. $k_a[P]_o \ >> \ k_d$). Hence, although these two reaction rates exist, it is this association rate that we are interested in.

Another important rate for this problem is that of target diffusion through the hydrogel composing particles. This rate is governed by the diffusivity of target in the gel (D_{gel}) and the smallest particle lengthscale (half the particle thickness l), as D_{gel}/l^2. The Damköhler number gives a ratio of the reaction rate to the diffusion rate, which for the case of the association reaction is $Da = k_a[P]_o/\left(D_{gel}/l^2\right)$. For our system in the RD regime, Da is on the order of 100 (parameter estimates are given later).

We are interested in scaling the equations in order to make simplifications based on estimated parameter values. Because the Damköhler number is very large, reaction will occur much faster than targets can diffuse to the center of the particles. As such, the distance over which species evolution is occurring (ie. the penetration depth) is very small compared to the particle thickness, which appears to be semi-infinite in this regime. This indicates that the use of the natural lengthscale for the problem, (ie. $\widetilde{x} = x/l$), would not be an appropriate choice to scale the x coordinate. A more suitable scaling can be accomplished using the Damköhler number, such that $\eta = \widetilde{x} Da^{\frac{1}{2}}$. The exponent of 1/2 was selected to cause the prefactor in front of the diffusion term in Equation 7.1 to be unity upon rearrangement and scaling. This lengthscale gives a boundary layer thickness on the order of $\delta_{gel} \sim l/Da^{1/2} \sim 1\ \mu$m. Importantly, this length is much smaller than the dimensions of a probe region, which are typically on the order of 100 × 50 × 30 μm. This indicates that the reduction of this system to a 1-D model is a decent approximation.

As for the concentration of species in the system, natural scaling for $[S]$ and $[T]$ is $[S]_o$, which represents the highest concentration of target that can be achieved in the solution or particle. The probe concentration is expected to vary only slightly, and thus $[P]_o$ is an appropriate scale. To find the scale for $[TP]$, we can consider a scenario where all of the target from solution is bound homogeneously throughout the particle volume, giving a concentration of $V_s[S]_o/(N_p \times V_p) = v[S]_o$, where V_p is probe region volume per particle and v is the ratio of sample to total particle volume such that $v = V_s/(N_p \times V_p)$. Thus, our scaled variables become:

length: $\eta = \widetilde{x} Da^{\frac{1}{2}} = x\left(Da^{\frac{1}{2}}/l\right)$;

concentrations: $\widetilde{T} = \frac{[T]}{[S]_o}$; $\widetilde{P} = \frac{[P]}{[P]_o}$; $\widetilde{TP} = \frac{[TP]}{v[S]_o}$; $\widetilde{S} = \frac{[S]}{[S]_o}$.

The timescale we are interested in is that needed to obtain the maximum number of hybridized complexes, which in the case of probe excess happens when all of the target molecules are captured from solution. Thus, for the *RD* model we are most interested in characterizing the evolution of $[S]$ over time. By rewriting our equations using the scalings above and finding our timescale using Equation 7.4, which describes target depletion from solution, we find the dimensionless time for this problem to be:

$$\tau = t/\left(\frac{V_s l}{D_{gel} N_p A_p Da^{\frac{1}{2}}}\right) = t/\left(\frac{V_s}{N_p A_p \left(D_{gel} k_a [P]_o\right)^{\frac{1}{2}}}\right).$$

After scaling, Equations 7.1 – 7.4 can be rewritten as:

$$\frac{1}{v' Da^{\frac{1}{2}}} \frac{\partial \widetilde{T}}{\partial \tau} = \frac{\partial^2 \widetilde{T}}{\partial \eta^2} - \widetilde{P}\widetilde{T} + \alpha \widetilde{TP} \tag{7.11}$$

$$\frac{v}{v' Da^{\frac{1}{2}}} \frac{\partial \widetilde{P}}{\partial \tau} = -\widetilde{P}\widetilde{T} + \alpha \widetilde{TP} \tag{7.12}$$

$$v \epsilon_s \widetilde{TP} = 1 - \widetilde{P} \tag{7.13}$$

$$\frac{\partial \widetilde{S}}{\partial \tau} = \frac{\partial \widetilde{T}}{\partial \eta}|_{\eta=0} \tag{7.14}$$

where the lumped parameters are given by:

$Da = \frac{k_a[P]_o}{\left(D_{gel}/l^2\right)}$; $v = \frac{V_s}{N_p V_p}$; $v' = \frac{V_s}{N_p A_p l}$; $\epsilon_s = \frac{[S]_o}{[P]_o}$; $\alpha = \frac{k_d}{ka[P]_o} = \frac{K_d}{[P]_o}$.

In these equations, α represents a ratio of the two Damköhler numbers of the system, for association and dissociation rates. The parameters v and v' represent sample-to-particle volume ratios. While $N_p V_p$ is the actual total particle volume (used in v), $N_p A_p l$ is the effective volume projected from the surface area (used in v'). The scaled initial conditions from Equations 7.5 – 7.8 are:

$$\widetilde{T}(\eta, 0) = 0 \tag{7.15}$$

$$\widetilde{P}(\eta, 0) = 1 \tag{7.16}$$

$$\widetilde{TP}(\eta, 0) = 0 \tag{7.17}$$

$$\widetilde{S}(\tau = 0) = 1 \tag{7.18}$$

while the boundary conditions, in the limit where $Da >> 1$ and so $\frac{\partial \widetilde{T}}{\partial \eta}|_{Da^{\frac{1}{2}}} \rightarrow \frac{\partial \widetilde{T}}{\partial \eta}|_{\infty}$, from Equations 7.9 – 7.10 are now:

$$\widetilde{T}(0, \tau) = \widetilde{S}(\tau) \tag{7.19}$$

$$\frac{\partial \widetilde{T}}{\partial \eta}|_{\infty} = 0. \tag{7.20}$$

Typical values for the parameters of this problem are $k_a \sim 10^6 Ms^{-1}$, $k_d \sim 10^{-7} s^{-1}$, $[P]_o \sim 10^{-5} M$, $[S]_o \sim 10^{-12} M$, $V_s \sim 10^{-4} L$, $N_p \sim 10$, $V_p \sim 10^{-10} L$, $A_p \sim 10^{-8} m^2$, $l \sim 10^{-5} m$, and $D_{gel} \sim 10^{-11} m^2 s^{-1}$, giving $Da \sim 10^2$, $v \sim v' \sim 10^5$, $\epsilon_s \sim 10^{-7}$, and $\alpha \sim 10^{-4}$. As such, several terms in these equations are small and can be removed. In particular, we can combine Equations 7.11 and 7.13 to obtain:

$$\frac{1}{v' Da^{\frac{1}{2}}} \frac{\partial \widetilde{T}}{\partial \tau} = \frac{\partial^2 \widetilde{T}}{\partial \eta^2} - (1 - v\epsilon_s \widetilde{TP})\widetilde{T} + \alpha \widetilde{TP} \tag{7.21}$$

which, after eliminating small terms, reduces simply to:

$$0 = \frac{\partial^2 \widetilde{T}}{\partial \eta^2} - \widetilde{T}. \tag{7.22}$$

This indicates that target evolution in the particle is quasi-steady over the timescales of the problem. The general solution for this equation has the form of $\widetilde{T} = C_1 e^{-\eta} + C_2 e^{\eta}$, where C_1 and C_2 are constants to be determined. We can use the boundary conditions in Equations 7.19 and 7.20 to find:

$$\widetilde{T} = \widetilde{S} e^{-\eta}. \tag{7.23}$$

We can use this expression for $\widetilde{T}$ in Equation 7.14 to solve for $\widetilde{S}$, finding that:

$$\widetilde{S} = e^{-\tau}. \tag{7.24}$$

This result suggests the exponential decay of target from solution, governed by a timescale that incorporates probe concentration, sample volume, particle surface area, and diffusivity of target in the gel particles.

The depletion of target from solution is inversely related to formation of target-probe complexes in the particles. Using Equation 7.24, we can estimate the fluorescent signal intensity (I_{RD}) seen on the particles in the RD regime using

$$I_{RD} = \frac{F_e V_s [S]_o (1 - e^{-\tau})}{N_p A_p} \tag{7.25}$$

where F_e is a signal efficiency factor (with units $AU\ m^2/mol$) that takes into account fluorophore and detector efficiencies as well as the ratio of detection to hybridization surface areas (which is 2 in the case of detection through 2 particle faces). We can scale the signal using $\widetilde{I}_{RD}N_p = I_sA_p/(F_eV_s[S]_o)$ to simply give:

$$\widetilde{I}_{RD}N_p = 1 - e^{-\tau}. \tag{7.26}$$

This result indicates that for maximum sensitivity, long hybridization times should be used with few particles and minimum probe region surface area.

7.1.2 Reaction-Limited Model

Often times, a particular target is in great excess with respect to other targets being assayed. This difference can be 3 – 4 orders of magnitude in some cases. With similar hybridization kinetics, this would lead to differences in fluorescent signal that would also vary by several orders of magnitude, thus requiring a detector that can accommodate a vast dynamic range. To overcome this limitation, particles may be designed to suppress hybridization kinetics. Thus, we present a “reaction-limited” (RL) regime where:

1) target is in great excess (ie. $V_s[S]_o >> V_p[P]_o$),

2) hybridization is very strong at the target concentration (ie. $K_d = k_d/k_a << [S]_o$), and

3) the rate of diffusion is much faster than the rate of reaction over the particle thickness.

It is important to realize that there are two timescales for the RL regime. At short times on the order of l^2/D ($\sim$ 10 sec in our case), transport is governed predominantly by the diffusion of target into particles. At “long” times much larger than the initial diffusion timescale, transport is governed by reaction. As incubations are conducted over hours, we will be investigating hybridization kinetics at “long” times.

The scalings for this regime are different. As diffusion happens much faster than reaction ($Da \sim 0.1$), we can expect spatial homogeneity of species in the particles (at “long” times as previously discussed) – this implies that l should be used to scale length. Because target is in great excess and the probes in particles may become saturated, $[TP]$ must be scaled by $[P]_o$. The scaling of target species (S and T) by the initial solution concentration ($[S]_o$) is still appropriate. Thus, for the RL regime, the scaled variables are:

length: $\widetilde{x} = x/l$;
concentrations: $\widetilde{T} = \frac{[T]}{[S]_o}$; $\widetilde{P} = \frac{[P]}{[P]_o}$; $\widetilde{TP} = \frac{[TP]}{[P]_o}$; $\widetilde{S} = \frac{[S]}{[S]_o}$.

The timescale we are now interested in is that for probe saturation, since in this regime it is impossible to bind all targets from solution. Thus, for the RL model, we will be investigating the evolution of $[P]$ over time. The dimensionless time that characterizes the rate of probe depletion (found using Equation 7.2) is given by:

$$\tau = t\left(k_a[S]_o\right).$$

Since target is at great excess, we can make a scaling argument to show that its concentration in solution ($[S]$) does not change significantly over time. A mass balance on target, which includes the amount in solution ($[S](t)$) and that in particles ($[T](x,t)+[TP](x,t)$, integrated over the particle volume), can be written as:

$$V_s[S]_o = V_s[S] + N_p\int_0^{V_p}[T]dV + N_p\int_0^{V_p}[TP]dV. \tag{7.27}$$

which upon scaling (using $\mathrm{d}\widetilde{V} = dV/V_p$ to scale the arbitrary volume unit) becomes:

$$1 = \widetilde{S} + \frac{1}{v}\int_0^1 \widetilde{T}d\widetilde{V} + \frac{1}{v\epsilon_s}\int_0^1 \widetilde{TP}d\widetilde{V}. \tag{7.28}$$

Using typical parameter values for this regime as given later in this section, the orders of v and ϵ_s are 10^5 and 10^{-2}, respectively. This leads to the expected conclusion that at all times, $\widetilde{S} \cong 1$.

This simplification for $\widetilde{S}$ eliminates the need for Equation 7.4 from our governing equations, which upon scaling are now:

$$\epsilon_s\frac{\partial\widetilde{T}}{\partial\tau} = \frac{1}{Da}\frac{\partial^2\widetilde{T}}{\partial\widetilde{x}^2} - \widetilde{P}\widetilde{T} + \kappa_s\widetilde{TP} \tag{7.29}$$

$$\frac{\partial\widetilde{P}}{\partial\tau} = -\widetilde{P}\widetilde{T} + \kappa_s\widetilde{TP} \tag{7.30}$$

$$\widetilde{TP} = 1 - \widetilde{P} \tag{7.31}$$

where the lumped parameters are given by:

$$\epsilon_s = [S]_o/[P]_o;\ Da = \frac{k_a[P]_o}{(D_{gel}/l^2)};\ \kappa_s = K_d/[S]_o.$$

The initial conditions for this regime, found by applying the appropriate scaling to Equations 7.5 – 7.7, become:

$$\widetilde{T}(\widetilde{x},0) = 0 \tag{7.32}$$

$$\widetilde{P}(\widetilde{x},0) = 1 \tag{7.33}$$

$$\widetilde{TP}(\widetilde{x},0) = 0 \tag{7.34}$$

and the boundary conditions are:

$$\widetilde{T}(0,\tau) = 1 \tag{7.35}$$

$$\frac{\partial\widetilde{T}}{\partial\widetilde{x}}|_1 = 0. \tag{7.36}$$

Typical parameter values for this regime are $k_a \sim 10^6 Ms^{-1}$, $k_d \sim 10^{-7}s^{-1}$, $[P]_o \sim 10^{-8}M$, $[S]_o \sim 10^{-10}M$, $V_s \sim 10^{-4}L$, $N_p \sim 10$, $A_pl \sim V_p \sim 10^{-10}L$, $D_{gel} \sim 10^{-11}m^2s^{-1}$, and $l \sim 10^{-5}m$, giving $v' \sim 10^5$, $Da \sim 10^{-1}$, $\epsilon_s \sim 10^{-2}$, and $\kappa_s \sim 10^{-3}$. If we drop all but the dominant terms from

Equation 7.29, we obtain:

$$0 = \frac{\partial^2 \widetilde{T}}{\partial \widetilde{x}^2}. \tag{7.37}$$

The general solution for this equation has the form $\widetilde{T} = C_1\widetilde{x} + C_2$, where again C_1 and C_2 are constants to be determined. By applying the boundary conditions in Equations 7.35 and 7.36, we obtain:

$$\widetilde{T} = 1. \tag{7.38}$$

This result shows us that the the system appears to be spatially homogenous, and in fact looks spatially *zero*-dimensional. This represents a simplification even over our 1-D approximation. After dropping insignificant terms, this solution can be used in Equation 7.30 to give:

$$\frac{\partial \widetilde{P}}{\partial \tau} = -\widetilde{P} \tag{7.39}$$

which has the solution:

$$\widetilde{P} = e^{-\tau}. \tag{7.40}$$

This solution can now be used in Equation 7.31 to find the concentration of target-probe complex within the particles as:

$$\widetilde{TP} = 1 - e^{-\tau}. \tag{7.41}$$

This shows that in the RL regime, hybridization kinetics depend only on the association rate constant and initial target concentration, and are independent of diffusivity and probe region surface area, both of which were important in the reaction-diffusion regime. In this regime, the fluorescent signal is cumulative over complex formation through the entire particle thickness, $2l$, and is given by:

$$I_{RL} = F_e[P]_o(2l)\left(1 - e^{-\tau}\right) \tag{7.42}$$

where F_e is again the signal efficiency factor that characterizes the signal obtained per mole of target bound. We can scale the signal as $\widetilde{I}_{RL} = I_{RL}/\left(F_e[P]_o(2l)\right)$ to obtain:

$$\widetilde{I}_{RL} = 1 - e^{-\tau}. \tag{7.43}$$

As expected, the results suggest that we can significantly suppress hybridization signal for abundant species, easily showing 1000× reduction compared to the signal that would be observed using the "high-sensitivity" particle design as presented in the RD model. One important consideration for this regime is the avoidance of probe saturation. For example, using our estimation of $k_a \sim 10^6$, a 2 hour incubation (typical) with ~ 7 fmol (7×10^{-15} moles) of target would result in $\sim 63\%$ saturation of probe ($\tau = 1$) regardless of the initial probe concentration.

7.1.3 Perfect Mixing Assumption

During hybridization, particles are vigorously mixed with orbital shaking, providing convective mass transfer throughout the sample. To assess the assumption of perfect mixing, we will compare two timescales – one that characterizes target transport in solution close to the particle surface and the other that describes target depletion within particles. Our perfect mixing assumption will be valid if we find that transport in solution happens much faster than depletion within particles.

We will first estimate the solution-phase concentration boundary layer thickness (δ_{sol}) seen close to a particle surface in the presence of convective transport. This can be done using scaling arguments, as presented in several texts including References [170] and [171]. For this order of magnitude analysis, we will use a relationship developed for laminar flow over a flat plate, which has been well-studied and experimentally confirmed.

There are two important dimensionless groups for this analysis, which are the Reynolds (Re) and Schmidt (Sc) numbers given by:

$$Re = \frac{\rho U L}{\mu}, \quad \text{and} \quad Sc = \frac{\mu}{\rho D_{sol}}$$

where ρ, μ, U, L, D_{sol} are fluid density, fluid viscosity, bulk flow velocity, characteristic particle lengthscale, and diffusivity of target in solution, respectively. While Re describes the ratio of convective to viscous momentum transfer, Sc is a ratio of and viscous to diffusive transfer.

In our system, typical parameter values are $\rho \sim 10^3 kg/m^3$, $\mu \sim 10^{-3} Pas$, $L \sim 10^{-5} m$, $D_{sol} \sim 10^{-10} m^2/s$. With rapid mixing at 1800 rpm in a microtube, we can estimate U to be on the order of $10^{-1} m/s$. These estimates give $Re \sim 10$ and $Sc \sim 10^4$, which can be used to estimate the concentration boundary layer thickness as:

$$\frac{\delta_{sol}}{L} \sim Re^{-\frac{1}{3}} Sc^{-\frac{1}{3}}. \tag{7.44}$$

This suggests that for our system, the diffusive boundary layer thickness is on the order of $\delta_{sol} \sim 10^{-6} m$. Using this thickness, we can estimate the timescale for diffusion from solution to the particles to be:

$$t^*_{sol} = \frac{\delta^2_{sol}}{D_{sol}} \sim 10^{-2} s. \tag{7.45}$$

Now that we have an estimate for the solution-phase transport timescale, we will estimate the timescale for target consumption within the particles. With a moderate to high probe concentration, chemical reaction provides the dominant means for target consumption, with a timescale given by $t^*_{gel} \sim 1/\left(k_a [P]_o\right)$. Using an estimate of $k_a \sim 10^6 M^{-1} s^{-1}$ and the highest incorporated probe concentration student in our system (10^{-5} M), we find that $t^*_{gel} \sim 10^{-1}$ sec.

Importantly, the timescale for target consumption is an order of magnitude larger than the timescale of diffusive transport in solution. This indicates that target is diffusing to the particle surface much faster than it is consumed within the particle – such constant replenishing ensures that the concentration of target at the surface is the same as that seen in bulk. This result justifies our estimation of perfect mixing.

7.2 Experimental Validation of Reaction-Diffusion Model

We investigated the validity of our RD model by performing kinetic studies using particles with varying probe concentrations (probe P_{7a}), probe-region surface areas (which is proportional to the probe region stripe thickness d), and particle numbers. In each case, we incubated distinct particle samples with 500 attomoles of target ($T_{7a,D,F}$) at room temperature. At various timepoints, particles from a sample were measured for fluorescence. The results are shown in figure 7.2 below.

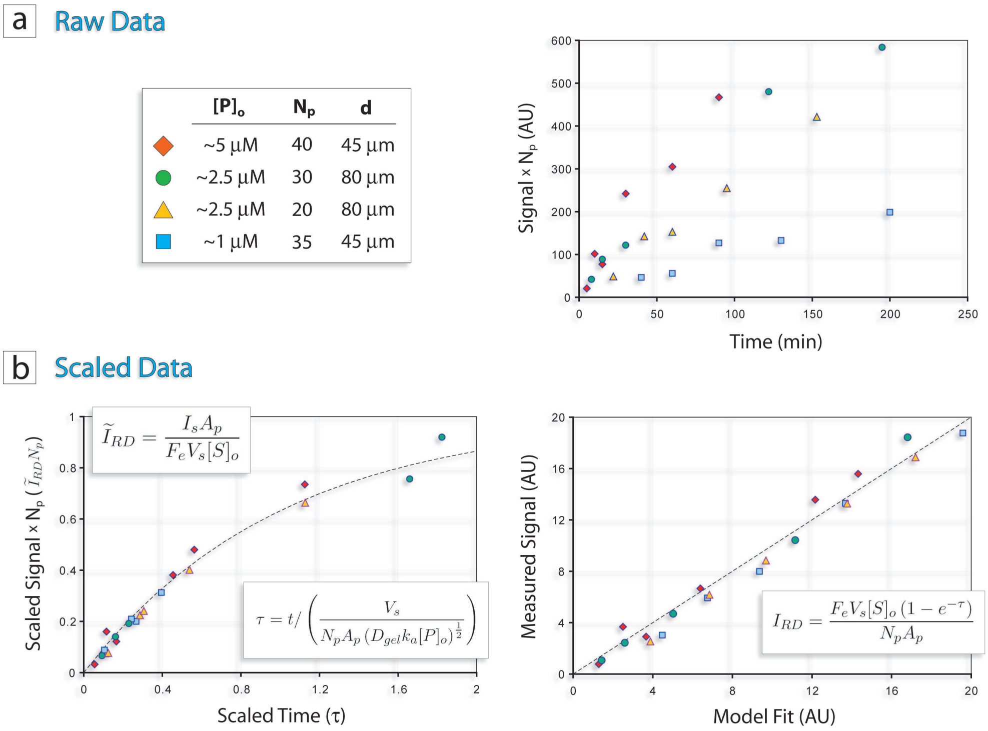

Fig. 7.2: *Validation of model predictions. Particles with varying probe concentrations* ($[P]$)*, stripe width* (d)*, and numbers* (N_p) *were incubated with 500 attomoles of complementary target and their fluorescence was measured over time. (a) Raw data showing the average particle signal multiplied by the number of particles. (b) The same data shown in (a) that has been plotted using the predicted timescale (left) along with comparison of predicted and measured particle signals (right).*

As the *RD model* predicts the depletion of target from solution, we have presented the "total signal" as a sum of signal across all of the particles (N_p) present in a sample. For each data point, the signal averages were taken over five particles in the sample. As can be seen, even though the parameter space seems somewhat limited, the raw data shows large variation of target consumption over time (Figure 7.2a, right).

We scaled the data using the relationship in Equation 7.26 to find that when applying the predicted timescale, the data falls along a similar trend (Figure 7.2b, left). The model also fits nicely with measured signal for each data point as shown in Figure 7.2b on the right. Importantly, the fit shown in figure 7.2b was made by setting $k_a D_{gel}$ to $5.5 \times 10^{-5}\, m^2 s^{-2} M^{-1}$, which agrees well with our estimates of $D_{gel} \sim 10^{-11}\, m^2 s^{-1}$, and $k_a \sim 10^6 M^{-1} s^{-1}$.

7.3 Experimental Validation of Reaction-Limited Model

We tested the validity of our *RL* model by again performing kinetic studies, but this time using very low probe concentrations. Particles were designed with probe regions that that were 50 μm wide, with probe (P_{7a}) concentrations of $\sim$ 50 – 200 nM ($\sim$ 10% incorporation efficiency with 0.5 – 2 μM probe in monomer). As before, all particles were $\sim$ 30 μm thick and 100 μm wide.

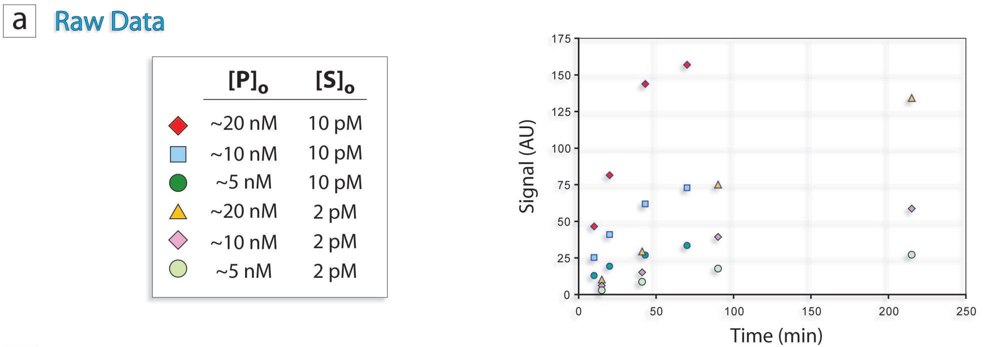

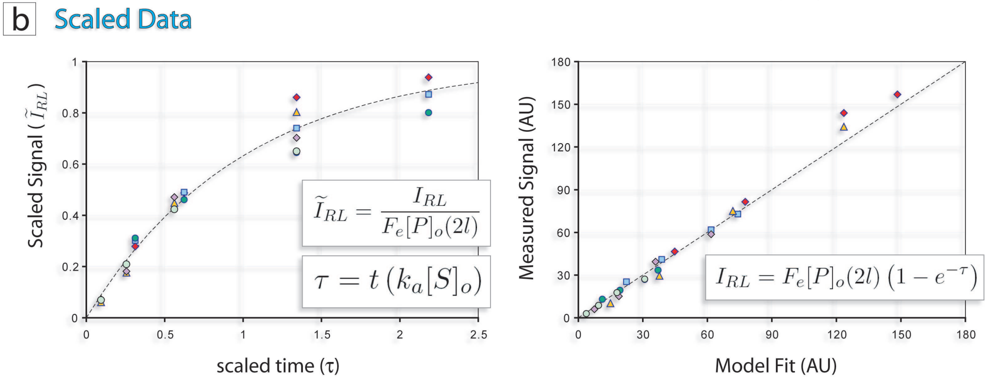

Fig. 7.3: *Experimental validation of Reaction-Limited Model. Particles with varying probe concentrations* ($[P]_o$) *were incubated with complementary DNA targets at two different concentrations* ($[S]_o$) *and the resulting fluorescence was measured over time. (a) Raw data showing the measured probe-region fluorescent signals. (b) The same data shown in (a) that has been plotted using the predicted timescale (left) along with comparison of predicted and measured particle signals (right).*

For these experiments, particles were incubated with either 1 or 5 fmoles of complementary target (T_{7a}), corresponding to concentrations of 2 or 10 pM, and subsequently labelled using PicoGreen *without* probe digestion (contrary to the protocol described in Section 6.3). Briefly, particles were incubated with target for the desired time, rinsed 2× with TET, 1× with PTET, and incubated with PicoGreen at 1:1000 for 15 minutes. This labelling method was used because PicoGreen provided a much higher fluorescent signal than fluorescein and probe concentrations were so low that the unbound probes were found to give negligible fluorescence, making it very convenient and rapid labelling method.

The results of the *RL model* validation experiments are shown in Figure 7.3. For each data point, probe-region fluorescence signals was averaged over five particles. As can be seen in Fiugre 7.3a, the raw data shows wide variability with respect to both probe and target concentrations.

We scaled the data using the relationship in Equation 7.43, fitting F_e and k_a, to find good agreement between experiment and model. Contrary to what was seen in the *RD model*, in this model the parameters k_a and D_{gel} are not coupled. As such, we were able to estimate association rate constant, finding that $k_a \sim 5 \times 10^6 \ M^{-1}s^{-1}$. Having previously estimated the product $k_aD_{gel} \sim 5.5 \ m^2s^{-2}M^{-1}$, we now see that $D_{gel} \sim 1 \times 10^{-11}m^2s^{-1}$. Both of these values are consistent with our parameter estimates.

7.4 Investigation of Sensitivity

With a mathematical model in place to understand hybridization, we assessed the sensitivity of our system using both labeling methods. For these sensitivity experiments, we chose to use a precursor probe concentration of 10 μM, as this was the highest level probe suitable for both labeling schemes (as described earlier). If desired, a higher probe concentration could be used with biotin/SAPE labeling to achieve faster kinetics. As hybridization is a dynamic process, sensitivity is expected to increase with hybridization time. We chose to limit hybridization times to a maximum of 3 hours, keeping the overall assay times (labeling + hybridization) around 4 hours, which is much shorter than typical assay times of commercially-available multiplexing systems.

We used Equation 7.25 to estimate the signal obtained with the given particle design, labeling scheme used, and hybridization time. We found the signal efficiency factors for the various fluorophores to be:

Fluorophore	**Efficiency factor** (F_e)
$FITC$	$2.5 \times 10^{10} \ AUm^2/mole$
$PicoGreen_{DNA/RNA}$	$1.5 \times 10^{11} \ AUm^2/mole$
$SAPE$	$1.4 \times 10^{12} \ AUm^2/mole$

Table 7.1: *Signal efficiency factors for fluorophores using our detection system.*

Using these efficiency factors, we show the expected assay sensitivities with respect to time in Figure 7.4. The total assay times include the time of incubation (variable) and that needed for target labeling, which is on the order of 90 minutes for biotin/SAPE labeling and 45 minutes for Exonuclease/PicoGreen labeling. To find the sensitivities experimentally, we incubated particles with target at varying concentrations near the expected sensitivity. For each concentration, the fluorescent signal was measured and divided by the standard deviation of the background signal to obtain a signal-to-noise ratio. A line was then fit to the SNR data to obtain and estimate of the sensitivity, which we designated as the point where SNR = 3.

Our experimentally determined sensitivities matched quite well with model predictions as shown in Figure 7.4. Importantly, we show with a 4-hour total assay time including hybridization and labeling, we can obtain ∼10 attomole sensitivity with the fast/easy Exonuclease/PicoGreen labeling scheme, and attomole-sensitivity with the biotin/SAPE scheme. These sensitivities are very favorable compared to commercially-available systems. The reason for this lies in the favorable

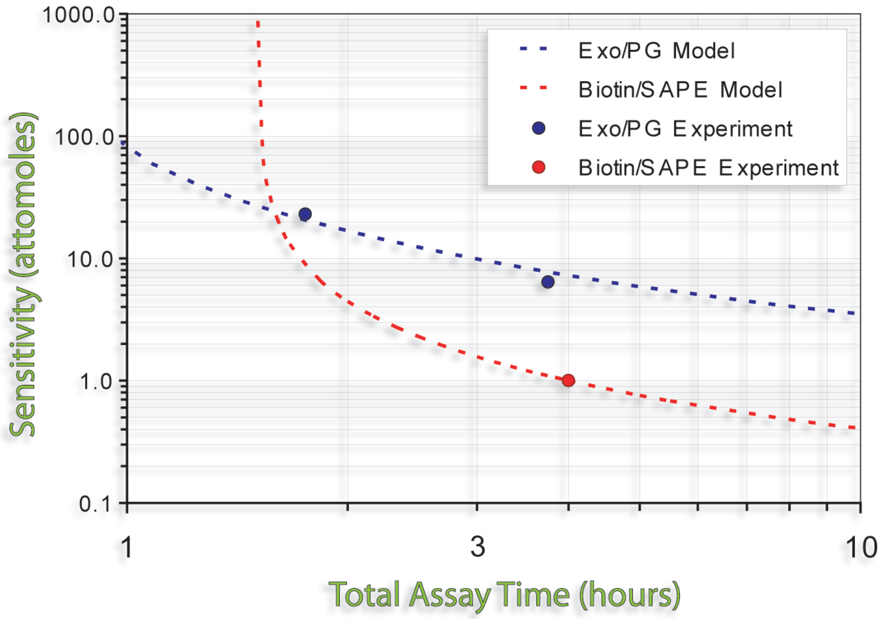

Fig. 7.4: *Assessment of assay sensitivity versus model predictions. Particles were incubated with varying amounts of target, and signal-to-noise ratios were calculated. The sensitivity was taken at the target concentration where SNR = 3. Total assay time includes both hybridization and labeling time (90 min for biotin/SAPE and 45 min for Exo/PG).*

thermodynamics of hybridization in hydrogels, as discussed in Chapter 1. Furthermore, better sensitivity could be achieved in this timeframe using a higher probe concentration with the biotin/SAPE labeling scheme.

7.5 Investigation of Specificity

When analyzing complex samples, it is necessary that each assay is specific for the targets of interest, and is invariant to fluctuations of non-target species levels. This may be very challenging when target sequences show considerable homology, as is the case with single nucleotide polymorphisms (SNPs) where sequences vary by one nucleotide. We investigated the specificity of our system across both labeling schemes used.

We synthesized particles bearing four unique regions, containing four similar probes (P_{7a}, P_{7b}, P_{7c}, and P_{7d}) that differed from each other by one or two nucleotides as shown in Figure 7.5. For use with both labeling schemes, the probes were incorporated at a precursor concentration of 10 μM. These particles were incubated with samples containing 5 fmol target oligonucleotide ($T_{7a,R}$ or $T_{7a,D,bio}$, which are specific for probe $7a$) and 500ng of total E. coli RNA to add complexity to the sample, thus mimicking a “real” assay. Incubations were one hour and the temperatures were set between 55^{o}C and 58^{o}C. The results of this study are shown in Figure 7.5.

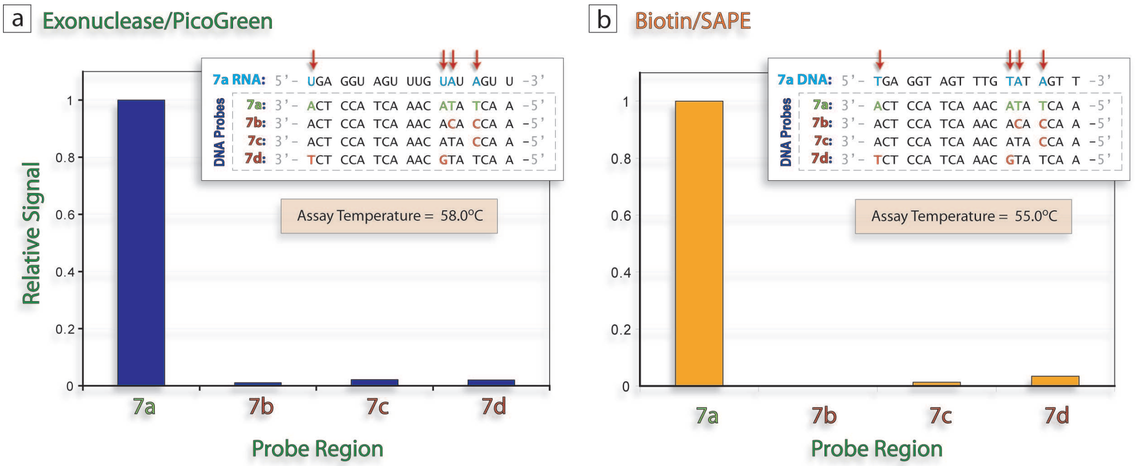

Fig. 7.5: *Assessment of assay specificity. (a) Specificity of DNA/RNA hybridization using the Exonuclease/PicoGreen labeling scheme, and (b) specificity of DNA/DNA hybridization using the biotin/SAPE labeling scheme.*

As can be seen, our method provides single-nucleotide resolution using both of the labeling schemes. In each case, non-specific hybridization was very low, below 5% relative to the intended interactions. As with sensitivity, the excellent specificity of our system is likely a result of solution-like thermodynamics observed in hydrogels.

7.6 Conclusions

We have used mathematical modelling to characterize two reaction regimes where high sensitivity or wide dynamic range are needed, validating both experimentally. We have shown that the two labeling schemes introduced in Chapter 6 can be used to provide attomole sensitivity with traditional labeling or 10-attomole sensitivity with our rapid labeling scheme, even with a relatively low probe concentration used. Using both of these labeling schemes, we demonstrated single-nucleotide specificity. These results show that our technology provides extremely high performance with very short assay times, making it an ideal platform for applications in diagnostics and drug discovery.

CHAPTER 8

Conclusions and Outlook

Throughout this thesis, we developed technologies that are already proving to be attractive for several applications in many diverse fields. As an overarching theme in this work, our methods were intentionally designed to be simple, cheap, generally-applicable, and easy to implement without use of special equipment. We have demonstrated how these methods can be used to generate structures with unprecedented intricacy and complexity, and have shown that the resulting substrates and particles can be used to meet the most demanding needs in several biological applications.

In Chapter 3, we described a method that brings together precise patterning of functional materials and bio-inert hydrogels. Unlike previous patterning methods, bead-patterned hydrogels afford accurate bead positioning, and virtually any bead chemistry using only a standard microscope. Beads may be completely encapsulated or exposed in bio-inert hydrogels, and in both cases may be applied to important biological problems such as phenotype-specific cell sorting.

In Chapter 4, we described a method for microparticle synthesis that combines projection lithography with fluid flow in a microdevice. Flow lithography represents an entirely new regime for particle synthesis, allowing unprecedented control over morphology, functionality, and materials. Though our group has combined the method with the areas of self-assembly [139], biomolecule detection [149], photonics [133], and disperse two-phase flows (Section 4.1.2), the potential of such a technology is still largely untapped.

One particularly interesting application of flow lithography is to applications in biomolecule detection. As shown in Chapter 5, access to complex morphologies and functionality makes particles generated with flow lithography ideal for multiplexed analysis. Hydrogels provide favorable, solution-like hybridization thermodynamics and bead-based systems allow for versatile, high-throughput analysis. To our knowledge, we have developed the first technology that combines both of these attributes with an encoding scheme that gives access to medium and high-density applications.

We have demonstrated the application of encoded hydrogel particles to gene profiling applications, and have optimized particle and assay designs to accommodate the many challenges existing in gene profiling. As shown in Chapter 7, we have also demonstrated a new target labeling scheme that costs only pennies to implement and shows minimal compromise of performance. With high performance, ease of use, and low cost, the encoded hydrogel particle technology appears to be an ideal candidate for many important applications including drug discovery, *in vitro* cancer diagnostics, and neonatal screening.

Although we have put a great deal of effort in designing and understanding the systems discussed in this thesis, there remails a substantial amount of work undone. In this chapter, we discuss just a few aspects of the unfinished work pertaining to bead patterning, flow lithography, and encoded gel particles.

8.1 Microwell-Directed Hydrogel Patterning

In Chapter 3 of this thesis, we described a method to generate bead-patterned hydrogels, that could be used for cell-sorting applications. Although we developed several regimes for synthesis, we did not fully demonstrate the patterning potential. One regime of bead-patterned hydrogel synthesis that might be very interesting is the microwell-directed patterning.

In the regimes shown previously, microparticles were initially patterned and hydrogel structures would subsequently be patterned around them (for example, see Figure 3.4). In a different regime, the hydrogel structures could be patterned initially and used to direct bead patterning as shown in Figure 8.1. This proof-of-principle experiment showed that it was feasible to use hydrogel microwells (roughly the size of a bead) to very precisely position magnetic microparticles.

The use of hydrogel templates for patterning of magnetic beads would greatly broaden the geometries that could be obtained. This would be especially attractive when patterning "magnetic rails" as described in the next section.

8.2 Pattern-Assisted Magnetic Cell Sorting

The concept of patterning magnetic materials in bio-inert PEG hydrogels, presented in Chapter 3 of this work, was originally developed for use in "continuous pattern-assisted cell sorting." As described briefly in Chapter 1, homogeneous populations of cells are needed for many applications. If cells are being analyzed for phenotypic characteristics, it is essential that the processes required to obtain the cells do not "activate" the cells, or that the process is fast enough to avoid phenotypic changes over the isolation timescale. As such, we designed a microfluidic scheme to rapidly sort cells in continuous fashion.

The concept behind pattern-assisted sorting revolves around the effective "steering" of magnetic bead columns laterally across a microfluidic channels using magnetic "rails" for guidance. As the columns guided diagonally across the channel, they would interact with a mixed cell stream flowing

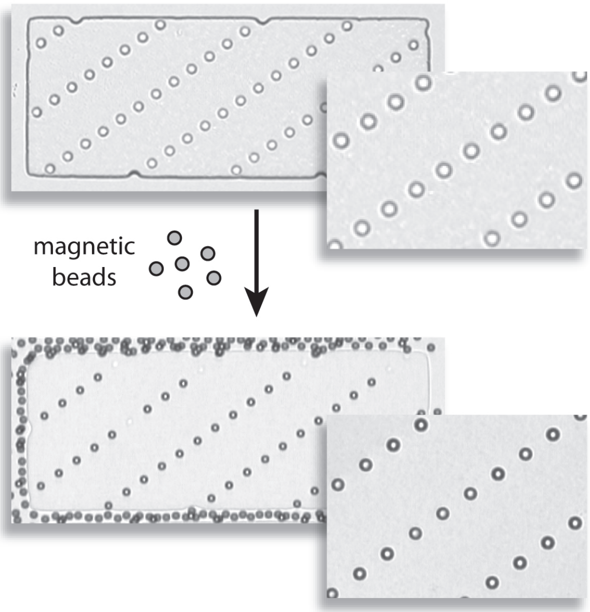

Fig. 8.1: *Precise patterning of beads in photopolymerized PEG microwells. PEG structures (*100 × 200 *µm) with lines of* ∼ 5 *µm microwells were polymerized on a glass surface. Magnetic beads (4.5 µm) were deposited on the structures, filling most of the microwells.*

parallel to the channel, capturing target cells on the beads protein-decorated surfaces. This process is shown schematically in Figure 8.2a.

In collaboration with Ramin Haghgooie of the Doyle Lab, we developed mathematical models to predicst when columns would properly guide across the patterned rails, when they would get stuck on the rails, or when they would flow past rails. We performed simulations to support the model, developing a phase diagram to predict the various guiding regimes over a broad parameter space (Figure 8.2b). The model development and simulations are described in great detail in Dr. Haghgooie's Doctoral Thesis [172].

Although simulations of this approach look very promising, the system has never been tested experimentally beyond proof-of-principle guiding along magnetic rails (data not shown). With the methods developed in this thesis now in place, the experimental demonstration could be readily realized. Specifically, the rail system used in this approach could be fairly easily synthesized using bead-patterned hydrogels. In addition, the columns used in the system could be made using flow-lithography.

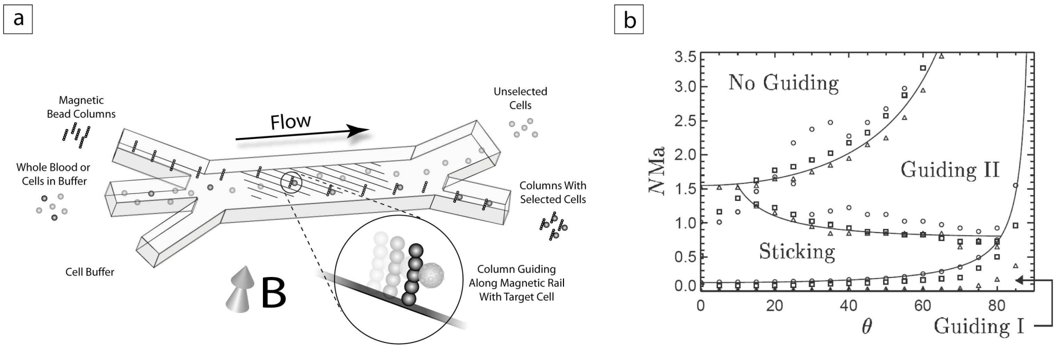

Fig. 8.2: *Pattern-assisted magnetic cell sorting. (a) Schematic of sorting method where columns of magnetic beads enter a channel, are directed laterally across a stream of mixed cells, where they capture cells of interest, and into a clean buffer stream where are harvested. (b) Phase diagram for predicting "guiding" and "non-guiding" regimes for column steering using the Mason Number (Ma), number of beads per column (N) and pattern angle (θ). For more details see Reference [172].*

8.3 Armored Droplets and Cell Encapsulation

As shown in Chapter 4, we have the ability to dynamically detect and capture entities using computer-aided flow lithography in a microfluidic device. Although in this work, we only showed the utility of this process for confining droplets in two-dimensional cages, it is possible to make only slight modifications to the system in order to cage and array single cells, or completely encapsulate droplets or cells. Furthermore, it is possible to use a dynamic mask to give each cage a unique "barcode." In this fashion, the single cells can be arrayed, probed with stimuli, analyzed for dynamic response, and subsequently sorted for further analysis or harvesting. Cages could also be loaded with probes in order to directly assay the cells they contain. This approach may provide a versatile, high-throughput method for single-cell analysis.

8.4 Particle Scanning Technologies

The prospect of using encoded hydrogel particles for multiplexed analysis is extremely attractive as it can potentially provide high-performance with very low cost. However, in order for this method to be truly high-throughput, a more advanced method for particle scanning needs to be developed. In Chapter 5, we demonstrated flow-through scanning of particles in a microfluidic device (Figure 5.4). However, with a limited detection rate provided by the particular CCD camera used, we were unable to test the achievable speeds at which particles could be accurately scanned.

With a new 1D-encoding scheme in place (Figure 6.1), we are now better suited to develop a high-throughput scanning system. In collaboration with Stephen Chapin, another graduate student of the Doyle Lab, we have performed high-speed analysis of particles passing through a flow-focusing microfluidic device. Sample time-sequence images taken using a high-speed camera (at up to 4,000 frames/sec) are shown in Figure 8.3.

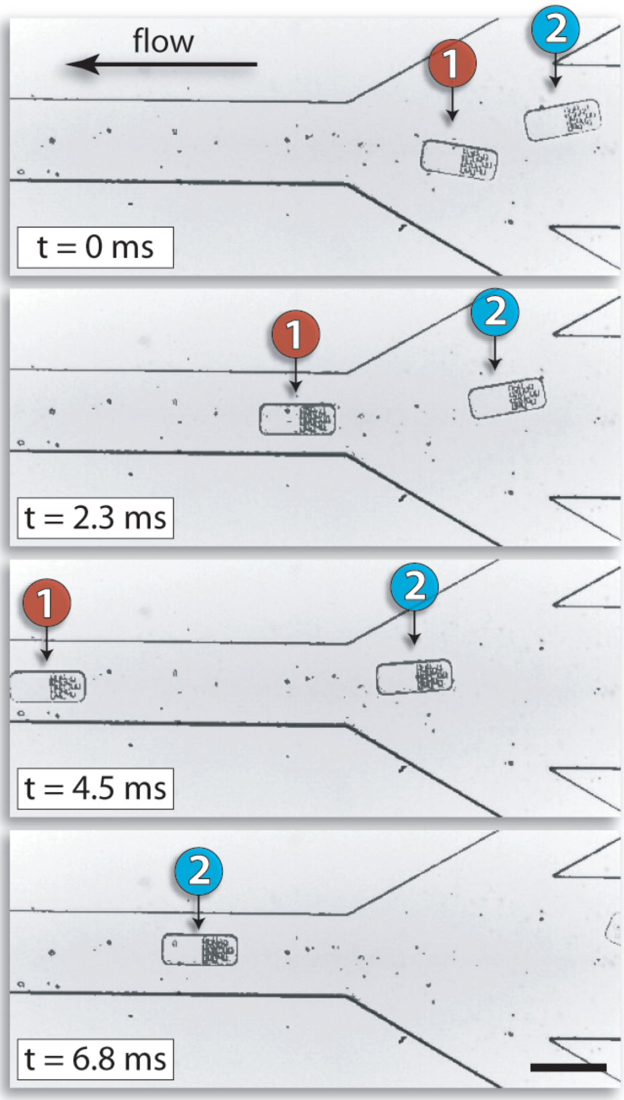

Fig. 8.3: *High speed particle alignment in a flow-focusing device. Time-lapse brightfield images, taken with a high-speed camera, show particles (225 × 90 × 25 µm) entering the focusing region of a microfluidic channel (35um-tall), where they are aligned by side-channel sheath flows in preparation for scanning. The particles were traveling at a velocity of 0.3 m/s with no incidents of clogging in any of the preliminary experiments. Scalebar is* 250 *µm.*

In this experiment, we passed hundreds of particles through a device at velocities of ~ 0.3 m/s. Importantly, there was not a single clogging event and no noticeable particle deformation. This experiment suggests that scan rates on the order of 100s of particles per second are feasible, which would make our system capable for high-throughput applications.

In order to realize this goal, it is imperative that several aspects of the system be optimized. Some of these include particle and barcode design, particle composition, channel geometry, and detection optics. Ideally, a system could be engineered that would enable scanning of hundreds of particles per second, accurate particle decoding and sensitive target detection, minimal particle breakage, and no device clogging.

8.5 Development of a Generic Scheme for Probe Attachment

Although the direct incorporation of probes is attractive for many applications, it may be more desirable to have a "generic" coupling scheme in others. For instance, if there is an application where target sets are rapidly changing, instead of synthesizing many new particle types, it would be possible to react pre-synthesized particles with new probes. This can be done very rapidly, and in a multiplexed manner (ie. 96-well plates).

We investigated using such a "generic" reaction chemistry. For simplicity, we chose to incorporate acrylic acid into particles – these monomers present carboxyl groups that can subsequently reacted with amine-modified DNA probes, which are readily available. As shown in Figure 8.4, we were able to demonstrate the feasibility of this approach. In our experiment, we synthesized particles with varying monomer mixtures, containing a total concentration of 20% active species (PEG_{700} or acrylic acid), 40% $PEG_2 00$, 35% 3× TE, and 5% Darocur 1173. To investigate the effect of acrylic acid concentration, this component was varied from 0 – 5%.

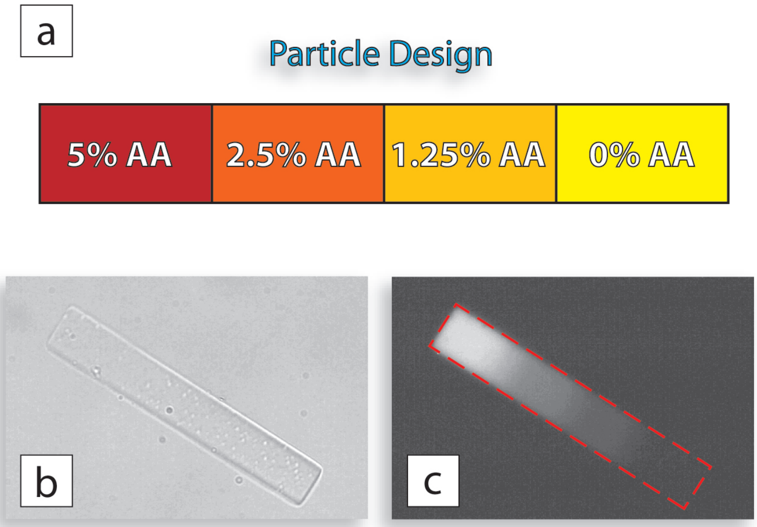

Fig. 8.4: *Generic coupling scheme using amino acid-loaded particles with amino-modified DNA probes. (a) Particles were synthesized using monomer blends of* $PEG\text{-}DA_{700}$ *and acrylic acid, and reacted with amino-modified DNA probe. After probe conjugation, the particles were incubated with a fluorescent target to assess incorporation. Shown are DIC (b) and fluorecence (c) images of a particle after probe conjugation and target hybridization.*

After synthesis, particles were conjugated with probe by simply mixing particles with EDC (1-Ethyl-3-[3-dimethylaminopropyl]carbodiimide hydrochloride, at 5 mg/ml) in PBS buffer (pH = 7.2), and incubating at room temperature for 45 minutes. This protocol was by no means optimized, but was sufficient to show that probe was incorporated with particles, at levels that varied with the amount of acrylic acid incorporated (Figure 8.4c).

As seen in Figure 8.4, we were able to successfully incorporate probe using a generic scheme, at levels that varied with acrylic acid concentration. Beyond proof-of-concept, this and other methods for incorporating generic reaction chemistries in particles should be investigated. The chemistries should be designed for simplicity, but more importantly, performance. Each scheme should be tested for specificity and sensitivity (as done in Chapter 7) to ensure that the high-quality of hydrogel-particle based assays is preserved.

Bibliography

[1] Sun, K., Yamaguchi, A., Ishida, Y., Matsuo, S., and Misawa, H., "A heater-integrated transparent microchannel chip for continuous-flow PCR," *Sensors And Actuators B-Chemical* **84**(2-3), 283–289 (2002).

[2] El-Ali, J., Perch-Nielsen, I. R., Poulsen, C. R., Bang, D. D., Telleman, P., and Wolff, A., "Simulation and experimental validation of a SU-8 based PCR thermocycler chip with integrated heaters and temperature sensor," *Sensors And Actuators A-Physical* **110**(1-3), 3–10 (2004).

[3] Rodriguez, I., Lesaicherre, M., Tie, Y., Zou, Q. B., Yu, C., Singh, J., Meng, L. T., Uppili, S., Li, S. F. Y., Gopalakrishnakone, P., and Selvanayagam, Z. E., "Practical integration of polymerase chain reaction amplification and electrophoretic analysis in microfluidic devices for genetic analysis," *Electrophoresis* **24**(1-2), 172–178 (2003).

[4] Doyle, P. S., Bibette, J., Bancaud, A., and Viovy, J. L., "Self-assembled magnetic matrices for DNA separation chips," *Science* **295**(5563), 2237–2237 (2002).

[5] Cheng, S. B., Skinner, C. D., Taylor, J., Attiya, S., Lee, W. E., Picelli, G., and Harrison, D. J., "Development of a multichannel microfluidic analysis system employing affinity capillary electrophoresis for immunoassay," *Analytical Chemistry* **73**(7), 1472–1479 (2001).

[6] Macounova, K., Cabrera, C. R., and Yager, P., "Concentration and separation of proteins in microfluidic channels on the basis of transverse IEF," *Analytical Chemistry* **73**(7), 1627–1633 (2001).

[7] Wang, X. B., Yang, J., Huang, Y., Vykoukal, J., Becker, F. F., and Gascoyne, P. R. C., "Cell separation by dielectrophoretic field-flow-fractionation," *Analytical Chemistry* **72**(4), 832–839 (2000).

[8] Muller, T., Schnelle, T., Gradl, G., Shirley, S. G., and Fuhr, G., "Microdevice for cell and particle separation using dielectrophoretic field-flow fractionation," *Journal Of Liquid Chromatography and Related Technologies* **23**(1), 47–59 (2000).

[9] Fu, A. Y., Spence, C., Scherer, A., Arnold, F. H., and Quake, S. R., "A microfabricated fluorescence-activated cell sorter," *Nature Biotechnology* **17**(11), 1109–1111 (1999).

[10] Kruger, J., Singh, K., O'Neill, A., Jackson, C., Morrison, A., and O'Brien, P., "Development of a microfluidic device for fluorescence activated cell sorting," *Journal Of Micromechanics And Microengineering* **12**(4), 486–494 (2002).

[11] Inglis, D. W., Riehn, R., Austin, R. H., and Sturm, J. C., "Continuous microfluidic immunomagnetic cell separation," *Appl. Phys. Lett.* **85**(21), 5093–95 (2004).

[12] Gu, W., Zhu, X. Y., Futai, N., Cho, B. S., and Takayama, S., "Computerized microfluidic cell culture using elastomeric channels and braille displays," *Proceedings Of The National Academy Of Sciences Of The United States Of America* **101**(45), 15861–15866 (2004).

[13] Hung, P. J., Lee, P. J., Sabounchi, P., Lin, R., and Lee, L. P., "Continuous perfusion microfluidic cell culture array for high-throughput cell-based assays," *Biotechnology And Bioengineering* **89**(1), 1–8 (2005).

[14] Chiem, N. H. and Harrison, D. J., "Microchip systems for immunoassay: an integrated immunoreactor with electrophoretic separation for serum theophylline determination," *Clinical Chemistry* **44**(3), 591–598 (1998).

[15] Hatch, A., Kamholz, A. E., Hawkins, K. R., Munson, M. S., Schilling, E. A., Weigl, B. H., and Yager, P., "A rapid diffusion immunoassay in a T-sensor," *Nature Biotechnology* **19**(5), 461–465 (2001).

[16] von Lode, P., "Point-of-care immunotesting: Approaching the analytical performance of central laboratory methods," *Clinical Biochemistry* **38**(7), 591–606 (2005).

[17] Gascoyne, P., Satayavivad, J., and Ruchirawat, M., "Microfluidic approaches to malaria detection," *Acta Tropica* **89**(3), 357–369 (2004).

[18] Monaghan, P. B., McCarney, K. M., Ricketts, A., Littleford, R. E., Docherty, F., Smith, W. E., Graham, D., and Cooper, J. M., "Bead-based DNA diagnostic assay for chlamydia using nanoparticle-mediated surface-enhanced resonance raman scattering detection within a lab-on-a-chip format," *Analytical Chemistry* **79**(7), 2844–2849 (2007).

[19] Wang, C. H. and Lee, G. B., "Automatic bio-sampling chips integrated with micro-pumps and micro-valves for disease detection," *Biosensors and Bioelectronics* **21**(3), 419–425 (2005).

[20] Cheng, X. H., Irimia, D., Dixon, M., Sekine, K., Demirci, U., Zamir, L., Tompkins, R. G., Rodriguez, W., and Toner, M., "A microfluidic device for practical label-free CD4(+) T cell counting of HIV-infected subjects," *Lab On A Chip* **7**(2), 170–178 (2007).

[21] Yager, P., Edwards, T., Fu, E., Helton, K., Nelson, K., Tam, M. R., and Weigl, B. H., "Microfluidic diagnostic technologies for global public health," *Nature* **442**(7101), 412–418 (2006).

[22] Murray, H. W., Rubin, B. Y., Masur, H., and Roberts, R. B., "Impaired production of lymphokines and immune (gamma) interferon in the acquired immunodeficiency syndrome," *New England Journal Of Medicine* **310**(14), 883–889 (1984).

[23] Catalona, W. J., Smith, D. S., Ratliff, T. L., Dodds, K. M., Coplen, D. E., Yuan, J. J. J., Petros, J. A., and Andriole, G. L., "Measurement of prostate-specific antigen in serum as a screening-test for prostate-cancer," *New England Journal Of Medicine* **324**(17), 1156–1161 (1991).

[24] Zielenski, J., Rozmahel, R., Bozon, D., Kerem, B. S., Grzelczak, Z., Riordan, J. R., Rommens, J., and Tsui, L. C., "Genomic DNA-sequence of the cystic-fibrosis transmembrane conductance regulator (Cftr) gene," *Genomics* **10**(1), 214–228 (1991).

[25] Schumm, M., Lang, P., Taylor, G., Kuci, S., Klingebiel, T., Buhring, H. J., Geiselhart, A., Niethammer, D., and Handgretinger, R., "Isolation of highly purified autologous and allogeneic peripheral cd34+ cells using the clinimacs device," *J. Hematother.* **8**(2), 209–218 (1999).

[26] Partington, K. M., Jenkinson, E. J., and Anderson, G., "A novel method of cell separation based on dual parameter immunomagnetic cell selection," *J. Immunol. Methods.* **223**(2), 195–205 (1999).

[27] Hoerstrup, S. P., Zund, G., Schoeberlein, A., Ye, Q., Vogt, P. R., and Turina, M. I., "Fluorescence activated cell sorting: a reliable method in tissue engineering of a bioprosthetic heart valve," *Ann. Thorac. Surg.* **66**(5), 1653–1657 (1998).

[28] Klucher, K. M., Gerlach, M. J., and Daley, G. Q., "A novel method to isolate cells with conditional gene expression using fluorescence activated cell sorting," *Nucleic. Acids Res.* **25**(23), 4858–4860 (1997).

[29] Frangioni, J. V. and Hajjar, R. J., "In vivo tracking of stem cells for clinical trials in cardiovascular disease," *Circulation* **110**(21), 3378–83 (2004).

[30] Breckpot, K., Heirman, C., Neyns, B., and Thielemans, K., "Exploiting dendritic cells for cancer immunotherapy: genetic modification of dendritic cells," *J. Gene. Med.* **6**(11), 1175–1188 (2004).

[31] Dullaers, M., Breckpot, K., Meirvenne, S. V., Bonehill, A., Tuyaerts, S., Michiels, A., Straetman, L., Heirman, C., Greef, C. D., Bruggen, P. V. D., and Thielemans, K., "Side-by-side comparison of lentivirally transduced and MRNA-electroporated dendritic cells: implications for cancer immunotherapy protocols," *Mol. Ther.* **10**(4), 768–779 (2004).

[32] Tachdjian, G., Frydman, N., Audibert, F., Ray, P., Kerbrat, V., Ernault, P., Frydman, R., and Costa, J. M., "Clinical applications of fetal sex determination in maternal blood in a preimplantation genetic diagnosis centre," *Hum. Reprod.* **17**(8), 2183–2186 (2002).

[33] Chen, H., Griffin, D. K., Jestice, K., Hackett, G., Cooper, J., and Ferguson-Smith, M. A., "Evaluating the culture of fetal erythroblasts from maternal blood for non-invasive prenatal diagnosis," *Prenat. Diagn.* **18**(9), 883–892 (1998).

[34] Kotobuki, N., Hirose, M., Funaoka, H., and Ohgushi, H., "Enhancement of in vitro osteoblastic potential after selective sorting of osteoblasts with high alkaline phosphatase activity from human osteoblast-like cells," *Cell Transplantation* **13**(4), 377–383 (2004).

[35] de Gruijter, M., van Rijn, M. A., Verkerk, A., and Jongkind, J. F., "Isolation of human and porcine monocytes and lymphocytes by three parameter flow sorting," *Zentralbl Veterinarmed A* **37**(8), 585–591 (1990).

[36] Cotter, M. J., Norman, K. E., Hellewell, P. G., and Ridger, V. C., "A novel method for isolation of neutrophils from murine blood using negative immunomagnetic separation," *Am. J. Pathol.* **159**(2), 473–481 (2001).

[37] de Wildt, R. M., Steenbakkers, P. G., Pennings, A. H., van den Hoogen, F. H., van Venrooij, W. J., and Hoet, R. M., "A new method for the analysis and production of monoclonal antibody fragments originating from single human B cells," *J. Immunol. Methods* **207**(1), 61–67 (1997).

[38] Leyendeckers, H., Odendahl, M., Lohndorf, A., Irsch, J., Spangfort, M., Miltenyi, S., Hunzelmann, N., Assenmacher, M., Radbruch, A., and Schmitz, J., "Correlation analysis between frequencies of circulating antigen-specific IgG-bearing memory B cells and serum titers of antigen-specific IgG," *European Journal of Immunology* **29**(4), 1406–1417 (1999).

[39] Townsend, S. E., Goodnow, C. C., and Cornall, R. J., "Single epitope multiple staining to detect ultralow frequency B cells," *J. Immunol. Methods.* **249**(38354), 137–146 (2001).

[40] Ash, R. C., Casper, J. T., Chitambar, C. R., Hansen, R., Bunin, N., Truitt, R. L., Lawton, C., Murray, K., Hunter, J., Baxterlowe, L. A., Gottschall, J. L., Oldham, K., Anderson, T., Camitta, B., and Menitove, J., "Successful allogeneic transplantation of t-cell depleted bone-marrow from closely hla-matched unrelated donors," *New England Journal of Medicine* **322**(8), 485–494 (1990).

[41] Kernan, N. A., Bartsch, G., Ash, R. C., Beatty, P. G., Champlin, R., Filipovich, A., Gajewski, J., Hansen, J. A., Hensleedowney, J., Mccullough, J., Mcglave, P., Perkins, H. A., Phillips, G. L., Sanders, J., Stroncek, D., Thomas, E. D., and Blume, K. G., "Analysis of 462 transplantations from unrelated donors facilitated by the national-marrow-donor-program," *New England Journal of Medicine* **328**(9), 593–602 (1993).

[42] Lamb, J., Crawford, E. D., Peck, D., Modell, J. W., Blat, I. C., Wrobel, M. J., Lerner, J., Brunet, J. P., Subramanian, A., Ross, K. N., Reich, M., Hieronymus, H., Wei, G., Armstrong, S. A., Haggarty, S. J., Clemons, P. A., Wei, R., Carr, S. A., Lander, E. S., and Golub, T. R., "The connectivity map: Using gene-expression signatures to connect small molecules, genes, and disease," *Science* **313**(5795), 1929–1935 (2006).

[43] Segal, E., Friedman, N., Koller, D., and Regev, A., "A module map showing conditional activity of expression modules in cancer," *Nature Genetics* **36**(10), 1090–1098 (2004).

[44] Chiu, D. T., Jeon, N. L., Huang, S., Kane, R. S., Wargo, C. J., Choi, T. S., Ingber, D. E., and Whitesides, G. M., "Patterned deposition of cells and proteins onto surfaces by using three-dimensional microfluidic systems," *Proc. Natl. Acad. Sci. USA* **97**(6), 2408–13 (2000).

[45] Dillmore, W. S., Yousaf, M. N., and Mrksich, M., "A photochemical method for patterning the immobilization of ligands and cells to self-assembled monolayers," *Langmuir* **20**(17), 7223–31 (2004).

[46] Christman, K. L. and Maynard, H. D., "Protein micropatterns using a ph-responsive polymer and light," *Langmuir* **21**(18), 8389–93 (2005).

[47] Kim, H., Doh, J., Irvine, D. J., Cohen, R. E., and Hammond, P. E., "Large area two-dimensional b cell arrays for sensing and cell-sorting applications," *Biomacromolecules* **5**(3), 822–7 (2004).

[48] Khademhosseini, A., Suh, K. Y., Jon, S., Eng, G., Yeh, J., Chen, G. J., and Langer, R., "A soft lithographic approach to fabricate patterned microfluidic channels," *Anal. Chem.* **76**(13), 3675–81 (2004).

[49] Lahann, J., Balcells, M., Rodon, T., Lee, J., Choi, I. S., Jensen, K. F., and Langer, R., "Reactive polymer coatings: A platform for patterning proteins and mammalian cells onto a broad range of materials," *Langmuir* **18**(9), 2117–22 (2002).

[50] Gleason, N. J., Nodes, C. J., Higham, E. M., Guckert, N., Aksay, I. A., Schwarzbauer, J. E., and Carbeck, J. D., "Patterning proteins and cells using two-dimensional arrays of colloids," *Langmuir* **19**(3), 513–8 (2003).

[51] Zheng, H. P., Berg, M. C., Rubner, M. F., and Hammond, P. T., "Controlling cell attachment selectively onto biological polymer-colloid templates using polymer-on-polymer stamping," *Langmuir* **20**(17), 7215–22 (2004).

[52] Chen, K. M., Jiang, X. P., Kimerling, L. C., and Hammond, P. T., "Selective self-organization of colloids on patterned polyelectrolyte templates," *Langmuir* **16**(20), 7825–34 (2000).

[53] Aizenberg, J., Braun, P. V., and Wiltzius, P., "Patterned colloidal deposition controlled by electrostatic and capillary forces," *Phys. Rev. Lett.* **84**(13), 2997–3000 (2000).

[54] Mio, C. and Marr, D. W. M., "Tailored surfaces using optically manipulated colloidal particles," *Langmuir* **15**(25), 8565–68 (1999).

[55] Won, J., Inaba, T., Masuhara, H., Fujiwara, H., Sasaki, K., Miyawaki, S., and Sato, S., "Photothermal fixation of laser-trapped polymer microparticles on polymer substrates," *Appl. Phys. Lett.* **75**(11), 1506–08 (1999).

[56] Hoogenboom, J. P., Vossen, D. L. J., Faivre-Moskalenko, C., Dogterom, M., and van Blaaderen, A., "Patterning surfaces with colloidal particles using optical tweezers," *Appl. Phys. Lett.* **80**(25), 4828–30 (2002).

[57] Suzuki, M., Yasukawa, T., Mase, Y., Oyamatsu, D., Shiku, H., and Matsue, T., "Dielectrophoretic micropatterning with microparticle monolayers covalently linked to glass surfaces," *Langmuir* **20**(25), 11005–11 (2004).

[58] Fan, F. Q. and Stebe, K. J., "Assembly of colloidal particles by evaporation on surfaces with patterned hydrophobicity," *Langmuir* **20**(8), 3062–67 (2004).

[59] Fustin, C. A., Glasser, G., Spiess, H. W., and Jonas, U., "Parameters influencing the templated growth of colloidal crystals on chemically patterned surfaces," *Langmuir* **20**(21), 9114–23 (2004).

[60] Jonas, U., del Campo, A., Kruger, C., Glasser, G., and Boos, D., "Colloid assemblies on patterned silane layers," *Proc. Natl. Acad. Sci. USA* **99**(8), 5034–9 (2002).

[61] Yin, Y. D., Lu, Y., Gates, B., and Xia, Y. N., "Template-assisted self-assembly: A practical route to complex aggregates of monodispersed colloids with well-defined sizes, shapes, and structures," *J. Am. Chem. Soc.* **123**(36), 8718–29 (2001).

[62] Schaak, R. E., Cable, R. E., Leonard, B. M., and Norris, B. C., "Colloidal crystal microarrays and two-dimensional superstructures: A versatile approach for patterned surface assembly," *Langmuir* **20**(17), 7293–97 (2004).

[63] Miyazaki, H. T., Miyazaki, H., Ohtaka, K., and Sato, T., "Photonic band in two-dimensional lattices of micrometer-sized spheres mechanically arranged under a scanning electron microscope," *J. Appl. Phys.* **87**(10), 7152–58 (2000).

[64] Furdui, V. I. and Harrison, D. J., "Immunomagnetic t cell capture from blood for PCR analysis using microfluidic systems," *Lab Chip* **4**(6), 614–8 (2004).

[65] Kim, K. S. and Park, J. K., "Magnetic force-based multiplexed immunoassay using superparamagnetic nanoparticles in microfluidic channel," *Lab Chip* **5**(6), 657–64 (2005).

[66] Roos, P. and Skinner, C. D., "A two bead immunoassay in a micro fluidic device using a flat laser intensity profile for illumination," *Analyst* **128**(6), 527–31 (2003).

[67] Choi, J. W., Oh, K. W., Thomas, J. H., Heineman, W. R., Halsall, H. B., Nevin, J. H., Helmicki, A. J., Henderson, H. T., and Ahn, C. H., "An integrated microfluidic biochemical detection system for protein analysis with magnetic bead-based sampling capabilities," *Lab Chip* **2**(1), 27–30 (2002).

[68] Fan, Z. H., Mangru, S., Granzow, R., Heaney, P., Ho, W., Dong, Q. P., and Kumar, R., "Dynamic DNA hybridization on a chip using paramagnetic beads," *Anal. Chem.* **71**(21), 4851–9 (1999).

[69] Ali, M. F., Kirby, R., Goodey, A. P., Rodriguez, M. D., Ellington, A. D., Neikirk, D. P., and McDevitt, J. T., "DNA hybridization and discrimination of single-nucleotide mismatches using chip-based microbead arrays," *Anal. Chem.* **75**(18), 4732–9 (2003).

[70] Deng, T., Prentiss, M., and Whitesides, G. M., "Fabrication of magnetic microfiltration systems using soft lithography," *Appl. Phys. Lett.* **80**(3), 461–3 (2002).

[71] Campbell, C. J. and Grzybowski, B. A., "Microfluidic mixers: from microfabricated to self-assembling devices," *Philos. Transact. A Math. Phys. Eng. Sci.* **362**(1818), 1069–86 (2004).

[72] Lyles, B. F., Terrot, M. S., Hammond, P. T., and Gast, A. P., "Directed patterned adsorption of magnetic beads on polyelectrolyte multilayers on glass," *Langmuir* **20**(8), 3028–31 (2004).

[73] Schena, M., Shalon, D., Davis, R. W., and Brown, P. O., "Quantitative monitoring of gene-expression patterns with a complementary-DNA microarray," *Science* **270**(5235), 467–470 (1995).

[74] Fodor, S. P., Rava, R. P., Huang, X. C., Pease, A. C., Holmes, C. P., and Adams, C. L., "Multiplexed biochemical assays with biological chips," *Nature* **364**(6437), 555–556 (1993).

[75] Gershon, D., "Microarray technology: an array of opportunities," *Nature* **416**(6883), 885–891 (2002).

[76] Nolan, J. P. and Sklar, L. A. *Trends Biotechnol.* **20**, 9 (2002).

[77] Fan, J. B., Chee, M. S., and Gunderson, K. L., "Highly parallel genomic assays," *Nat. Rev. Genet.* **7**(8), 632–644 (2006).

[78] Fulton, R. J., McDade, R. L., Smith, P. L., Kienker, L. J., and Jr., J. R. K., "Advanced multiplexed analysis with the flowmetrix system," *Clin Chem.* **43**(9), 1749–1756 (1997).

[79] Battersby, B. J., Bryant, D., Meutermans, W., Matthews, D., Smythe, M. L., and Trau, M., "Toward larger chemical libraries: Encoding with fluorescent colloids in combinatorial chemistry," *J. Am. Chem. Soc.* **122**(9), 2138–2139 (2000).

[80] Xu, H., Sha, M. Y., Wong, E. Y., Uphoff, J., Xu, Y., Treadway, J. A., Truong, A., O'Brien, E., Asquith, S., Stubbins, M., Spurr, N. K., Lai, E. H., and Mahoney, W., "Multiplexed SNP genotyping using the qbead system: a quantum dot-encoded microsphere-based assay," *Nucleic Acids Res.* **31**(8), e43 (2003).

[81] Han, M., Gao, X., Su, J. Z., and Nie, S., "Quantum-dot-tagged microbeads for multiplexed optical coding of biomolecules," *Nat. Biotechnol.* **19**(7), 631–635 (2001).

[82] Zhao, X. W., Liu, Z. B., Yang, H., Nagai, K., Zhao, Y. H., and Gu, Z. Z., "Uniformly colorized beads for multiplexed immunoassay," *Chem. Mater.* **18**(9), 2443–2449 (2006).

[83] Cunin, F., Schmedake, T. A., Link, J. R., Li, Y. Y., Koh, J., Bhatia, S. N., and Sailor, M. J., "Biomolecular screening with encoded porous-silicon photonic crystals," *Nat. Mater.* **1**(1), 39–41 (2002).

[84] Su, X., Zhang, J., Sun, L., Koo, T. W., Chan, S., Sundararajan, N., Yamakawa, M., and Berlin, A. A., "Composite organic-inorganic nanoparticles (coins) with chemically encoded optical signatures," *Nano Lett.* **5**(1), 48–54 (2005).

[85] Fenniri, H., Chun, S., Ding, L., Zyrianov, Y., and Hallenga, K., "Preparation, physical properties, on-bead binding assay and spectroscopic reliability of 25 barcoded polystyrene-poly(ethylene glycol) graft copolymers," *J. Am. Chem. Soc.* **125**(35), 10546–10560 (2003).

[86] Nicewarner-Pena, S. R., Freeman, R. G., Reiss, B. D., He, L., Pena, D. J., Walton, I. D., Cromer, R., Keating, C. D., and Natan, M. J., "Submicrometer metallic barcodes," *Science* **294**(5540), 137–141 (2001).

[87] Sha, M. Y., Walton, I. D., Norton, S. M., Taylor, M., Yamanaka, M., Natan, M. J., Xu, C., Drmanac, S., Huang, S., Borcherding, A., Drmanac, R., and Penn, S. G., "Multiplexed SNP genotyping using nanobarcode particle technology," *Anal. Bioanal. Chem.* **384**(3), 658–666 (2006).

[88] Evans, M., Sewter, C., and Hill, E., "An encoded particle array tool for multiplex bioassays," *Assay Drug Dev. Technol.* **1**(1), 1999–2207 (2003).

[89] Zhi, Z. L., Morita, Y., Hasan, Q., and Tamiya, E., "Micromachining microcarrier-based biomolecular encoding for miniaturized and multiplexed immunoassay," *Anal. Chem.* **75**(16), 4125–4131 (2003).

[90] Braeckmans, K., Smedt, S. C. D., Roelant, C., Leblans, M., Pauwels, R., and Demeester, J., "Encoding microcarriers by spatial selective photobleaching," *Nat. Mater.* **2**(3), 169–173 (2003).

[91] Moran, E. J., Sarshar, S., Cargill, J. F., Shahbaz, M. M., Lio, A., Mjalli, A. M. M., and Armstrong, R. W., "Radio-frequency tag encoded combinatorial library method for the discovery of tripeptide-substituted cinnamic acid inhibitors of the protein-tyrosine-phosphatase ptp1b," *J. Am. Chem. Soc.* **117**(43), 10787–10788 (1995).

[92] Nicolaou, K. C., Xiao, X. Y., Parandoosh, Z., Senyei, A., and Nova, M. P., "Radiofrequency encoded combinatorial chemistry," *Angew. Chem. Int. Edn.* **34**(20), 2289–2291 (1995).

[93] Service, R. F., "Radio tags speed compound synthesis," *Science* **270**(5236), 577 (1995).

[94] Xiao XY, Li RS, Z. H. E. B. K. K. L. J. B. R. N. K., "Solid-phase combinatorial synthesis using microkan reactors, Rf tagging, and directed sorting," *Biotech. Bioeng.* **71**(1), 44–50 (2000).

[95] McHugh, T. M., Miner, R. C., Logan, L. H., and Stites, D. P., "Simultaneous detection of antibodies to cytomegalovirus and herpes simplex virus by using flow cytometry and a microsphere-based fluorescence immunoassay," *J. Clin. Microbiol.* **26**(10), 1957–1961 (1988).

[96] Vaino, A. R. and Janda, K. D., "Euclidean shape-encoded combinatorial chemical libraries," *Proc. Natl. Acad. Sci. U. S. A.* **97**(14), 7692–7696 (2000).

[97] Ferguson, J. A., Steemers, F. J., and Walt, D. R., "High-density fiber-optic DNA random microsphere array," *Anal. Chem.* **72**(22), 5618–5624 (2000).

[98] Finkel, N. H., Lou, X., Wang, C., and He, L., "Barcoding the microworld," *Anal. Chem.* **76**(19), 352A–359A (2004).

[99] Braeckmans, K., Smedt, S. C. D., Leblans, M., Pauwels, R., and Demeester, J., "Encoding microcarriers: present and future technologies," *Nat. Rev. Drug Discov.* **1**(6), 447–456 (2002).

[100] Lu, Y., Yin, Y., and Xia, Y., "Three-dimensional photonic crystals with non-spherical colloids as building blocks," *Adv. Mater.* **13**(6), 415–420 (2001).

[101] Beebe, D. J., Moore, J. S., Bauer, J. M., Yu, Q., Liu, R. H., Devadoss, C., and Jo, B.-H., "Functional hydrogel structures for autonomous flow control inside microfluidic channels," *Nature* **404**, 588–590 (2000).

[102] Langer, R. and Tirrell, D. A., "Designing materials for biology and medicine," *Nature* **428**, 487–492 (2004).

[103] Glotzer, S. C., "Some assembly required," *Science* **306**, 419–420 (2004).

[104] Hernandez, C. J. and Mason, T. G., "Colloidal alphabet soup: Monodisperse dispersions of shape-designed lithoparticles," *Journal of Physical Chemistry C* **111**(12), 4477–4480 (2007).

[105] Rolland, J. P., Maynor, B. W., Euliss, L. E., Exner, A. E., Denison, G. M., and DeSimone, J. M., "Direct fabrication and harvesting of monodisperse, shape-specific nanobiomaterials," *Journal of the American Chemical Society* **127**(28), 10096–10100 (2005).

[106] Sugiura, S., Nakajima, M., Tong, J., Nabetani, H., and Seki, M., "Preparation of monodispersed solid lipid microspheres using a microchannel emulsification technique," *J. Colloid Interface Sci.* **227**, 95–103 (2000).

[107] Nisisako, T., Torii, T., and Higuchi, T., "Novel microreactors for functional polymer beads," *Chem. Eng. J.* **101**, 23–29 (2004).

[108] Dendukuri, D., Tsoi, K., Hatton, T. A., and Doyle, P. S., "Controlled synthesis of nonspherical microparticles using microfluidics," *Langmuir* **21**, 2113–2116 (2005).

[109] Xu, S., Nie, Z., Seo, M., Lewis, P., Kumacheva, E., Stone, H. A., Garstecki, P., Weibel, D. B., Gitlin, I., and Whitesides, G. M., "Generation of monodisperse particles by using microfluidics: control over size, shape and composition," *Angew. Chem. Int. Ed.* **44**, 724–728 (2005).

[110] Jeong, W., Kim, J., Kim, S., Lee, S., Mensing, G., and Beebe, D. J., "Hydrodynamic microfabrication *via* "on the fly" photopolymerization of microscale fibers and tubes," *Lab Chip* **4**, 576–580 (2004).

[111] Wark, A. W., Lee, H. J., and Corn, R. M., "Multiplexed detection methods for profiling microRNA expression in biological samples," *Angewandte Chemie-International Edition* **47**(4), 644–652 (2008).

[112] Levicky, R. and Horgan, A., "Physicochemical perspectives on dna microarray and biosensor technologies," *Trends in Biotechnology* **23**(3), 143–149 (2005).

[113] Castoldi, M., Schmidt, S., Benes, V., Noerholm, M., Kulozik, A. E., Hentze, M. W., and Muckenthaler, M. U., "A sensitive array for microRNA expression profiling (michip) based on locked nucleic acids (LNA)," *RNA-a Publication of the RNA Society* **12**(5), 913–920 (2006).

[114] Rubina, A. Y., Pan'kov, S. V., Dementieva, E. I., Pen'kov, D. N., Butygin, A. V., Vasiliskov, V. A., Chudinov, A. V., Mikheikin, A. L., Mikhailovich, V. M., and Mirzabekov, A. D., "Hydrogel drop microchips with immobilized dna: properties and methods for large-scale production," *Analytical Biochemistry* **325**(1), 92–106 (2004).

[115] Fotin, A. V., Drobyshev, A. L., Proudnikov, D. Y., Perov, A. N., and MIrzabekov, A. D., "Parallel thermodynamic analysis of duplexes on oligodeoxyribonucleotide microchips," *Nucleic Acids Research* **26**(6), 1515–1521 (1998).

[116] Sorokin, N. V., Chechetkin, V. R., Pan'kov, S. V., Somova, O. G., Livshits, M. A., Donnikov, M. Y., Turygin, A. Y., Barsky, V. E., and Zasedatelev, A. S., "Kinetics of hybridization on surface oligonucleotide microchips: Theory, experiment, and comparison with hybridization on gel-based microchips," *Journal of Biomolecular Structure and Dynamics* **24**(1), 57–66 (2006).

[117] Beebe, D. J., Moore, J. S., Bauer, J. M., Yu, Q., Liu, R. H., Devadoss, C., and Jo, B. H., "Functional hydrogel structures for autonomous flow control inside microfluidic channels," *Nature* **404**(6778), 588–90 (2000).

[118] Folch, A., Jo, B. H., Hurtado, O., Beebe, D. J., and Toner, M., "Microfabricated elastomeric stencils for micropatterning cell cultures," *J Biomed. Mater. Res.* **52**(2), 346–53 (2000).

[119] Khademhosseini, A., Yeh, J., Jon, S., Eng, G., Suh, K. Y., Burdick, J. A., and Langer, R., "Molded polyethylene glycol microstructures for capturing cells within microfluidic channels," *Lab Chip* **4**(5), 425–430 (2004).

[120] Liu, V. A. and Bhatia, S. N., "Three-dimensional photopatterning of hydrogels containing living cells," *Biomed. Microdevices* **4**(4), 257–66 (2002).

[121] Pregibon, D. C., Toner, M., and Doyle, P. S., "Magnetically and biologically active bead-patterned hydrogels," *Langmuir* **22**(11), 5122–5128 (2006).

[122] Love, J. C., Wolfe, D. B., Jacobs, H. O., and Whitesides, G. M., "Microscope projection photolithography for rapid prototyping of masters with micron-scale features for use in soft lithography," *Langmuir* **17**(19), 6005–12 (2001).

[123] Decker, C. and Jenkins, A. D., "Kinetic approach of O_2 inhibition in ultraviolet-induced and laser-induced polymerizations," *Macromolecules* **18**(6), 1241–4 (1985).

[124] Dendukuri, D., Pregibon, D. C., Collins, J., Hatton, T. A., and Doyle, P. S., “Continuous-flow lithography for high-throughput microparticle synthesis,” *Nat. Mater.* **5**(5), 365–369 (2006).

[125] Prestrelski, S. J., Tedeschi, N., Arakawa, T., and Carpenter, J. F., “Dehydration-induced conformational transitions in proteins and their inhibition by stabilizers,” *Biophys. J.* **65**(2), 661–71 (1993).

[126] Thiel, A., Scheffold, A., and Radbruch, A., “Immunomagnetic cell sorting - pushing the limits,” *Immunotechnology* **4**(2), 89–96 (1998).

[127] Urban, D. and Takamura, K., eds., [*Polymer Dispersions and Their Industrial Applications*], Wiley-VCH, Weinheim, Germany (2002).

[128] Brown, A. B. D., Smith, C. G., and Rennie, A. R., “Fabricating colloidal particles with photolithography and their interactions at an air-water interface,” *Phys. Rev. E.* **62**, 951–960 (2000).

[129] Love, J. C., Wolfe, D. B., Jacobs, H. O., and Whitesides, G. M., “Microscope projection photolithograpy for rapid prototyping of masters with micron-scale features for use in soft lithography,” *Langmuir* **17**, 6005–6012 (2001).

[130] Rezvin, A., Russell, R. J., Yadavalli, V. K., Koh, W.-G., Deister, C., Hile, D. D., Mellott, M. B., and Pishko, M. V., “Fabrication of poly(ethylene glycol) hydrogel microstructures using photolithography,” *Langmuir* **17**, 5440–5447 (2001).

[131] Jiang, P., Bertone, J. F., and Colvin, V. L., “A lost-wax approach to monodisperse colloids and their crystals,” *Science* **291**, 453–457 (2001).

[132] Subramaniam, A. B., Abkarian, M., and Stone, H. A., “Controlled assembly of jammed colloidal shells on fluid droplets,” *Nature Mater.* **4**(7), 553–556 (2005).

[133] Dendukuri, D., Gu, S. S., Pregibon, D. C., Hatton, T. A., and Doyle, P. S., “Stop-flow lithography in a microfluidic device,” *Lab on a Chip* **7**(7), 818–828 (2007).

[134] Decker, C. and Jenkins, A. D., “Kinetic approach of O_2 inhibition in ultraviolet- and laser-induced polymerizations,” *Macromolecules* **18**, 1241–1244 (1985).

[135] Kim, S., Oh, H., Baek, J. Y., Kim, H., Kim, W., and Lee, S., “Hydrodynamic fabrication of polymeric barcoded strips as components for parallel bio-analysis and programmable microactuation,” *Lab Chip* **5**, 1168–1172 (2005).

[136] Roh, K.-H., Martin, D. C., and Lahann, J., “Biphasic janus particles with nanoscale anisotropy,” *Nature Mater.* **4**, 759–763 (2005).

[137] Fialkowski, M., Bitner, A., and Grzybowski, B. A., “Self-assembly of polymeric microspheres of complex internal structures,” *Nature Mater.* **4**, 93–97 (2005).

[138] Finkel, N. H., Lou, X., Wang, C., and He, L., “Barcoding the microworld,” *Anal. Chem.* **76**, 352A–359A (2004).

[139] Dendukuri, D., Hatton, T. A., and Doyle, P. S., "Synthesis and self-assembly of amphiphilic polymeric microparticles," *Langmuir* **23**(8), 4669–4674 (2007).

[140] Tawfik, D. S. and Griffiths, A. D., "Man-made cell-like compartments for molecular evolution," *Nat. Biotech.* **16**(7), 652–656 (1998).

[141] Shendure, J., Porreca, G. J., Reppas, N. B., Lin, X. X., McCutcheon, J. P., Rosenbaum, A. M., Wang, M. D., Zhang, K., Mitra, R. D., and Church, G. M., "Accurate multiplex polony sequencing of an evolved bacterial genome," *Science* **309**(5741), 1728–1732 (2005).

[142] Aharoni, A., Griffiths, A. D., and Tawfik, D. S., "High-throughput screens and selections of enzyme-encoding genes," *Curr. Opin. Chem. Bio.* **9**(2), 210–216 (2005).

[143] Srinivasan, V., Pamula, V. K., and Fair, R. B., "Droplet-based microfluidic lab-on-a-chip for glucose detection," *Anal. Chem. Acta* **507**(1), 145–150 (2004).

[144] Sugiura, S., Nakajima, M., and Seki, M., "Preparation of monodispersed polymeric microspheres over 50 mu m employing microchannel emulsification," *Industrial and Engineering Chemistry Research* **41**(16), 4043–4047 (2002).

[145] Anna, S. L., Bontoux, N., and Stone, H. A., "Formation of dispersions using "flow focusing" in microchannels," *App. Phys. Lett.* **82**(3), 364–366 (2003).

[146] Thorsen, T., Roberts, R. W., Arnold, F. H., and Quake, S. R., "Dynamic pattern formation in a vesicle-generating microfluidic device," *Phys. Rev. Lett.* **86**(18), 4163–4166 (2001).

[147] Baroud, C. N. and Willaime, H., "Multiphase flows in microfluidics," *Comptes Rendus Physique* **5**(5), 547–555 (2004).

[148] Oh, H. J., Kim, S. H., Baek, J. Y., Seong, G. H., and Lee, S. H., "Hydrodynamic micro-encapsulation of aqueous fluids and cells via 'on the fly' photopolymerization," *Journal of Micromechanics and Microengineering* **16**(2), 285–291 (2006).

[149] Pregibon, D. C., Toner, M., and Doyle, P. S., "Multifunctional encoded particles for high-throughput biomolecule analysis," *Science* **315**(5817), 1393–1396 (2007).

[150] Hergt, R., Andra, W., d'Ambly, C. G., Hilger, I., Kaiser, W. A., Richter, U., and Schmidt, H. G., "Physical limits of hyperthermia using magnetite fine particles," *IEEE Trans. Magn.* **34**(5), 3745–3754 (1998).

[151] Rubina, A. Y., Dementieva, E. I., Stomakhin, A. A., Darii, E. L., Pan'kov, S. V., Barsky, V. E., Ivanov, S. M., Konovalova, E. V., and Mirzabekov, A. D., "Hydrogel-based protein microchips: manufacturing, properties, and applications," *Biotechniques* **34**(5), 1008–1022 (2003).

[152] Vasiliskov, A. V., Timofeev, E. N., Surzhikov, S. A., Drobyshev, A. L., Shick, V. V., and Mirzabekov, A. D., "Fabrication of microarray of gel-immobilized compounds on a chip by copolymerization," *Biotechniques* **27**(3), 592–600 (1999).

[153] Rehman, F. N., Audeh, M., Abrams, E. S., Hammond, P. W., Kenney, M., and Boles, T. C., “Immobilization of acrylamide-modified oligonucleotides by co-polymerization,” *Nucleic Acids Res.* **27**(2), 649–655 (1999).

[154] Mellott, M. B., Searcy, K., and Pishko, M. V., “Release of protein from highly cross-linked hydrogels of poly(ethylene glycol) diacrylate fabricated by UV polymerization,” *Biomaterials* **22**(9), 929–941 (2001).

[155] Cruise, G. M., Scharp, D. S., and Hubbell, J. A., “Characterization of permeability and network structure of interfacially photopolymerized poly(ethylene glycol) diacrylate hydrogels,” *Biomaterials* **19**(14), 1287–1294 (1998).

[156] Kohara, Y., Noda, H., Okano, K., and Kambara, H., “DNA probes on beads arrayed in a capillary, ’bead-array’, exhibited high hybridization performance,” *Nucleic Acids Res.* **30**(16), e87 (2002).

[157] Simonnet, C. and Groisman, A., “High-throughput and high-resolution flow cytometry in molded microfluidic devices,” *Anal. Chem.* **78**(16), 5653–5663 (2006).

[158] de Jager, W. and Rijkers, G. T., “Solid-phase and bead-based cytokine immunoassay: A comparison,” *Methods* **38**(4), 294–303 (2006).

[159] Irizarry, R. A., Wu, Z., and Jaffee, H. A., “Comparison of affymetrix genechip expression measures,” *Bioinformatics* **22**(7), 789–794 (2006).

[160] Dunbar, S. A., Zee, C. A. V., Oliver, K. G., Karem, K. L., and Jacobson, J. W., “Quantitative, multiplexed detection of bacterial pathogens: DNA and protein applications of the Luminex LabMAP system,” *J. Microbiol. Methods* **53**(2), 245–252 (2003).

[161] Meagher, R. J., Won, J. I., McCormick, L. C., Nedelcu, S., Bertrand, M. M., Bertram, J. L., Drouin, G., Barron, A. E., and Slater, G. W., “End-labeled free-solution electrophoresis of dna,” *Electrophoresis* **26**(2), 331–350 (2005).

[162] Gao, Y., Wolf, L. K., and Georgiadis, R. M., “Secondary structure effects on dna hybridization kinetics: a solution versus surface comparison,” *Nucleic Acids Research* **34**(11), 3370–3377 (2006).

[163] Lu, J., Getz, G., Miska, E. A., Alvarez-Saavedra, E., Lamb, J., Peck, D., Sweet-Cordero, A., Ebet, B. L., Mak, R. H., Ferrando, A. A., Downing, J. R., Jacks, T., Horvitz, H. R., and Golub, T. R., “MicroRNA expression profiles classify human cancers,” *Nature* **435**(7043), 834–838 (2005).

[164] Liang, R. Q., Li, W., Li, Y., Tan, C. Y., Li, J. X., Jin, Y. X., and Ruan, K. C., “An oligonucleotide microarray for microrna expression analysis based on labeling rna with quantum dot and nanogold probe,” *Nucleic Acids Research* **33**(2), – (2005).

[165] Baskerville, S. and Bartel, D. P., “Microarray profiling of micrornas reveals frequent coexpression with neighboring mirnas and host genes,” *Rna-a Publication of the Rna Society* **11**(3), 241–247 (2005).

[166] Wang, H., Ach, R. A., and Curry, B., "Direct and sensitive mirna profiling from low-input total rna," *Rna-a Publication of the Rna Society* **13**(1), 151–159 (2007).

[167] Nelson, P. T., Baldwin, D. A., Oberholtzer, J. C., and Mourelatos, Z., "A microarray-based method for studying micro-rna (mirna) expression.," *Journal of Neuropathology and Experimental Neurology* **63**(5), 520–520 (2004).

[168] Fang, S. P., Lee, H. J., Wark, A. W., and Corn, R. M., "Attomole microarray detection of MicroRNAs by nanoparticle-amplified spr imaging measurements of surface polyadenylation reactions," *Journal of the American Chemical Society* **128**(43), 14044–14046 (2006).

[169] Peck, D., Crawford, E. D., Ross, K. N., Stegmaier, K., Golub, T. R., and Lamb, J., "A method for high-throughput gene expression signature analysis," *Genome Biology* **7**(7), – (2006).

[170] Deen, W. M., [*Transport Phenomena*], Oxford University Press, New York, USA (1998).

[171] Welty, J. R., [*Fundamentals of momentum, heat, and mass transfer*], John Wiley, New York, 4th ed. (2001).

[172] Haghgooie, R., *Structure and dynamics of mangetorheological fluids confined in microfluidic devices*, Ph.D. Thesis – Massachusetts Institute of Technology, Dept. of Chemical Engineering (2006).